MECHANISMS OF ACTION AND INHIBITION
OF [4FE-4S] PROTEINS ISPG AND ISPH IN ISOPRENOID BIOSYNTHESIS

BY

WEIXUE WANG

DISSERTATION

Submitted in partial fulfillment of the requirements
for the degree of Doctor of Philosophy in Biophysics & Computational Biology
in the Graduate College of the
University of Illinois at Urbana-Champaign, 2012

Urbana, Illinois

Doctoral Committee:

Professor Eric Oldfield, Chair
Professor Thomas B. Rauchfuss
Associate Professor Chad Rienstra
Professor Martin Gruebele

Abstract

The methylerythritol phosphate pathway (also known as the non-mevalonate pathway) of isoprenoid biosynthesis is potentially an important anti-bacterial and anti-malarial drug target. However, the catalytic mechanisms of the last two enzymes in this pathway, IspG (also known as GcpE) and IspH (also known as LytB) were largely unknown, and there were no inhibitors targeting these two enzymes. These two enzymes both are [4Fe-4S] proteins with one unique iron not bonded to any cysteine residue, and catalyze $2e^-/2H^+$ reductions.

In this study, bioorganometallic mechanisms are proposed for IspG and IspH catalyses, where direct iron-carbon interactions play important roles. This is a new type of catalytic mechanism of iron-sulfur enzymes, and is supported by extensive characterizations of trapped reaction intermediates: in IspG catalysis, a reaction intermediate with Fe-C and Fe-O bonding has been identified; whereas in IspH catalysis, an alkoxide complex, a weak π-complex, and an η3-allyl complex has been discovered along the reaction pathway. No free radical intermediates were observed. In addition, the first potent inhibitors against IspG and IspH have been discovered. Based on the catalytic mechanism of IspH enzyme, alkyne diphosphate inhibitors against both enzymes were rationally designed; pyridine diphosphate inhibitors against *Aquifex aeolicus* IspH were discovered by compound library screening. The binding modes of both types of inhibitors have also been determined.

The work reported here is of broad general interest, since it clarifies the nature of the reaction mechanisms of IspG and IspH catalyses, and opens up new routes to inhibitor design, of interest in the context of both anti-bacterial as well as anti-malarial drugs.

Acknowledgement

This work would not have been done without the great support and sharp guidance from my advisor, Professor Eric Oldfield. I won't forget those hours spent with Dr. Oldfield discussing all kinds of possible reaction mechanisms drawn on piles of yellow scratch papers. Those moments when we were discussing hot data and inspired with sparkling new ideas were some of my best memories in my graduate research life.

This work would not have been possible either without Dr. Ke Wang's effort: the large numbers of compounds he synthesized have been crucial for the entire project. I was very impressed by his hard-working as well as his ability of making all kinds molecules, especially those specifically isotopically labeled ones. I also owe the success of this work to Jikun Li, for those labeled and unlabeled IspG substrates he prepared.

Many other Oldfield group members have contributed to this project as well: I thank Dr. Joo-Hwan No for performing computational docking; Yi-Liang Liu for his effort and help on site-directed mutagenesis; Dr. Yonghui Zhang and Dr. Kai Li for synthesizing several inhibitors; and Francisco Guerra for help on computer-related problems, as well as for being a warm-hearted office mate for four years. I want to thank all other Oldfield group members as well, for their general help and friendship.

For making my electron paramagnetic resonance study possible, I would like to thank Professor Mark J. Nilges of the Illinois EPR Research Center. He nicely trained me using both continuous-wave and pulsed EPR spectrometers, and instructed me how to set up various pulsed

Table of Contents

Chapter 1

Introduction

1.1 Methylerythritol Phosphate Pathway as an Anti-bacterial and Anti-malarial Drug Target

There is an urgent need for new anti-infective drugs. The total number of antibiotics introduced has been rapidly decreasing, plus resistance to all antibiotics is becoming a major problem.[1] For example, the occurrence of not only drug resistant, multi-drug resistant and now of extensively drug resistant strains of *M. tuberculosis*[2] are enormous threats, as is the morbidity and mortality burden of malaria, Chagas disease and the leishmaniases, in less developed nations.[3] So new targets, as well as new concepts are of interest.

Enzymes in the methylerythritol phosphate pathway (MEP pathway, also known as non-mevalonate pathway, scheme 1.1) are emerging anti-bacterial and anti-malarial drug targets.[4] This pathway makes the five-carbon fundamental building blocks of isoprenoids, isoprenoids isopentenyl diphosphate (IPP, **1**) and dimethylallyl diphosphate (DMAPP, **2**),[5,6] shown in Scheme 1.1, to produce C_{10}, C_{15}, C_{20} etc. species.[7] This pathway is essential in plants, most bacteria, and in some protozoan parasites of the phylum *Apicomplexa*, but in humans, **2** and **3** are formed exclusively from a totally different pathway, the mevalonate pathway. Therefore, the MEP pathway has great possibilities for the development of novel anti-infective drugs,[4] and indeed, inhibition of the second enzyme of this pathway (1-deoxyxylulose-5-phosphate reductoisomerase,

DXR) by the phosphonate inhibitor fosmidomycin, has been shown to be quite effective against

malaria parasite infections in a clinical trial.[8]
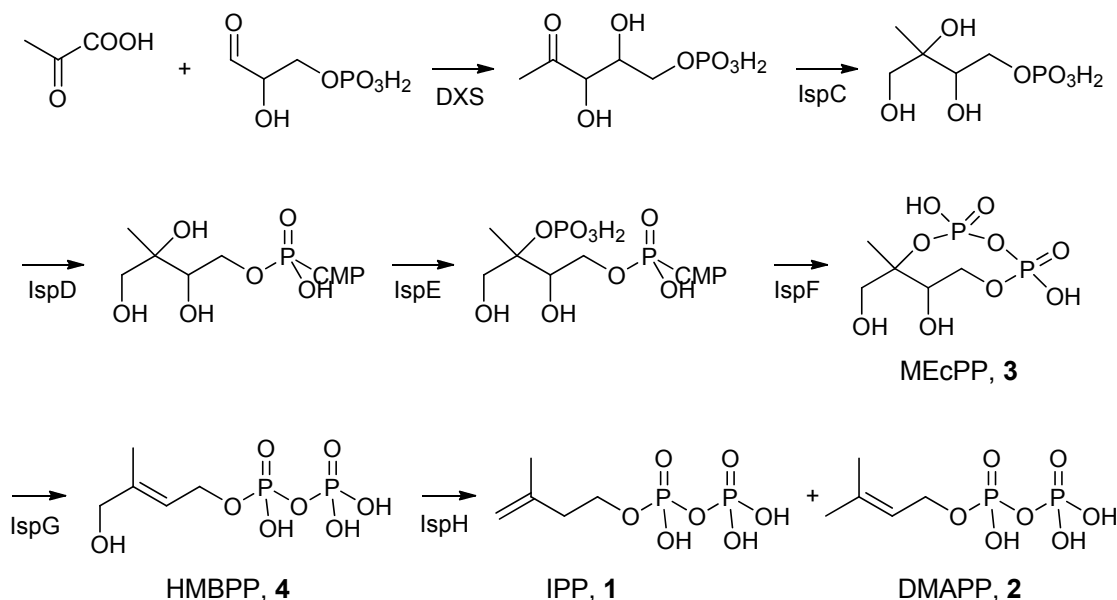
Scheme 1.1. Tthe methylerythritol phosphate pathway.

1.2 The Last Two Enzymes in MEP Pathway, IspG and IspH

IspG and IspH (also known as GcpE and LytB, respectively) are the last two enzymes in this

pathway. IspG converts 2-C-methylerythritol-cyclo-2,4-diphosphate (MEcPP, **3**) to

(*E*)-4-hydroxy-3-methyl-but-2-enyl- 1-diphosphate (HMBPP, **4**), which is further converted to **1**

and **2** by IspH. These two enzymes are essential for pathogen survival and, as such, are validated

drug targets. Moreover, inhibiting IspH is expected to raise the level of **4** (as it does in a IspH

knockout[9]), which is a very potent phosphoantigen that activate human $\gamma\delta$ T cells,[10] leading

potentially to even more effective pathogen killing. This is an entirely new approach to

chemo-immunotherapy in the anti-infective area, in which pathogens are either killed by having isoprenoid biosynthesis shut down, or they are "highlighted" for prompt immune system killing, by $\gamma\delta$ T cells.
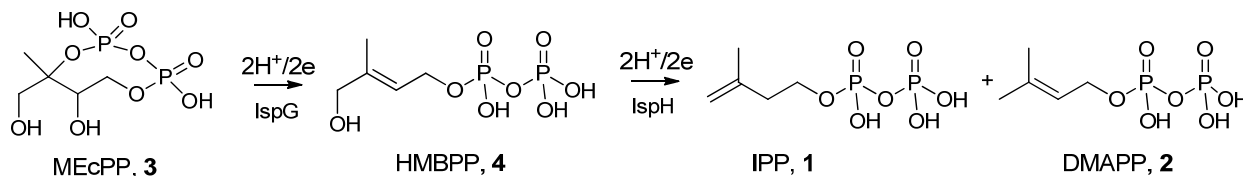
Scheme 1.2. Reactions catalyzed by IspG and IspH.

These two enzymes are also fascinating from a structure/function perspective, since they contain unusual [4Fe-4S] clusters coordinated to only three cysteine residues, with a unique 4th iron not bonded to a cysteine thiol group. This is somewhat analogous to *Pyrococcus furiosus* ferredoxin,[11] aconitase[12] and the radical-SAM family enzymes[13-15], but here, IspG and IspH carry out $2H^+/2e$ deoxygenation reactions (Scheme 1.2). Over the years, up until early 2010, approximately six mechanisms have been proposed for IspH enzyme,[5,6,16-19] and four for IspG enzyme.[6,20-22] Most of these proposals contained a series of carbon cation, carbon anion, and carbon radical reaction intermediates; however, there has been no direct evidence support the involvement of radical species. How do IspG and IspH actually catalyze these reactions? Can we trap any of these proposed reaction intermediates? As I will show later, mechanistic study on the two enzymes reported in this work has revealed a novel type of catalytic mechanisms involving bioorganometallic species,[23-25] and has led to the discovery of the first potent IspH and IspG inhibitors.[23,24,26,27]

1.3 Research Strategies

The ultimate aim of this research is to design inhibitors/drug leads targeting IspH and IspG. But how to proceed, when neither the structures nor the catalytic mechanisms were known? One possible approach is to make substrate analogs which bind to target enzymes but cannot turnover. The first attempt using this approach reported a series of IspH substrate analogs but all had very weak inhibitory effects;[28] a more recent report showed that the thio-analog (**5**) and amino-analog (**6**) of the natural substrate **4** (Scheme 1.3) are potent IspH inhibitors, with sub-μM IC_{50} values.[29] However, this strategy limits the diversity of inhibitor structures. Are there other ways to design inhibitors? Two alternative strategies have been used in this study, and each has led to a different type of inhibitors.
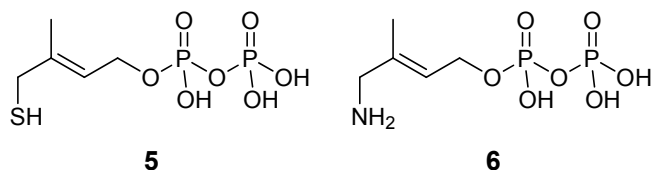
Scheme 1.3. Two potent IspH inhibitors designed based on the structure of IspH substrate **4**.

The first strategy in my research was rational inhibitor design, which requires knowledge on either the target structure, or the target enzyme catalytic mechanism, or both. I focused my study on elucidating the catalytic mechanisms of these two enzymes (Chapter 2 and 3). Because in the turnover state, the [4Fe-4S] clusters of both enzymes are in the paramagnetic, reduced state ([4Fe-4S]$^+$), this paramagnetism adds a invaluable dimension to the study of reaction mechanisms - the application of electron paramagnetic resonance (EPR) spectroscopy is thus

possible. As a result, EPR spectroscopy has been extensively used for characterizing various trapped paramagnetic reaction intermediates. Based on the *g* tensors obtained from continuous-wave EPR spectroscopy, different intermediates could be identified; more detailed structural information was obtained from pulsed EPR experiments,[30] often in combination with isotopic labeling. Pulsed EPR spectroscopy (e.g. electron nuclear double resonance, or ENDOR, and hyperfine sublevel correlation, or HYSCORE) has much higher resolution than continuous-wave EPR, therefore small hyperfine features can be resolved. By spectral simulation,[31-33] hyperfine coupling tensors of nuclei with non-zero nuclear spin interacting with the electron spin can be obtained; for nuclei with greater than 1/2 nuclear spin, nuclear quadrupole coupling tensors can also be obtained. By comparing these spectroscopic data with those of well-studied systems, we have gained valuable insights on the nature of reaction intermediates; quantum chemical calculations on model systems have also helped the understanding of the structures of reaction intermediates. This mechanistic study turned out to be very rewarding, as it has led not only to a novel type of catalytic mechanisms of iron-sulfur enzymes involving direct iron-carbon interactions, but also to the discovery of the first potent IspH and IspG inhibitors. Based on the proposed structure of an IspH reaction intermediate (a π-complex **7**, shown in Scheme 1.4), alkyne diphosphates (**8-10**, Scheme 1.4) with μM or even sub-μM IC_{50} values against both enzymes were designed (Chapter 4). Remarkably, these inhibitors are also the most potent inhibitors against IspG. With either enzyme, we believe those alkyne inhibitors form π-complexes with the unique iron of the [4Fe-4S] cluster, just in a similar way as the alkene substrate **4** binding to IspH.
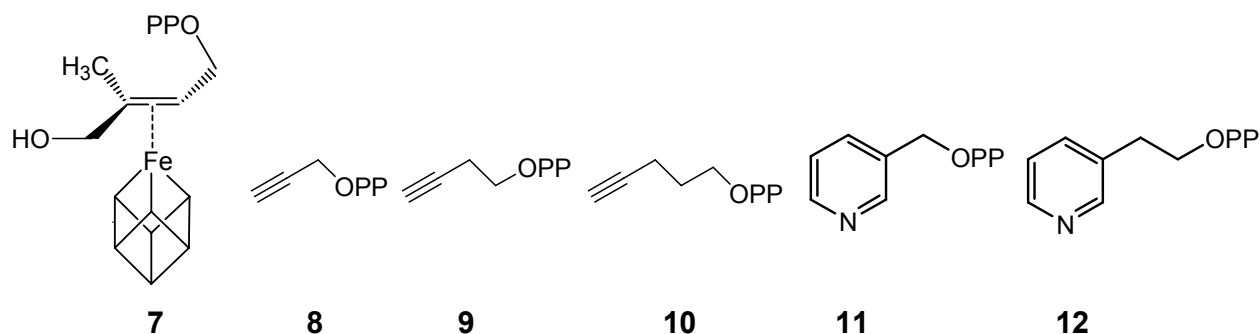
Scheme 1.4. The proposed structure of one of IspH reaction intermediates (**7**), and designed inhibitors inspired by this intermediate (**8-10**). Inhibitor **11** and **12** were discovered in compound library screening. OPP represents the diphosphate group.

The second strategy to discover inhibitors was compound library screening. In our laboratory there is a compound library containing more than a thousand compounds, mostly bisphosphonates and diphosphates. By screening using enzyme kinetic assays I discovered another type of inhibitors against *Aquifex aeolicus* IspH, pyridine diphosphates. After structural optimizations based on the original discovered pyridine diphosphate (**11**), the best compound (**12**) has an IC50 of ~ 9 μM (Chapter 5).

To find out how these inhibitors bind to their target, I again took advantage of the paramagnetism of the reduced IspH/IspG enzymes. EPR spectroscopy has been used to characterize the binding modes of inhibitors to the reduced enzymes with [4Fe-4S]$^+$ clusters, by measuring hyperfine coupling/nuclear quadrupole coupling tensors, similar to that used in studies on reaction intermediates. But how do these inhibitors bind to the oxidized enzyme? In the oxidized state the [4Fe-4S]$^{2+}$ cluster is diamagnetic, therefore EPR-silent. We have to use alternative strategies - using Mössbauer spectroscopy and X-ray crystallography. The result of

this study was rather surprising - the reductase IspH has hydratase activity in its oxidized state, as it can convert certain alkyne diphosphates into the corresponding aldehyde and ketone (Chapter 6).

Overall, IspG and IspH are two fascinating proteins not only because of their importance as potentially anti-infective drug targets, but also because of their intriguing or even unexpected chemistries. I hope my work presented here will open up new routes to inhibitor design targeting the MEP isoprenoid biosynthesis pathway, and inspire future iron-sulfur chemistry research.

1.4 References

(1) Clatworthy, A. E.; Pierson, E.; Hung, D. T. *Nat Chem Biol* **2007**, *3*, 541.

(2) World Health Organization. *Anti-tuberculosis: Drug resistance in the world.*
     www.who.int/tb/publications/2008/drs_report4_26feb08.pdf.

(3) World Health Organization. www.who.int/mediacentre/factsheets/fs094/en.

(4) Rohmer, M.; Grosdemange-Billiard, C.; Seemann, M.; Tritsch, D. *Curr Opin Investig Drugs*
     2004, *5*, 154.

(5) Altincicek, B.; Duin, E. C.; Reichenberg, A.; Hedderich, R.; Kollas, A. K.; Hintz, M.; Wagner,
     S.; Wiesner, J.; Beck, E.; Jomaa, H. *FEBS Lett* **2002**, *532*, 437.

(6) Rohdich, F.; Zepeck, F.; Adam, P.; Hecht, S.; Kaiser, J.; Laupitz, R.; Grawert, T.; Amslinger,
     S.; Eisenreich, W.; Bacher, A.; Arigoni, D. *Proc Natl Acad Sci U S A* **2003**, *100*, 1586.

(7) Rohmer, M. *Nat Prod Rep* **1999**, *16*, 565.

(8) Missinou, M. A.; Borrmann, S.; Schindler, A.; Issifou, S.; Adegnika, A. A.; Matsiegui, P. B.; Binder, R.; Lell, B.; Wiesner, J.; Baranek, T.; Jomaa, H.; Kremsner, P. G. *Lancet* **2002**, *360*, 1941.

(9) Eberl, M.; Altincicek, B.; Kollas, A. K.; Sanderbrand, S.; Bahr, U.; Reichenberg, A.; Beck, E.; Foster, D.; Wiesner, J.; Hintz, M.; Jomaa, H. *Immunology* **2002**, *106*, 200.

(10) Reichenberg, A.; Hintz, M.; Kletschek, Y.; Kuhl, T.; Haug, C.; Engel, R.; Moll, J.; Ostrovsky, D. N.; Jomaa, H.; Eberl, M. *Bioorg Med Chem Lett* **2003**, *13*, 1257.

(11) Conover, R. C.; Kowal, A. T.; Fu, W. G.; Park, J. B.; Aono, S.; Adams, M. W.; Johnson, M. K. *J Biol Chem* **1990**, *265*, 8533.

(12) Lauble, H.; Kennedy, M. C.; Beinert, H.; Stout, C. D. *Biochemistry* **1992**, *31*, 2735.

(13) Berkovitch, F.; Nicolet, Y.; Wan, J. T.; Jarrett, J. T.; Drennan, C. L. *Science* **2004**, *303*, 76.

(14) Seemann, M.; Wegner, P.; Schunemann, V.; Bui, B. T.; Wolff, M.; Marquet, A.; Trautwein, A. X.; Rohmer, M. *J Biol Inorg Chem* **2005**, *10*, 131.

(15) Adedeji, D.; Hernandez, H.; Wiesner, J.; Kohler, U.; Jomaa, H.; Duin, E. C. *FEBS Lett* **2007**, *581*, 279.

(16) Wolff, M.; Seemann, M.; Tse Sum Bui, B.; Frapart, Y.; Tritsch, D.; Garcia Estrabot, A.; Rodriguez-Concepcion, M.; Boronat, A.; Marquet, A.; Rohmer, M. *FEBS Lett* **2003**, *541*, 115.

(17) Xiao, Y.; Zhao, Z. K.; Liu, P. *J Am Chem Soc* **2008**, *130*, 2164.

(18) Grawert, T.; Rohdich, F.; Span, I.; Bacher, A.; Eisenreich, W.; Eppinger, J.; Groll, M. *Angew Chem Int ed* **2009**, *48*, 5756.

(19) Grawert, T.; Span, I.; Bacher, A.; Groll, M. *Angew Chem Int ed* **2010**, *49*, 8802.

(20) Kollas, A. K.; Duin, E. C.; Eberl, M.; Altincicek, B.; Hintz, M.; Reichenberg, A.; Henschker, D.; Henne, A.; Steinbrecher, I.; Ostrovsky, D. N.; Hedderich, R.; Beck, E.; Jomaa, H.; Wiesner, J. *FEBS Lett* **2002**, *532*, 432.

(21) Seemann, M.; Bui, B. T.; Wolff, M.; Tritsch, D.; Campos, N.; Boronat, A.; Marquet, A.; Rohmer, M. *Angew Chem Int ed* **2002**, *41*, 4337.

(22) Brandt, W.; Dessoy, M. A.; Fulhorst, M.; Gao, W.; Zenk, M. H.; Wessjohann, L. A. *Chembiochem* **2004**, *5*, 311.

(23) Wang, W.; Wang, K.; Liu, Y.-L.; No, J. H.; Nilges, M. J.; Oldfield, E. *Proc Natl Acad Sci USA* **2010**, *107*, 4522.

(24) Wang, W.; Li, J.; Wang, K.; Huang, C.; Zhang, Y.; Oldfield, E. *Proc Natl Acad Sci USA* **2010**, *107*, 11189.

(25) Wang, W.; Wang, K.; Li, J.; Nellutla, S.; Smirnova, T. I.; Oldfield, E. *J Am Chem Soc* **2011**, *133*, 8400.

(26) Wang, K.; Wang, W.; No, J. H.; Zhang, Y.; Zhang, Y.; Oldfield, E. *J Am Chem Soc* **2010**, *132*, 6719.

(27) Wang, W.; Li, J.; Wang, K.; Smirnova, T. I.; Oldfield, E. *J Am Chem Soc* **2011**, *133*, 6525.

(28) Van Hoof, S.; Lacey, C. J.; Rohrich, R. C.; Wiesner, J.; Jomaa, H.; Van Calenbergh, S. *J Org Chem* **2008**, *73*, 1365.

(29) Ahrens-Botzong, A.; Janthawornpong, K.; Wolny, J. A.; Tambou, E. N.; Rohmer, M.; Krasutsky, S.; Poulter, C. D.; Schunemann, V.; Seemann, M. *Angew Chem Int ed* **2011**, *50*,

11976.

(30) Schweiger, A.; Jeschke, G. *Principles of Pulse Electron Paramagnetic Resonance*; Oxford

Univ Press: Oxford, 2001.

(31) Hoffman, B. M.; Martinsen, J.; Venters, R. A. *Journal of Magnetic Resonance* **1984**, *59*,

110.

(32) Hoffman, B. M.; Venters, R. A.; Martinsen, J. *Journal of Magnetic Resonance* **1985**, *62*,

537.

(33) Stoll, S.; Schweiger, A. *J Magn Reson* **2006**, *178*, 42.

Chapter 2

Bioorganometallic Mechanism of Action

of the [4Fe-4S] Protein IspG

2.1 Notes and Acknowledgement

I would like to sincerely thank Ke Wang for synthesizing compounds **3** and **7-12**, and Jikun Li for preparing compounds **2**, [*U*-^{2}H]-**2**, **4** and **6**. Without these compounds, this work is hardly possible. I would also like to thank Yong Zhang for a long-term collaboration on this project, for which he performed a large amount of quantum chemical calculations to help us understand the nature of the reaction intermediate. I also thank Mark J. Nilges for helpful discussions and assistance with ENDOR and pulsed EPR experiments, and Thomas B. Rauchfuss and Sergei Dikanov, for their helpful suggestions. Finally, I thank Pinghua Liu for providing the *E. coli* IspG expression system, Hassan Jomaa and Jochen Wiesner for providing the *T. thermophilus* IspG expression system, Dennis Dean for providing the *isc* proteins expression system, and Wolfgang Eisenreich and Victoria Illarionova for providing compound **5**. This work was supported by the United States Public Health Service (NIH grants GM65307 and GM073216) for Eric Oldfield and American Heart Association Midwest Affiliate Predoctoral Fellowship (Award 10PRE4430022) for Weixue Wang.

This chapter was reproduced in part with permission from Wang W, Li J, Wang K, Huang C,

Zhang Y, Oldfield E (2010) Organometallic mechanism of action and inhibition of the 4Fe-4S isoprenoid biosynthesis protein GcpE (IspG), *Proc Natl Acad Sci USA* 107: 11189-11193, Copyright (2010) National Academy of Sciences, U.S.A.; and from Wang W, Wang K, Li J, Nellutla S, Smirnova TI, Oldfield E (2011) An ENDOR and HYSCORE investigation of a reaction intermediate in IspG (GcpE) catalysis, *J Am Chem Soc* 133: 8400-8403, Copyright (2011) American Chemical Society.

2.2 Introduction

IspG ((*E*)-4-hydroxy-3-methyl-but-2-enyl-1-diphosphate (**1**) synthase, EC 1.17.7.1, also known as GcpE) is the penultimate enzyme in the non-mevalonate isoprenoid biosynthesis pathway. IspG enzymes catalyze the $2H^+/2e^-$ reduction of 2-*C*-methyl-D-erythritol-2,4-*cyclo*-diphosphate (**2**, MEcPP) to HMBPP **1**,[1] shown in Scheme 2.1.
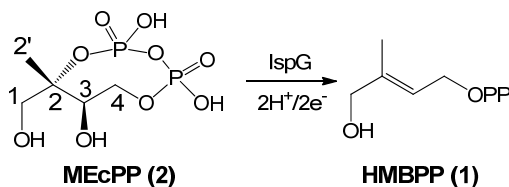

Scheme 2.1. Reaction catalyzed by IspG.

All IspGs contain three highly conserved cysteine residues that are essential for catalysis, and are thought to bind to an iron-sulfur cluster.[2,3] This cluster is, based on the results of Mössbauer[2] and EPR[3] spectroscopy, thought to have a [4Fe-4S] composition. Its mechanism of

action was not well understood, and there were no potent inhibitors reported at the time I started this project (year 2009). There have been several catalytic mechanisms proposed for IspG shown in Figure 2.1. In one, Kollas et al.[4] proposed ring-opening of the *cyclo*-diphosphate to form a carbocation, followed by reduction to a radical, which then underwent reduction and dehydration to form the product, HMBPP **1** (Figure 2.1A). In a second mechanism, Seemann et al.[5] proposed a similar route, but with subsequent formation of a cationic carbon radical (Figure 2.1B). In a third mechanism, Brandt et al.[6] proposed a carbon cation → radical → anion mechanism (Figure 2.1C). And in a fourth mechanism, Rohdich et al.[7] proposed that **2** underwent an OH⁻-assisted ring opening/ring closing to produce an epoxide, which was then reduced to the alkene, **1**, via radical intermediates (Figure 2.1D). Therefore, there are numerous mechanistic possibilities that have been proposed, however, none of these radical / cation / anion intermediates were observed in experiments.

In 2007, Adedeji et al.[3] reported that a paramagnetic intermediate was involved in IspG catalysis. Later, Nyland et al. found that the epoxide **3** is a substrate of IspG,[8] and we showed that **3** can form the same reaction intermediate as obtained with its natural substrate **2**.[9] But, the nature of this reaction intermediate was unknown. A key to understand IspG catalytic mechanism is to find out the structure of this reaction intermediate, which we call it "X. Therefore, I carried out extensive EPR spectroscopic characterizations of this intermediate, measuring the hyperfine coupling constants/tensors of most of the atoms of "X" prepared from a series of isotopically labeled substrates (Scheme 2.2, **4-12**). Base on these spectroscopic data, we proposed that "X" is most likely to be a ferraoxetane.
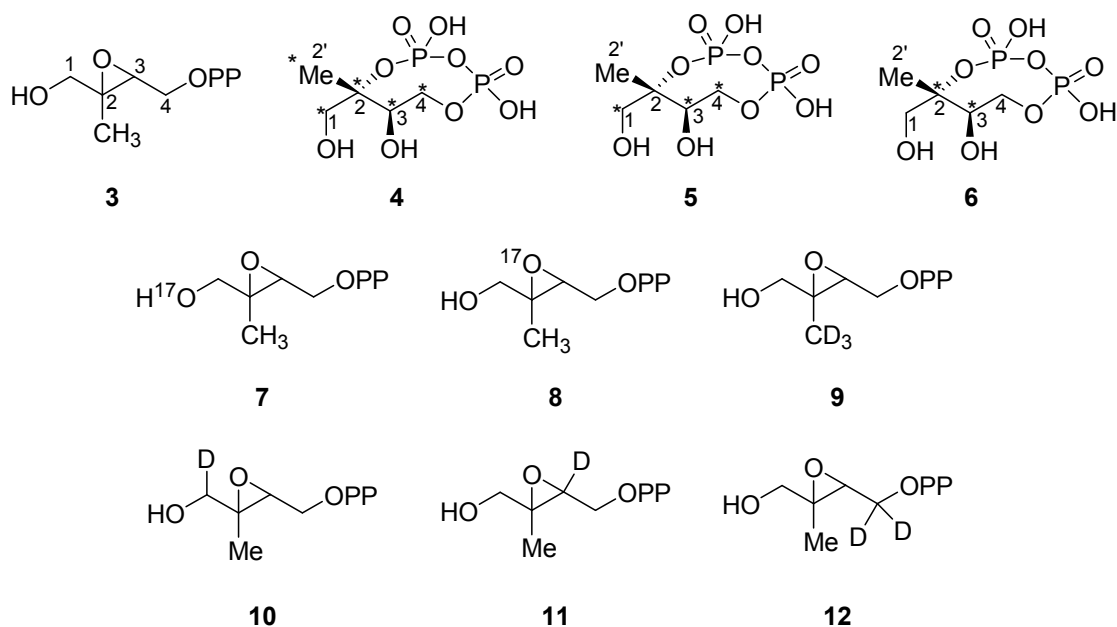
Scheme 2.2. Compounds used in this study. * marks ^{13}C label positions.

2.3 Results and Discussion

2.3.1 Continuous-wave EPR investigation on IspG catalysis

In a continuous-wave EPR study on IspG catalysis, the reaction intermediate "X" was clearly identified (Figure 2.2). The X-band EPR spectrum of reduced IspG in the absence of any exogenous ligands is typical for a $[Fe_4S_4]^+$ cluster, characterized by $g_{//} = 2.04$, $g_{\perp} = 1.90$ and g_{iso} = 1.95 (Figure 2.2A). However, if the substrate **2** was added and the reaction was frozen within 30 seconds, a different EPR spectrum was obtained, characterized by g = [2.092, 2.018, 1.999] and g_{iso} = 2.035 (Figure 2.2B). The same species can be trapped by using the epoxide **3** (Figure 2.2C). If the reaction was incubated for a longer time (45 minutes), the spectrum further changes (Figure 2.2D), which is essentially identical to that of the product **1** binding to IspG,

characterized by g = [2.092, 2.010, 1.976] and g_{iso} = 2.026 (Figure 2.2E). Based on these continuous-wave EPR data, it is clear that a paramagnetic transient species "X" formed during the catalysis, before the formation of the final product **1**.

What is the nature of this paramagnetic reaction intermediate "X"? Is it a carbon radical, as proposed in previous mechanisms (Figure 2.1)? To address this question, I prepared [57]Fe-enriched IspG and trapped this reaction intermediate. As shown in Figure 2.2B as red dashed line, the EPR linewidth significantly broadened due to unresolved [57]Fe hyperfine interactions. This indicates that most of the spin density is on the [4Fe-4S] cluster; therefore it is unlikely to be a carbon-based free radical. To obtain more detailed structural information, I measured hyperfine coupling constants of most of the atom in "X" derived from the substrates **2** or **3**.

2.3.2 ^{13}C hyperfine coupling measurement of the intermediate "X"

I first considered the ^{13}C hyperfine coupling tensors/constants measurement and assignment. The hyperfine sublevel correlation (HYSCORE) spectrum of "X" prepared by using *E. coli* IspG and [U-^{13}C] MEcPP (**4**) exhibits three sets of ^{13}C signals (Figure 2.3A): one has a relatively large (~17 MHz) hyperfine coupling, the second a small (~3 MHz) coupling, the third a very small ($\leq$ 1 MHz) coupling, consistent with results obtained using *T. thermophilus* IspG (Figure 2.3B).[9] To begin to specifically assign these signals, we obtained HYSCORE spectra using [1,3,4-^{13}C$_3$]-labeled MEcPP (**5**) and [2,3-^{13}C]-labeled MEcPP (**6**). The ~17 MHz hyperfine coupling is absent in the [1,3,4-^{13}C$_3$]-labeled sample (Figure 2.3C), but is present in the [2,3-^{13}C$_2$]-labeled sample (Figure 2.3D), indicating that this strongly coupled ^{13}C signal arises

15

from the quaternary carbon, C2. The results of simulations of HYSCORE spectra taken at different magnetic field strengths (Figure 2.4) and different τ-values (Figure 2.5) indicate that the hyperfine tensor (*A*) of C2 is [14.5, 12.0, 26.5] MHz, with an isotropic hyperfine coupling constant a_{iso} (^{13}C2) of 17.7 MHz.

The hyperfine coupling tensor of C2 indicates direct bonding interaction between the unique 4th iron and this carbon, for several reasons. First of all, the C2 hyperfine coupling tensor is highly anisotropic which possibly arises from the strong dipole-dipole interaction of C2 with the paramagnetic center; therefore it should be very close to the iron-sulfur cluster. Second, the observed ^{13}C2 isotropic hyperfine coupling constants (a_{iso} (^{13}C2) = 17.7 MHz) in "X" is close to that seen for ^{13}CO directly bonded to one of the irons in the H-cluster in the H_{ox}-CO state of a [FeFe] hydrogenase, where a_{iso}(^{13}CO) = 17.1 MHz.[10] In addition, the 17.7 MHz a_{iso} (^{13}C2) in "X" is much smaller than the 43.8 MHz a_{iso}(^{13}C) found in a formaldehyde-inhibited xanthine oxidase, in which the formaldehyde carbon is two bonds away from the Mo center.[11] This 43.8 MHz hyperfine coupling arises from a "trans-annular hyperfine interaction", and is in good accord with the results of DFT calculations (a_{iso}(^{13}C) $\approx$ 47.9 MHz).[11] However, in a structure containing a single Mo-C bond, the same DFT methods yielded an *A* (^{13}C) = [23.2, 13.4, 11.7] MHz, a_{iso} (^{13}C) = 16.1 MHz, very close to the ^{13}C2 hyperfine coupling results found with the reaction intermediate "X" in IspG. These comparisons suggest a direct interaction of iron with C2 in "X", rather than the large trans-annular hyperfine interaction seen in the Mo-containing system, whose square-pyramidal geometry enables a large metal-carbon orbital overlap.

The ~3 MHz ^{13}C signal arises from C3, since it is present in the [2,3-$^{13}C_2$]-MEcPP (**6**)

sample (Figure 2.3D). We also conclude that C3 is the only carbon that contributes to this 3 MHz ^{13}C signal, based on the following: First, **4**, **5** and **6** all give the same line-shapes and peak positions in their ^{13}C HYSCORE spectra for the ~3 MHz signals (Figures 2.3). Second, the ~3 MHz ^{13}C HYSCORE signal from samples prepared using **4** and **5** taken at different magnetic field strengths can be well simulated using just a single carbon, having A ([13]C3) = [1.8, 2.0, 5.1] MHz, a_{iso} ([13]C3) = 3.0 MHz (Figures 2.4, 2.6). Third, the ~3 MHz ^{13}C HYSCORE signals of samples prepared using **4** and **5** vary in the same manner with changes in τ-values (Figure 2.7), and can be well simulated using a single carbon with the hyperfine values given above (Figure 2.5).

2.3.3 [17]O hyperfine coupling measurement of the intermediate "X"

We then investigated the [17]O hyperfine coupling constants in the reaction intermediate "X", to probe possible Fe-O bonding. Because it is much easier to synthesize [17]O-labeled epoxides than to synthesize [17]O-labeled MEcPP, and because epoxide **3** forms exactly the same intermediate "X" as the natural substrate **2**, we prepared [17]O-labeled epoxides **7** and **8**. These two compounds correspond to [1-[17]O]-**2** and [3-[17]O]-**2**, respectively (scheme 2.3).

The HYSCORE spectrum of "X" prepared from **7** showed very small [17]O hyperfine coupling (0.15 MHz by simulation, Figure 2.8A), while "X" prepared from **8** gave quite big [17]O hyperfine coupling (~8 MHz by simulation, Figure 2.8B). In a search of literature, I found that H_x[17]O binding to the unique iron of aconitase yielded 8 ~ 12 MHz [17]O hyperfine coupling constants,[12] while aconitase with [17]O-labeled substrates or analogues yielded 9 ~ 15 MHz [17]O hyperfine coupling constants when [17]O-labeled carboxyl group or hydroxyl group bind to the unique iron.[13]

Comparing with these literature results, our experiments clearly indicate that the unique 4th iron of the [4Fe-4S] cluster binds to the 3-OH group of **2** in "X", but not to the 1-OH group.
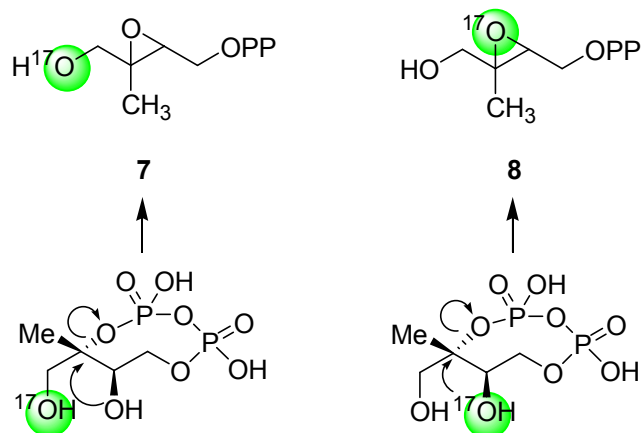
Scheme 2.3. ^{17}O-labeled epoxide **7** and **8** correspond to [1-^{17}O]-**2** and [3-^{17}O]-**2**, respectively.

2.3.4 ^{31}P hyperfine coupling measurement of the intermediate "X"

The diphosphate group of **2** is another a possible ligand to the unique 4th iron in the intermediate "X". To test this possibility, I have obtained ^{31}P Mims ENDOR spectrum of "X" (Figure 2.9). Only very small (0.08 MHz) ^{31}P hyperfine coupling constant was observed. Later, the full ^{31}P hyperfine coupling tensor was reported by Xu *et al.*,[14] where they found that the orientation-selective ^{31}P ENDOR data can be simulated by either an isotropic dominated tensor (A = [0.21, 0.09, 0.05] MHz) or a dipolar dominated tensor (A = [0.22, -0.11, -0.09] MHz). In either case, the small hyperfine coupling constant indicates that the diphosphate group does not bind to the iron-sulfur cluster. Using a point-dipole model, a minimum distance of 6.6 Å from the phosphorous nucleus to the unique 4th iron was estimated based on the dipolar-dominated

tensor.[14]

2.3.5 ^{1}H/^{2}H hyperfine coupling measurement of the intermediate "X"

^{1}H hyperfine coupling constants/tensors may also provide structural information of the intermediate "X". As shown in Figure 2.10A, a ^{1}H ENDOR signal with a large hyperfine coupling (A ~ 11.5 MHz) was observed with "X" prepared from unlabeled **2**. We also found that "X" prepared from unlabeled epoxide **3** shows almost identical ^{1}H ENDOR spectrum (Figure 2.10B). Later, Xu *et al*. performed orientation-selective ENDOR measurements followed by spectral simulation, and reported the hyperfine tensor for this proton being A (^{1}H) = [14,11,11] MHz, a_{iso} = 12 MHz.[14]

What is the origin of this a_{iso} = 12 MHz proton? This ^{1}H ENDOR signal does not decrease on ^{2}H$_2$O buffer exchange (Figure 2.10C) but is absent when [U-^{2}H]-**2** is used (Figure 2.10D), so it must originate from the ligand. In the sample prepared from [U-^{2}H]-**2**, we also find two sets of ^{2}H ENDOR signals (Figure 2.10E). The first has a large hyperfine coupling (A ~ 1.7 MHz) with a small quadrupole splitting and corresponds to the 11.5 MHz feature found in the ^{1}H ENDOR spectrum (Figure 2.10A). The second set has a smaller coupling (A ~ 0.5 MHz) and arises from a weaker or long-range interaction with other deuterons in the ligand.

To specifically assign the a_{iso} = 12 MHz proton in "X", we used four specifically-deuterated epoxides (**9-12**) which were easier to synthesize than their corresponding deuterated MEcPP **2** (Scheme 2.4). The reaction intermediate "X" prepared using **9** showed the 1.7 MHz ^{2}H resonance in its X-band Mims ENDOR spectrum (Figure 2.11A), consistent with the Davies ENDOR

spectra which showed the disappearance of the $A \sim 11.5$ MHz proton signal (Figures 2.10A, B).

Clearly then, the A ~ 11.5 MHz ^{1}H ENDOR signal arises from one or more protons in the C2′

methyl group. Interestingly, in addition to the 1.7 MHz ^{2}H resonance, an $A \sim 0.37$ MHz

resonance was also apparent in the Mims ENDOR spectrum (Figure 2.11A), suggesting

nonequivalence of the three methyl protons/deuterons. The three non-equivalent C2' methyl

deuteron signals of "X" prepared using **9** are better resolved in Q-band orientation-selective

ENDOR spectra (Figure 2.12), and these spectra can be well simulated with 3 sets of hyperfine

couplings in addition to a nuclear quadrupole coupling constant $(e^2qQ/h) \sim 165$ kHz. These

results indicate that the C2′ methyl group is essentially static at 20 K (and at 2 K^{14} since the line

shapes of the 12 MHz proton ENDOR signals are the same at these two temperatures).
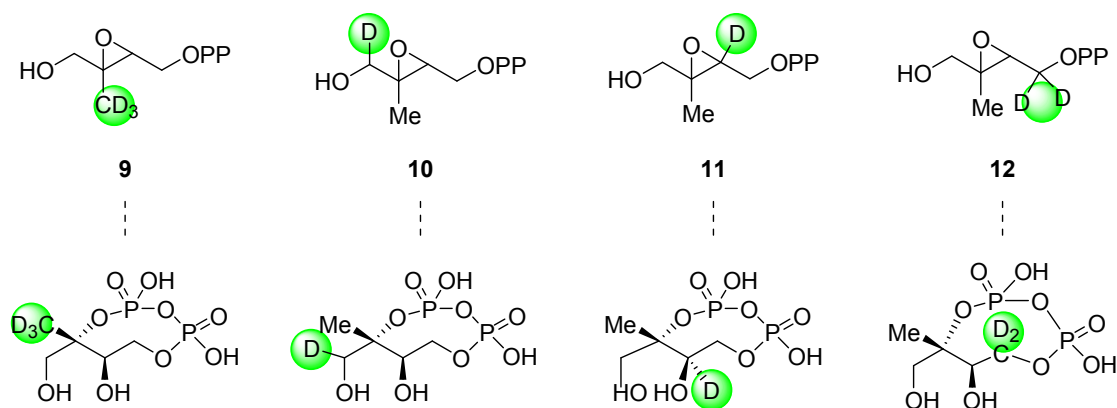

Scheme 2.4. Deuterated epoxides **9 - 12** and their corresponding deuterated MEcPP **2**.

The reaction intermediates "X" prepared using **10, 11**, and **12** showed ^{2}H resonances with

small hyperfine couplings (< 0.5 MHz) in their Mims ENDOR spectra (Figures 2.11B-D). These

signals, together with those from **9,** contributed to the broad, $A \sim 0.4$ MHz resonances seen with

[U-^{2}H]-**2** (Figure 2.11E, red dotted line), which can be well reproduced by adding the ^{2}H Mims

ENDOR spectra of "X" prepared using **9, 10**, **11**, and **12** (Figure 2.11E, black line).

2.3.6 Ferraoxetane as the reaction intermediate "X"

So far, I have measured the hyperfine coupling constants/tensors of most of the atoms of "X"

derived from the substrates **2** or **3**. Can we propose any structure for "X" based on these

spectroscopic data? As discussed previously, the ^{13}C and ^{17}O HYSCORE data has revealed direct

Fe-C2 bonding and Fe-O3 bonding. Therefore, a possible candidate for "X" is a ferraoxetane

(Scheme 2.5). This structure is not only consistent with ^{13}C and ^{17}O data, but also in good

agreement with ^{31}P and ^{1}H/^{2}H hyperfine coupling data. In this ferraoxetane structure, the

diphosphate group is away from the [4Fe-4S] cluster, consistent with very small ^{31}P hyperfine

coupling constant; protons on the C2' methyl group is also away from the [4Fe-4S] cluster,

therefore their hyperfine coupling tensors all have very small anisotropy due to weak

dipole-dipole interaction with the paramagnetic center.
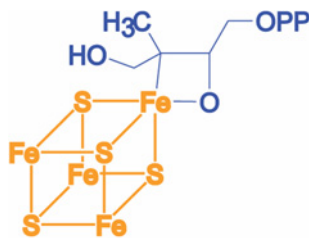
Scheme 2.5. Ferraoxetane as the reaction intermediate "X".

The possibility that the ferraoxetane is a reaction intermediate is intriguing, since many

metallaoxatanes are known as stable species,[15,16] and in the case of iron interacting with oxirane

itself, the 1,2-ferraoxetane has been observed using matrix isolation.[17] This species is more stable than is iron + oxirane,[18] and on warming, the ferraoxetane undergoes a [2+2] dissociation to ethylene and FeO.[17] The involvement of more complex metallaoxetanes in epoxide deoxygenation was proposed early on by Sharpless[19] (and would be essentially the opposite reaction to Sharpless epoxidation), and such species might be involved in oxirane deoxygenation, both by IspG, as well as by model [4Fe-4S] clusters.[20]

2.3.7 Validation by quantum chemical calculation

To see to what extent it might be possible to predict these spectroscopic observables, we used density functional theory (DFT). The structural model used was $[Fe_4S_4(SMe)_3(-C(CH_2OH)(CH_3)-CH(CH_2OH)-O-]^{2-}$ (Figure 2.13A inset) with S = 1/2. All calculations were performed with the Gaussian 09 program[21] using a Wachters' basis (62111111/3311111/3111) for Fe, 6-311G(d) for other heavy atoms, 6-31G(d) for hydrogens, and the BPW91 functional, as reported previously.[22]

We found good accord with experiment for C2′ methyl protons, with calculated a_{iso}s of 9.1, 2.0, and 1.1 MHz for the three non-equivalent protons. Interestingly, the a_{iso}s of these three protons are found to be dependent on the H-C-C-Fe dihedral angles. The large coupling is in good accord with experimental results ($A(^1H)$ ~12 MHz) and arises from the *trans* (Fe-C-C-H torsion angle = 172°) proton, while the gauche$^{\pm}$ protons with geometry optimized torsion angle of 52, -67° have much smaller couplings – similar to the observation of large ^3J *trans* scalar couplings in NMR spectroscopy. Overall, there is a good correlation between the computed hyperfine couplings determined with DFT and those determined experimentally, as shown in

Figure 2.12A and Table 2.1, although overall there is a systematic error in the slope, due most likely to basis/functional deficiencies. The correlation coefficient, R = 0.87 is, however, very good. The computed spin densities are shown graphically in Figure 2.12B and show that significant spin density is transmitted from the cluster to the H2′-*trans* proton (indicated with an arrow).

2.4 Conclusions

The results described above are of interest for several reasons. First, I found that MEcPP **2** and epoxide **3** form the same reaction intermediate "X". Second, based on ^{1}H/^{2}H, ^{13}C, ^{17}O and ^{31}P hyperfine coupling measurements and assignments, we proposed a tentative structure for this intermediate, most likely a ferraoxetane, which is consistent with all my spectroscopic data. Third, we are able to reproduce reasonably well the spectroscopic data by DFT calculation on a model ferraoxetane; in addition, we found that the isotropic hyperfine coupling constants of the three protons on C2' methyl group depend on H-C-C-Fe dihedral angle. These computational results support ferraoxetane as the reaction intermediate "X" in IspG catalysis.

2.5 Materials and Methods

2.5.1 Materials

All chemicals were purchased from Sigma-Aldrich (St. Louis, MO) and were used as provided. BL-21(DE3) competent cells were purchased from Stratagene (La Jolla, CA).

Syntheses of compounds **3-12** were performed by Ke Wang and Jikun Li, and were reported elsewhere.[9,23] Density functional calculations were performed by Yong Zhang and was reported elsewhere.[24]

2.5.2 *T. thermophilus* **IspG protein expression and purification**

TOP10F'(Invitrogen) cells harboring the *T. thermophilus* GcpE construct were grown in Luria-Bertani media containing 0.2 % glucose, 0.5 mM $CaCl_2$,1 mM $MgCl_2$ and 100 mg/L ampicillin at 37°C until the OD_{600} reached ~ 0.6-0.8. Induction was performed with 1mM IPTG, followed by incubation at 32°C, overnight. Cells were harvested by centrifugation at 9000 rpm for 8 mins, then stored at -80 °C. Cell pellets were resuspended and lysed in B-PER (Thermo Scientific, Rockford, IL) protein extraction reagent for about two hours at 4°C, then the lysate was centrifuged at 250,000 rpm, for 20 minutes. The supernatant was collected and loaded onto a Ni-NTA column equilibrated with 10 mM imidazole in pH 8.0 buffer containing 50 mM Tris·HCl and 150 mM NaCl. After washing with 40 mM imidazole, protein was eluted using an imidazole gradient (40-500 mM) in pH 8.0 buffer containing 50 mM Tris·HCl and 150 mM NaCl. Fractions were collected and dialyzed in pH 8.0 buffer containing 50 mM Tris·HCl, 150 mM NaCl, 5% glycerol, and 1mM DTT, three times. The purified protein was flash-frozen in liquid nitrogen, then stored at -80 °C until use.

2.5.3 *T. thermophilus* **IspG reconstitution**

T. thermophilus GcpE protein was transferred into a Coy Vinyl Anaerobic Chamber after being degassed on a Schlenk line. All the following steps were performed inside the anaerobic chamber with an oxygen level < 2 ppm. In a typical reconstitution experiment, 10 mM DTT and

~ 0.5 mg of elemental sulfur were added to 3 mL 0.6 mM protein solution in a pH 8.0 buffer containing 50 mM Tris·HCl, 150 mM NaCl and 5% glycerol. After stirring for 1.5 hours, $FeCl_3$ was then added from a 30 mM stock solution, slowly, to 6 equivalents. After 3 hours, an aliquot of the solution was centrifuged and a UV-VIS spectrum recorded. The A_{410}/A_{280} ratio was typically ~0.4. The protein was then desalted by passing through a PD10 column. The reconstituted protein was concentrated by ultrafiltration, and the protein concentration determined by using a Bio-Rad (Hercules, CA) Protein Assay kit.

2.5.4 *E. coli* IspG protein expression and anaerobic purification

BL-21(DE3) cells over-expressing *E. coli* IspG (encoded in plasmid pASK-IBA5$^+$) and *isc* proteins (encoded in plasmid pDB1282) were grown in LB media supplemented with 100 mg/L ampicillin and 50 mg/L kanamycin at 37 °C, until the OD_{600} reached 0.3. Cells were then induced with 0.5 g L-arabinose to initiate over-expression of the *isc* proteins. Cysteine (0.5 mM) and $FeCl_3$ (0.1 mM) were supplemented, and cells were grown until the OD_{600} reached 0.6. At this point, 400 μg/L anhydrotetracycline was added to induce overexpression of *E. coli* IspG. Cells were grown at 21 °C for 24 hours, then were harvested by centrifugation (9000 rpm, 8 min, 4 °C) and were kept at -80 °C until use.

All purification steps were carried out in a Coy Vinyl Anaerobic Chamber (Coy Laboratories, Grass Lake, MI) with an oxygen level < 2 ppm, and all buffers were degassed by using a Schlenk line. Cell pellets were resuspended in 100 mM Tris-HCl, 150 mM NaCl buffer (pH 8.0). Lysozyme, Benzonase nuclease (EMD Chemicals, San Diego, CA) and phenylmethanesulfonyl fluoride were added, and stirred for 1.5 hour at 10 °C followed by sonication (Fisher Scientific

Sonic Dismembrator, Model 500) with 4 pulses, each 7 sec duration at 35% power. The cell lysate was then centrifuged at 11,000 rpm at 10 °C for 30 min. The supernatant was purified by using Strep-tactin chromatography.[25] Fractions having a brown color were collected and desalted in pH 8.0 buffer containing 100 mM Tris-HCl and 150 mM NaCl.

2.5.5 EPR/ENDOR/HYSCORE sample preparation

All samples were prepared inside a Coy Vinyl Anaerobic Chamber with an oxygen level < 2 ppm. Samples were typically 1.0-2.0 mM in IspG for ENDOR/HYSCORE, and 0.3 mM for continuous-wave EPR. Glycerol was added as a glassing agent to 20% (v/v), and 40 equivalents of sodium dithionite were added as a reducing agent. Ligands (MEcPP or HMBPP-epoxide) were added to 20 equivalents. To trap the reaction intermediate "X", samples in EPR tubes (706-PQ-9.50, Wilmad Labglass, Vineland, NJ) were frozen in liquid nitrogen ~30 sec after substrate injection at room temperature.

2.5.6 EPR/ENDOR/HYSCORE spectroscopy

EPR spectra were collected at X-band using a Varian E-122 spectrometer together with an Air Products (Allentown, PA) helium cryostat. Data acquisition parameters were typically: field center = 3250 G; field sweep = 800 G; modulation = 100 kHz; modulation amplitude = 5 G; time constant = 32 ms; 60 s per scan; 8 s between each scan and temperature = 15K. Pulsed ENDOR/HYSCORE spectra were obtained on a Bruker ElexSys E-580-10 FT-EPR X-band EPR spectrometer equipped with an Oxford Instruments CF935 cryostat. A Bruker RF amplifier (150 watts, 100 kHz - 250 MHz) was used for ENDOR experiments. Mims ENDOR used a three-pulse sequence $\pi/2_{mw}$ - τ - $\pi/2_{mw}$ – T – $\pi/2_{mw}$ - τ - echo; $\pi/2_{mw}$ = 16 ns, with π_{RF} (20 μs, 3

dB attenuation) applied during T. The Mims ENDOR spectrum of "X" prepared using unlabeled HMBPP-epoxide was subtracted from that of "X" prepared using labelled HMBPP-epoxides. Davies ENDOR used a three-pulse sequence $\pi_{mw} - T - \pi/2_{mw} - \tau - \pi_{mw} - \tau -$ echo; $\pi/2_{mw} = 48$ ns, with π_{RF} (10 µs, 3 dB attenuation) applied during T. HYSCORE used a four-pulse sequence $\pi/2_{mw} - \tau - \pi/2_{mw} - t_1 - \pi_{mw} - t_2 - \pi/2_{mw} -$ echo; $\pi/2_{mw} = 16$ ns and $\pi_{mw} = 32$ ns, 256 points for both t_1 and t_2, each using 16 ns steps. Time-domain data were baseline corrected using a 3rd order polynomial, then Hamming windowed, followed by zero-filling and 2D-Fourier transformation. The HYSCORE spectrum was simulated using the EasySpin program package.[26]

Detailed operation steps of the pulsed EPR instrument and setting up a pulsed EPR experiment are described below. (1) Set up the cryostat with liquid helium as the cooling agent. (2) Turn on the cooling water for the magnet. Check if the water tank is full. (3) Turn on the magnet power. (4) Turn on the console. (5) Turn on the magnet. (6) Open Xepr on the computer, and connect to the spectrometer (select "connect to a spectrometer" under the Acquisition menu, and tyoe E580). (7) Set some spectrometer configurations. Open "spectrometer configuration" dialog box under acquisition menu. Select the desired band (X-band or Q-band); select the temperature controller; and select the correct probe and related calibration data. (8) Open the microwave bridge panel and find the resonance dip. (9) Insert the sample. Before inserting the sample, first turn off the pump on the liquid helium transfer line and wait until the pressure inside the cavity becomes positive. (10) Center the resonance dip. Adjust phase and iris. Bias bar should be at the center. (11) Take a continuous-wave EPR spectrum if necessary. (12) Over-couple the cavity. Re-center the now very broad resonance dip. (13) Turn on the TWT and

wait the green "standby" light is on. (14) Create a new experiment and select the desired experiment. (15) Open spec jet. Start pulsing (but with 60 dB TWT attenuation) and check if the defense pulse is present. (16) If the defense pulse is present, turn the TWT to the "operate" mode. (17) Adjust the microwave attenuation and timing of the pulses and gate and run the experiment.

2.6 Figures and Table
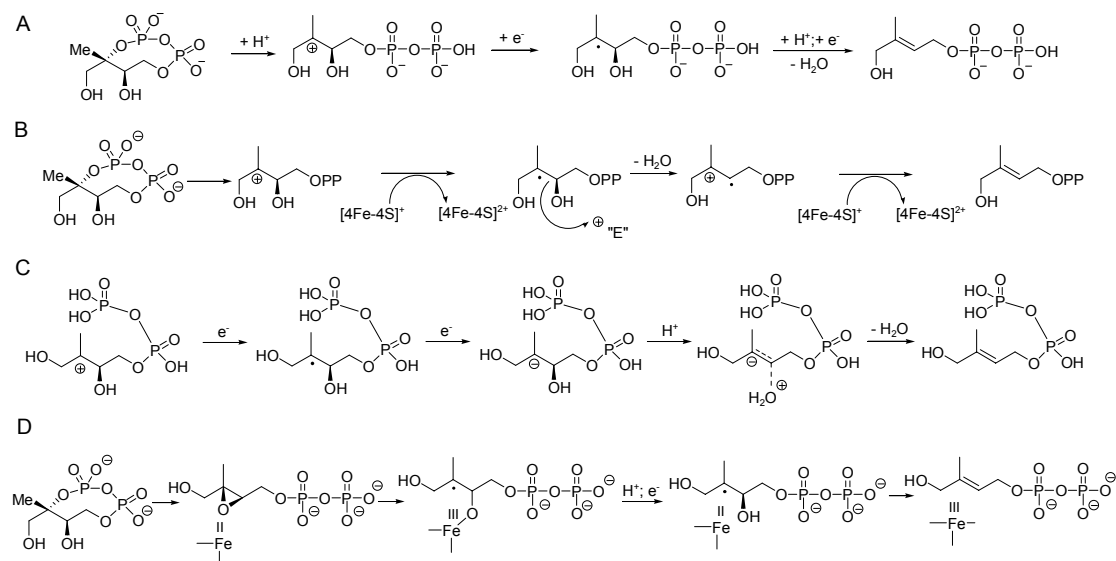

Figure 2.1. Previously proposed mechanisms of IspG catalysis. (A), cation → radical mechanism of Kollas *et al.*[4] (B), cation → radical → cation radical mechanism of Seemann *et al.*[5] (C), cation → radical → anion mechanism of Brandt *et al.*[6] (D), oxirane → radical mechanism of Rohdich *et al.*[7]
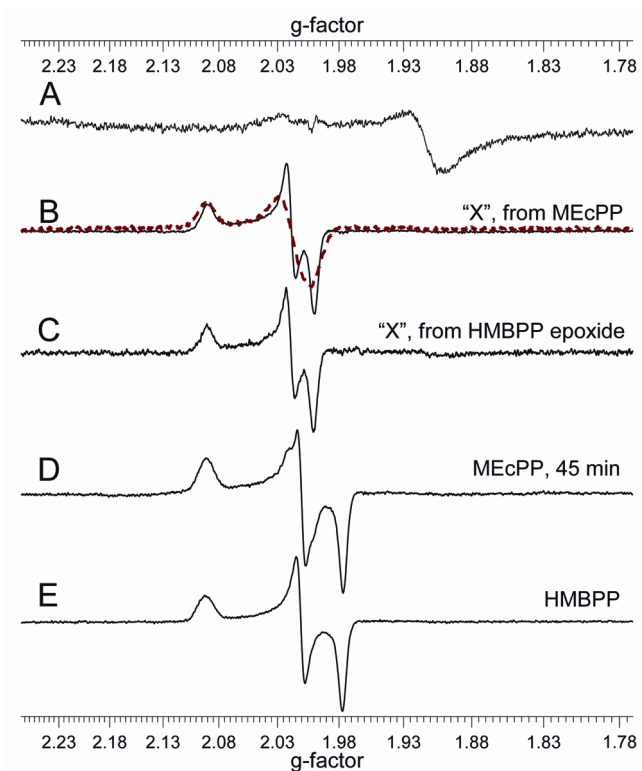
Figure 2.2. X-band EPR spectra of *E. coli* IspG ± reactants/products. (A), EPR spectrum of IspG reduced with 20 equivalents $Na_2S_2O_4$. (B), EPR spectrum of IspG + **2**, incubated for 1 minute. The red dashed line is the EPR spectrum of the same species but prepared with [57]Fe-enriched IspG. (C), EPR spectrum of IspG + **3**, incubated for 2 minutes. (D), EPR spectrum of IspG + **2**, incubated for 45 minutes. (E), EPR spectrum of IspG + **1**, incubated for 45 minutes. Microwave frequency = 9.05 GHz; microwave power = 1 mW for (A), 0.05 mW for (B)-(E); T = 15K.
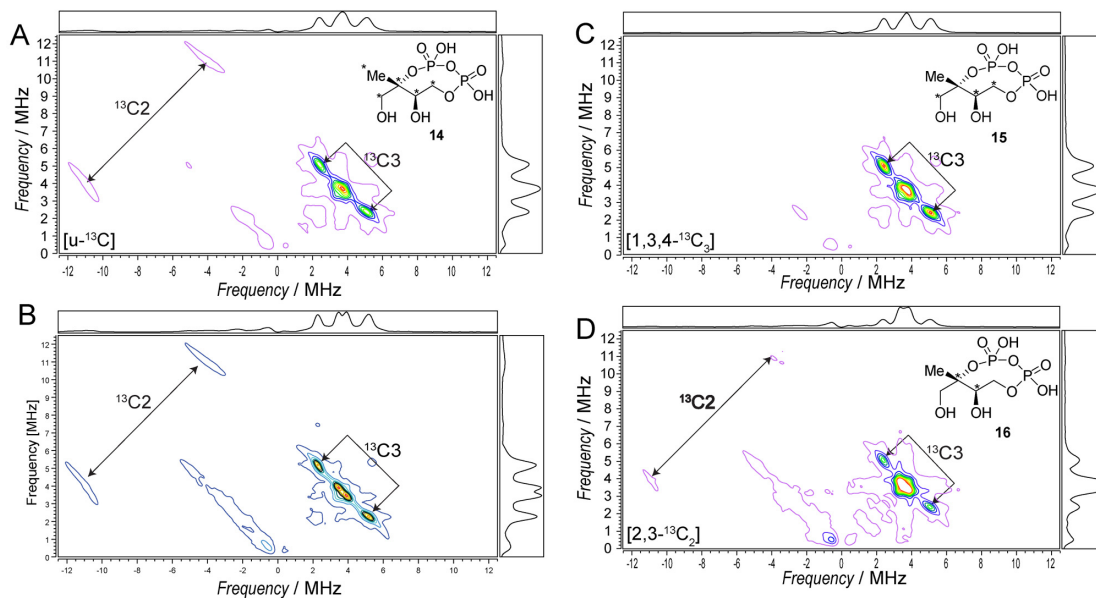
**Figure 2.3.** X-band HYSCORE spectra at g_2 (g = 2.018) of the reaction intermediate "X" prepared from ^{13}C-labeled MEcPP. (A), [U-^{13}C]-MEcPP (**4**) + *E. coli* IspG. (B), [u-^{13}C] MEcPP (**4**) + *T. thermophilus* IspG. (C), [1,3,4-[13]C$_3$] MEcPP (**5**) + *E. coli* IspG. (D), [2,3-[13]C$_2$] MEcPP (**6**) + *E. coli* IspG. The weaker ^{13}C signals in D are due to low enrichment.[9] In (A)-(C), the diagonal peak at ~ 3.6 MHz is the superposition of ^{13}C signals having small (<1 MHz) hyperfine couplings from the labeled substrates and the double quantum transitions of protein ^{14}N, while in (D), this signal arise only from double quantum transitions of protein [14]N. τ = 136 ns. T = 20.0 K.
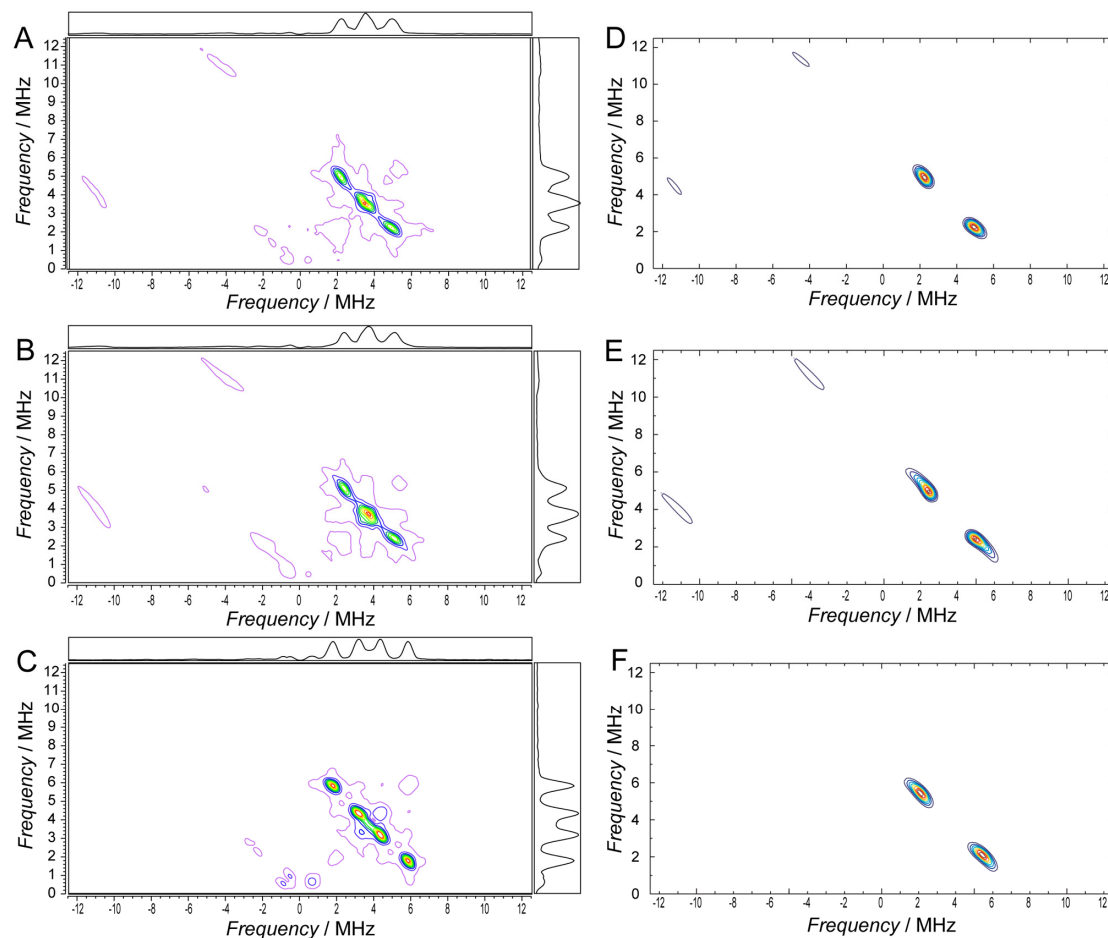
Figure 2.4. X-band HYSCORE spectra of the reaction intermediate "X" prepared by using *E. coli* IspG and [U-13C] MEcPP (**4**) at three different magnetic field strengths (left) and simulations of the C2 and C3 13C hyperfine signals (right). In (A)-(C), the signals at ~ 3.6 MHz are superpositions of 13C signals arising from very small hyperfine couplings (≤1 MHz) from the labeled substrates and protein 14N double quantum transitions and are not simulated. Experimental parameters are: microwave frequency = 9.684 GHz, τ = 136 ns and T = 20.0 K. Spectra were simulated using A = [14.5, 12.0, 26.5] MHz with Euler angles α = 0˚, β= 18˚, γ= 0˚ for C2, and A = [1.8, 2.0, 5.1] MHz with Euler angles α = 40˚, β= 30˚, γ= 0˚ for C3.
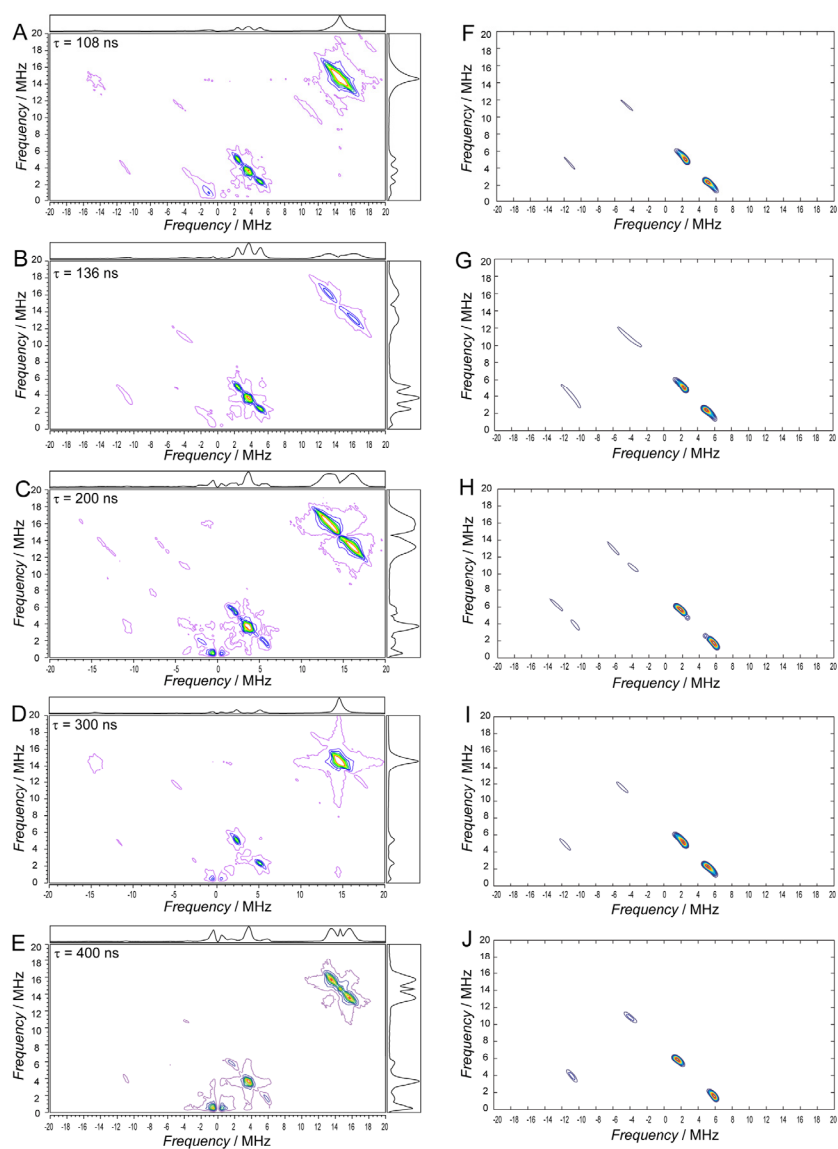
Figure 2.5. X-band HYSCORE spectra (left) at g_2 of the reaction intermediate "X", prepared by using **4**, at different τ values, together with simulations (right) of the 17.7 MHz and 3 MHz signals. (A)-(E) are experimental results at $\tau = 108$, 136, 200, 300 and 400 ns, respectively. (F)-(J) are simulations of (A)-(E). In (A)-(E), the signals at ~ 3.6 MHz are the superposition of ^{13}C signals with very small hyperfine couplings (≤ 1 MHz) from the labeled substrates and the protein ^{14}N double quantum transition, and are not simulated; the signals centered at 14.5 MHz are proton signals and are also not simulated. Experimental parameters are: microwave frequency = 9.674 GHz, magnetic field strength = 342.5 mT and $T = 20.0$ K.
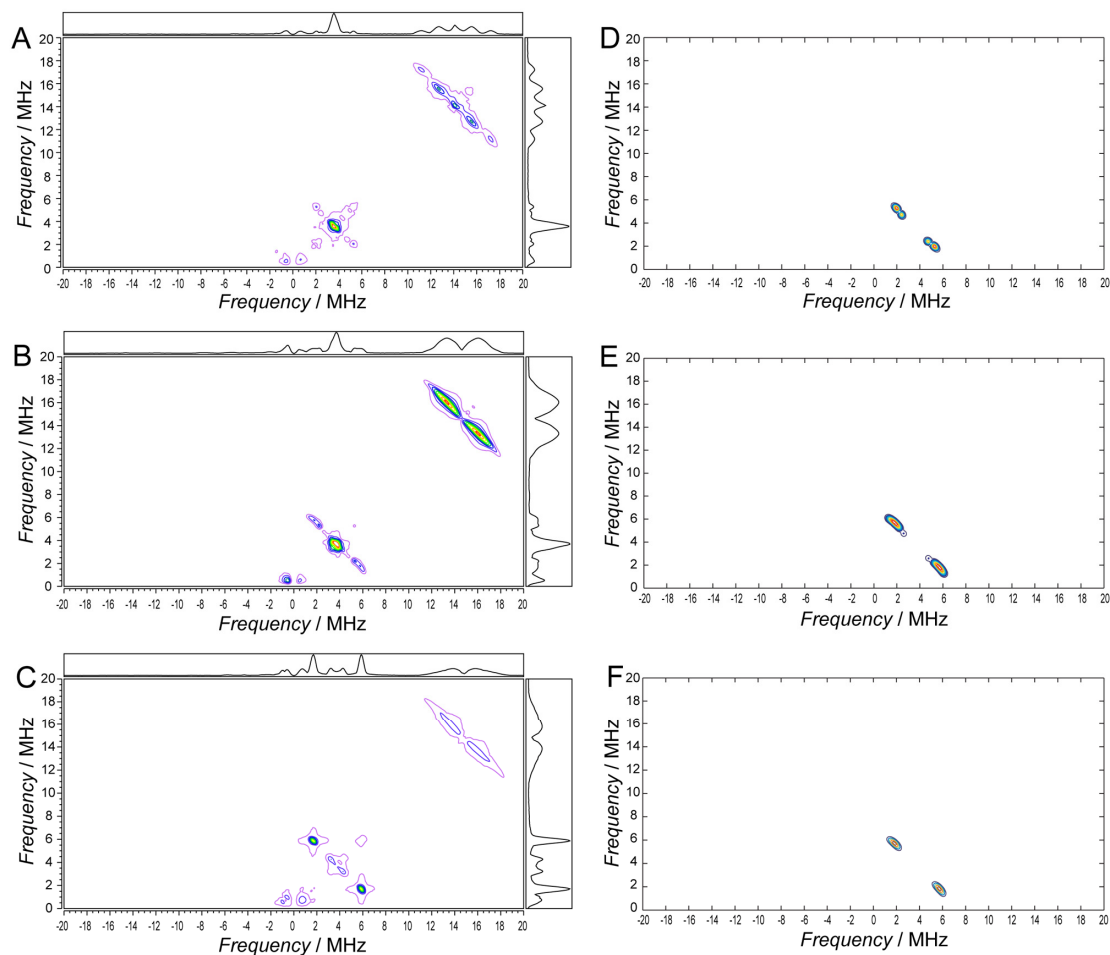
Figure 2.6. X-band HYSCORE spectra of the reaction intermediate "X" prepared by using *E. coli* IspG and **5** at three different magnetic field strengths (left), and simulations of the 3 MHz ^{13}C hyperfine signals (right). (A), magnetic field strength = 331.0 mT (*g* = 2.08). (B), magnetic field strength = 342.86 mT (*g* = 2.02). (C), magnetic field strength = 346.0 mT (*g* = 2.00); (D)–(F) are simulations of (A)-(C), respectively. In (A)-(C), the signals at ~ 3.6 MHz are superpositions of ^{13}C signals arising from very small hyperfine couplings (≤1 MHz) from the labeled substrates and protein ^{14}N double quantum transitions and are not simulated; the signals centered at 14.5 MHz are proton signals and are also not simulated. Experimental parameters are: microwave frequency = 9.684 GHz, τ = 200 ns and *T* = 20.0 K. Spectra were simulated using *A* = [1.8, 2.0, 5.1] MHz with Euler angles α = 40°, β= 30°, γ= 0° for C3.

34
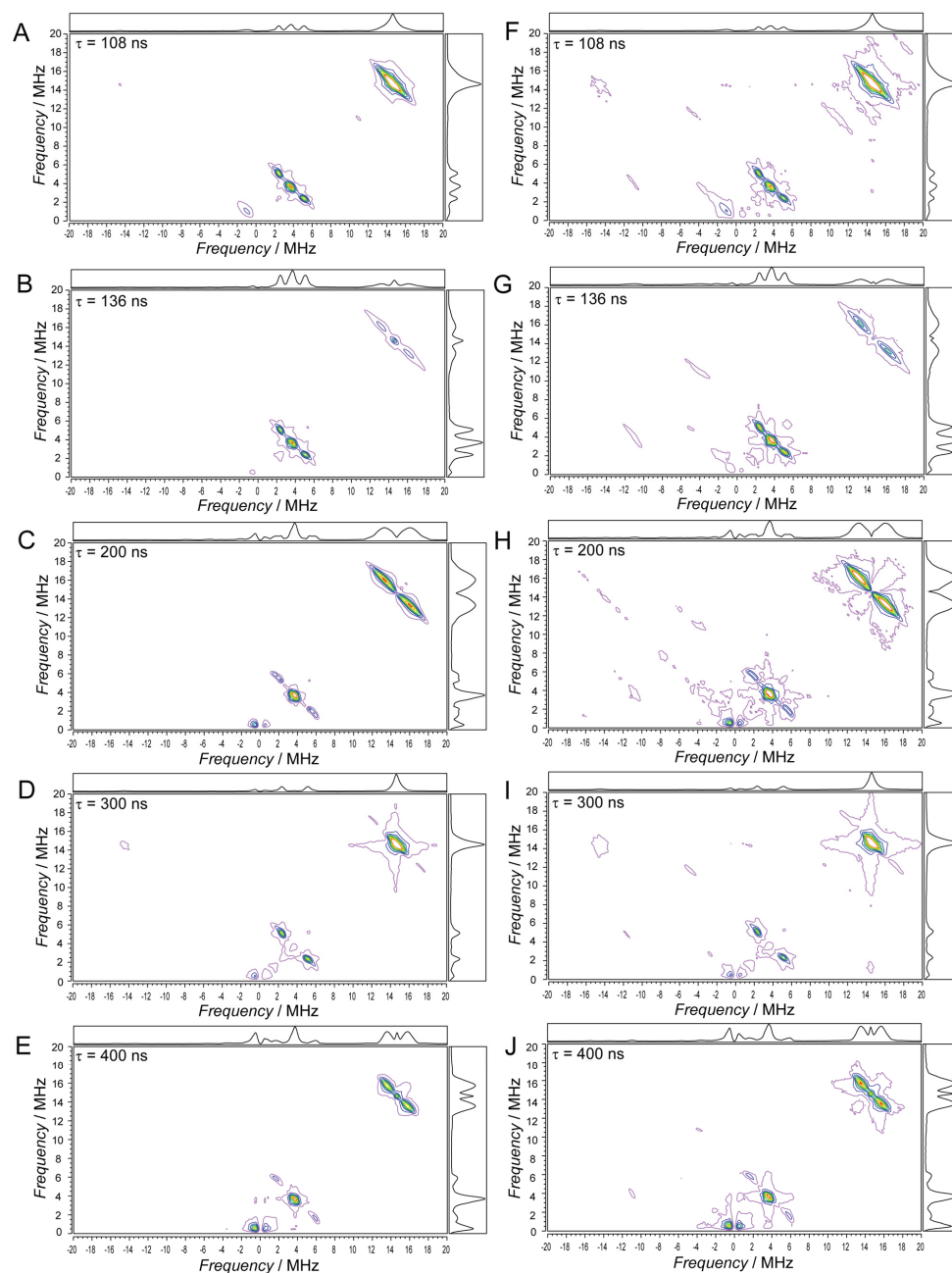
Figure 2.7. X-band HYSCORE spectra at g_2 of the reaction intermediate "X" prepared by using ^{13}C-labeled MEcPP at different τ-values. (A)-(E) are from the sample prepared using **5** and (F)-(J) are from the sample prepared using **4**. The signals at ~ 3.6 MHz are superpositions of ^{13}C signals having very small hyperfine couplings (≤ 1 MHz) from the labeled substrates, and the protein ^{14}N double quantum transitions. The signals centered at 14.5 MHz are proton signals. $T = 20.0$ K.
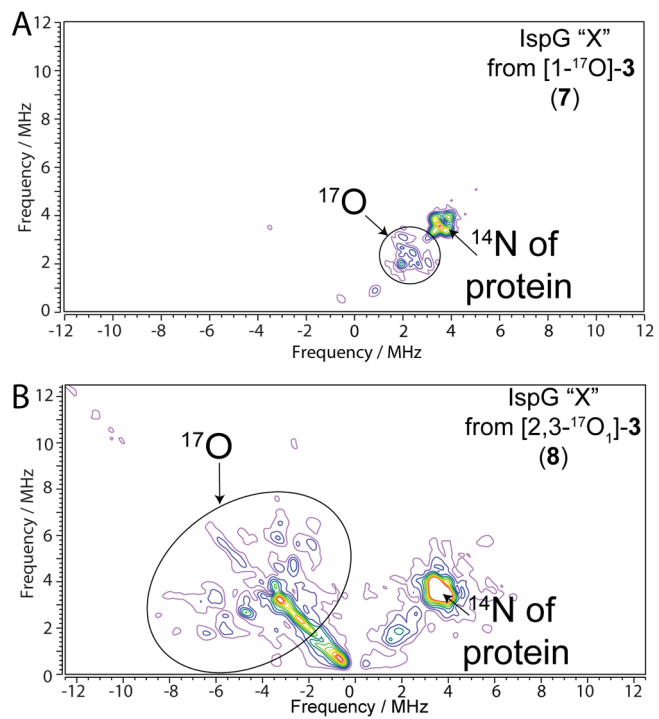
Figure 2.8. X-band HYSCORE spectra of "X" at g_2 prepared from ^{17}O labeled substrates **7** and **8**. (A), HYSCORE spectrum of "X" prepared from **7**. (B), HYSCORE spectrum of "X" prepared from **8**. $\tau = 136$ ns, $T = 18$ K.
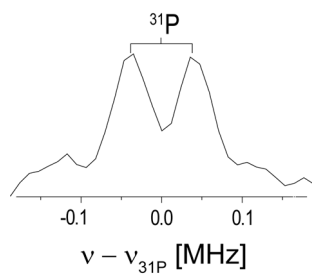
Figure 2.9. X-band ^{31}P Mims ENDOR of the reaction intermediate "X" collected at g_2. It is a sum of 12 spectra collected at different τ-values (248 - 336 ns). $T = 18$ K
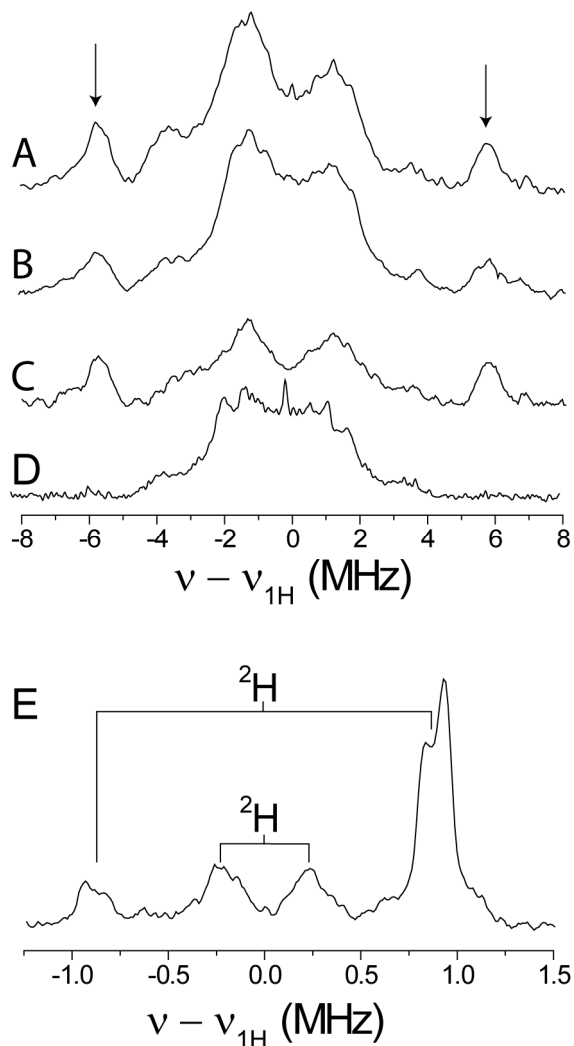
Figure 2.10. X-band $^1H/^2H$ ENDOR spectra of the reaction intermediate "X" at g_2 trapped with *T. thermophilus* IspG. (A), ^1H Davies ENDOR of "X" in H_2O buffer prepared using unlabeled MEcPP **2**. (B), ^1H Davies ENDOR of "X" in H_2O buffer prepared using unlabeled epoxide **3**. (C), ^1H Davies ENDOR of "X" in D_2O buffer prepared using unlabeled **2**. (D), ^1H Davies ENDOR of "X" in H_2O buffer prepared using [U-^2H]-**2**. (E), ^2H Mims ENDOR of "X" in H_2O buffer prepared using [U-^2H]-**2**, difference spectrum (^2H-labeled - unlabeled). $\pi/2_{mw}$ = 48 ns for Davies ENDOR experiments, 16 ns for Mims ENDOR experiment. (E). τ-averaging was used for collecting the Mims ENDOR spectrum (10 spectra at 8 ns steps with an initial τ = 248 ns). T = 20 K.
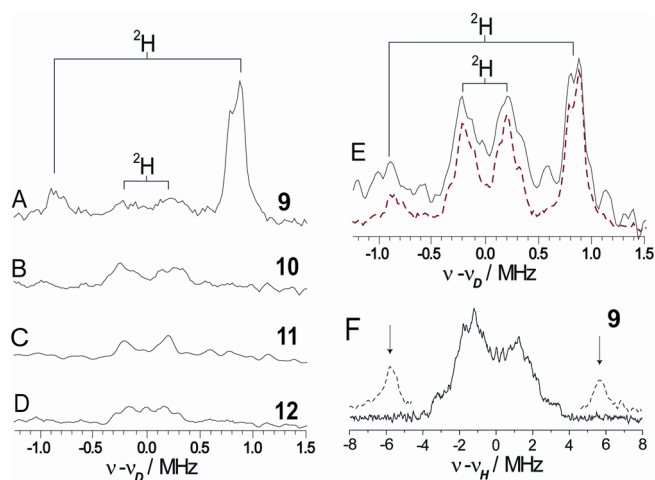
Figure 2.11. X-band ENDOR spectra at g_2 (g = 2.018) of the reaction intermediate "X" prepared using *E. coli* IspG and deuterated **2** or **3**. (A), Mims ENDOR spectrum of "X" prepared using **9**. (B), Mims ENDOR spectrum of "X" prepared using **10**. (C), Mims ENDOR spectrum of "X" prepared using **11**. (D), Mims ENDOR spectrum of "X" prepared using **12**. (E), the sum of (A) - (D) (solid black line). Mims ENDOR spectrum of "X" prepared using [U-^{2}H]-**2** collected under the same condition as (A) - (D) is shown in dashed red line, for comparison. (F), Davies ^{1}H ENDOR spectrum of "X" prepared using **9** (solid line), showing the disappearance of the a_{iso} = 12 MHz ^{1}H signal (dashed lines), indicated by arrows. Mims ENDOR spectra shown in (A)-(E) are the sums of spectra taken at 30 different τ-values (from 132 ns to 1060 ns, in 32 ns steps), and are normalized according to their ^{31}P signal intensity. The percentages of ^{2}H enrichment were also taken into account when adding (A)-(D). T = 20.0 K.
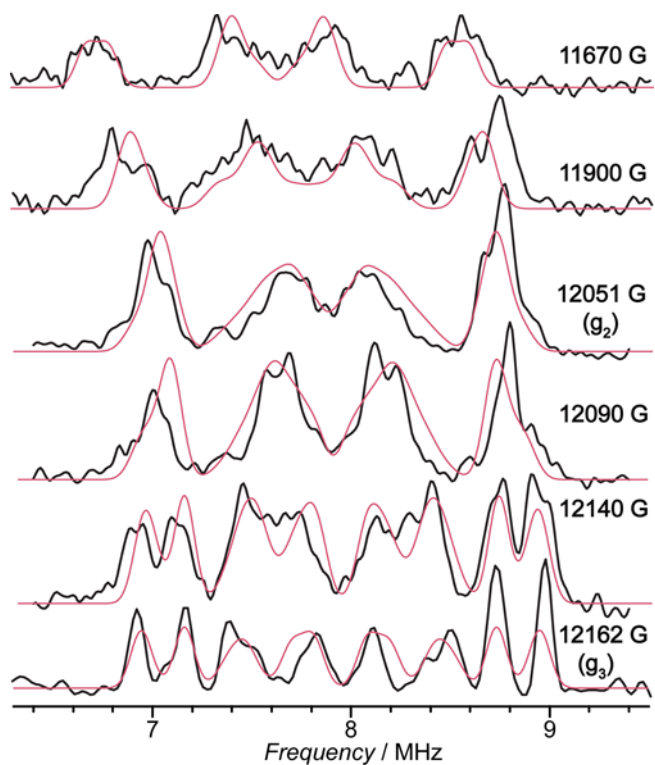
Figure 2.12. Q-band field-dependent Mims ENDOR spectra and simulations of "X" prepared using **9**. Black

lines: experimental data; red lines: simulations. Microwave frequency: 34.05 GHz; τ = 740 ns; T = 20K.

Simulation parameters: A (^2H_a) = [1.8, 1.6, 1.8] MHz; A (^2H_b) = [0.2, 0.0, 0.4] MHz; A (^2H_c) = [0.5, 0.1, 1.1]

MHz; $e2qQ/h$ = 168 kHz (^2H_a) and 160 kHz (^2H_b and ^2H_c).
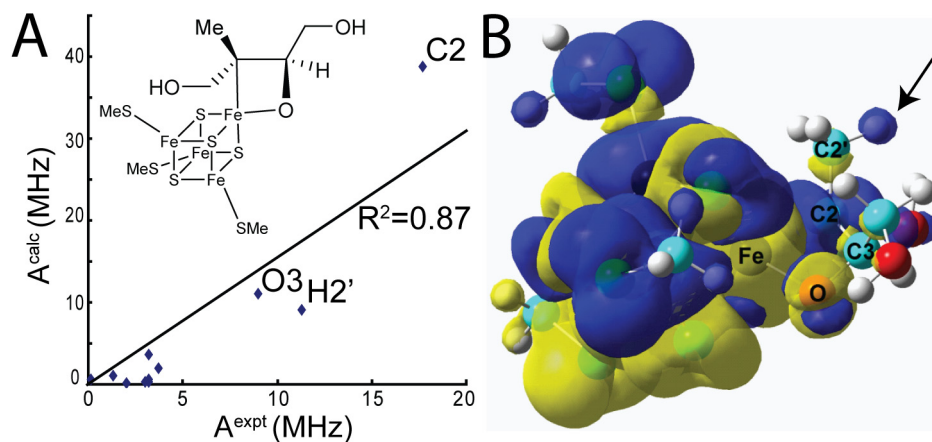
Figure 2.13. Experimental and computational results for the reaction intermediate "X". (A), correlation between computed hyperfine couplings (A_{iso}; Table 2.1) and experimental hyperfine couplings for H1(2), C2, H2′ (3), H3, H4(2), O1 and O3. The line is constrained through the origin and R=0.87, slope=1.55. The inset shows the model used for performing the calculation. (B), spin density for the ferraoxetane model. One methyl proton (indicated by the arrow) has a very large (~12 MHz) coupling and originates from a trans (Fe-C2-C2′-H2′) hyperfine interaction.

Table 2.1. Calculated A_{iso} for the ferraoxetane reaction intermediate model and A_{iso} or A determined by experiments (A_{iso} was obtained from spectral simulations of orientation-selective data, and A was estimated from the ENDOR/HYSCORE spectra taken at g_2).

	calculated A_{iso} (MHz)	experimental A_{iso} or A (MHz)
C1H1	0.6	$A = 3.2$
C1H2	0.3	$A = 3.2$
C2	38.9	$A_{iso} = 17.7$
C2'H1	9.1	$A_{iso} = 11.3$
C2'H2	2.0	$A = 3.7$
C2'H3	1.1	$A = 1.3$
C3	0.3	$A_{iso} = 3$
C3H	3.6	$A = 3.2$
C4H1	0.3	$A = 3.2$
C4H2	0.2	$A = 2.0$
O1	0.68	$A = 0.15$
O3	11.4	$A = 9$

2.7 References

(1) Hecht, S.; Eisenreich, W.; Adam, P.; Amslinger, S.; Kis, K.; Bacher, A.; Arigoni, D.; Rohdich, F. *Proc. Nat. Acad. Sci. USA* 2001, *98*, 14837.

(2) Seemann, M.; Wegner, P.; Schunemann, V.; Bui, B. T.; Wolff, M.; Marquet, A.; Trautwein, A. X.; Rohmer, M. *J Biol Inorg Chem* 2005, *10*, 131.

(3) Adedeji, D.; Hernandez, H.; Wiesner, J.; Kohler, U.; Jomaa, H.; Duin, E. C. *FEBS Lett* 2007, *581*, 279.

(4) Kollas, A. K.; Duin, E. C.; Eberl, M.; Altincicek, B.; Hintz, M.; Reichenberg, A.; Henschker, D.; Henne, A.; Steinbrecher, I.; Ostrovsky, D. N.; Hedderich, R.; Beck, E.; Jomaa, H.; Wiesner, J. *FEBS Lett* 2002, *532*, 432.

(5) Seemann, M.; Bui, B. T.; Wolff, M.; Tritsch, D.; Campos, N.; Boronat, A.; Marquet, A.; Rohmer, M. *Angew Chem Int ed* 2002, *41*, 4337.

(6) Brandt, W.; Dessoy, M. A.; Fulhorst, M.; Gao, W.; Zenk, M. H.; Wessjohann, L. A. *Chembiochem* 2004, *5*, 311.

(7) Rohdich, F.; Zepeck, F.; Adam, P.; Hecht, S.; Kaiser, J.; Laupitz, R.; Grawert, T.; Amslinger, S.; Eisenreich, W.; Bacher, A.; Arigoni, D. *Proc Natl Acad Sci U S A* 2003, *100*, 1586.

(8) Nyland, R. L. n.; Xiao, Y.; Liu, P.; Freel Meyers, C. L. *J Am Chem Soc* 2009, *131*, 17734.

(9) Wang, W.; Li, J.; Wang, K.; Huang, C.; Zhang, Y.; Oldfield, E. *Proc Natl Acad Sci USA* 2010, *107*, 11189.

(10) Silakov, A.; Wenk, B.; Reijerse, E.; Albracht, S. P.; Lubitz, W. *J Biol Inorg Chem* 2009, *14*,

301.

(11) Shanmugam, M.; Zhang, B.; McNaughton, R. L.; Kinney, R. A.; Hille, R.; Hoffman, B. M. *J Am Chem Soc* 2010, *132*, 14015.

(12) Werst, M. M.; Kennedy, M. C.; Beinert, H.; Hoffman, B. M. *Biochemistry* 1990, *29*, 10526.

(13) Kennedy, M. C.; Werst, M.; Telser, J.; Emptage, M. H.; Beinert, H.; Hoffman, B. M. *Proc Natl Acad Sci U S A* 1987, *84*, 8854.

(14) Xu, W.; Lees, N. S.; Adedeji, D.; Wiesner, J.; Jomaa, H.; Hoffman, B. M.; Duin, E. C. *J Am Chem Soc* 2010, *132*, 14509.

(15) Hashmi, A. S.; Hutchings, G. J. *Angew Chem Int ed* 2006, *45*, 7896.

(16) Calhorda, M. J.; Galvao, A. M.; Unaleroglu, C.; Zlota, A. A.; Frolow, F.; Milstein, D. *Organometallics* 1993, *12*, 3316.

(17) Kafafi, Z. H.; Hauge, R. H.; Billups, W. E.; Margrave, J. L. *J Am Chem Soc* 1987, *109*, 4775.

(18) Backvall, J. E.; Bokman, F.; Blomberg, M. R. A. *J Am Chem Soc* 1992, *114*, 534.

(19) Sharpless, K. B.; Teranishi, A. Y.; Backvall, J. E. *J Am Chem Soc* 1977, *99*, 3120.

(20) Itoh, T.; Nagano, T.; Sato, M.; Hirobe, M. *Tetrahedron Lett* 1989, *30*, 6387.

(21) Frisch, M. J.; Trucks, G. W.; Schlegel, H. B.; Scuseria, G. E.; Robb, M. A.; Cheeseman, J. R.; Scalmani, G.; Barone, V.; Mennucci, B.; Petersson, G. A.; Nakatsuji, H.; Caricato, M.; Li, X.; Hratchian, H. P.; Izmaylov, A. F.; Bloino, J. Z., G.; Sonnenberg, J. L. H., M.; Ehara, M.; Toyota, K.; Fukuda, R.; Hasegawa, J.; Ishida, M.; Nakajima, T.; Honda, Y.; Kitao, O.; Nakai, H.; Vreven, T.; Montgomery, Jr., J. A.; Peralta, J. E.; Ogliaro, F.; Bearpark, M.; Heyd, J. J.;

Brothers, E.; Kudin, K. N.; Staroverov, V. N.; Kobayashi, R.; Normand, J.; Raghavachari, K.; Rendell, A.; Burant, J. C.; Iyengar, S. S.; Tomasi, J.; Cossi, M.; Rega, N.; Millam, N. J.; Klene, M.; Knox, J. E.; Cross, J. B.; Bakken, V.; Adamo, C.; Jaramillo, J.; Gomperts, R.; Stratmann, R. E.; Yazyev, O.; Austin, A. J.; Cammi, R.; Pomelli, C.; Ochterski, J. W.; Martin, R. L.; Morokuma, K.; Zakrzewski, V. G.; Voth, G. A.; Salvador, P.; Dannenberg, J. J.; Dapprich, S.; Daniels, A. D.; Farkas, Ö.; Foresman, J. B.; Ortiz, J. V.; Cioslowski, J.; Fox, D. J.; Gaussian, Inc., Wallingford CT: 2009.

(22) Wang, W.; Li, J.; Wang, K.; Smirnova, T. I.; Oldfield, E. *J. Am. Chem. Soc.* 2011, *133*, 6525.

(23) Wang, W.; Wang, K.; Li, J.; Nellutla, S.; Smirnova, T. I.; Oldfield, E. *J Am Chem Soc* 2011, *133*, 8400.

(24) Wang, K.; Wang, W.; No, J. H.; Zhang, Y.; Zhang, Y.; Oldfield, E. *J Am Chem Soc* 2010, *132*, 6719.

(25) Schmidt, T. G.; Skerra, A. *Nature protocols* 2007, *2*, 1528.

(26) Stoll, S.; Schweiger, A. *J Magn Reson* 2006, *178*, 42.

Chapter 3

Bioorganometallic Mechanism of Action

of the [4Fe-4S] Protein IspH

3.1 Notes and Acknowledgement

3.2 Introduction

IspH (also known as LytB, EC 1.17.1.2) is the last enzyme in the non-mevalonate isoprenoid biosynthesis pathway.[1] It contains a [4Fe-4S] cluster with one unique fourth iron not coordinated to any cysteine ligand,[2-4] and catalyzes the $2H^+/2e^-$ reduction of (*E*)-4-hydroxy-3-methyl–but-2 -enyl-1-diphosphate (HMBPP, **1**) to form a ~5:1 mixture of isopentenyl diphosphate (IPP, **2**) and dimethylallyl diphosphate (DMAPP, **3**),[5] shown in Scheme 3.1. The mechanism of action of IspH has been a mystery for several years, and there have been many different proposals involving distinct cationic, radical, radical anion, anionic, or diene intermediates [2,5-9] (Figure 3.1). However, none of these detailed mechanistic models has yet been supported by any spectroscopic evidence. When I started working on this project (the year 2008), it has been proposed that the substrate **1** binds to IspH as an alkoxide complex containing a Fe-O4 bond, based on a computational docking study.[10] Later, this binding mode was directly observed in an X-ray crystal structure of IspH:**1** complex.[11] Then, after the formation of the alkoxide complex as the initial binding mode, what are the following steps that lead to the final products **2** and **3**?

Scheme 3.1. Reaction catalyzed by IspH, and two substrate analogs used in this study.

In this chapter, I will address the catalytic mechanism of IspH from four aspects. First, I will study the roles of several totally conserved amino acid residues in catalysis, by characterizing enzyme kinetics of IspH mutants; Second, I will report the electron paramagnetic resonance (EPR) characterization of a reaction intermediate trapped with unreactive IspH E126A/E126Q mutant, and discuss its relevance to IspH catalysis; Third, I will describe the EPR characterization of an intermediate trapped with the wild type IspH enzyme, and its role in IspH catalysis; and finally, I will address the reaction of two non-natural substrates, a fluoro-substituted HMBPP (**4**) and an isomer of HMBPP (**5**). These studies, together with the ^{57}Fe-Mössbauer spectroscopic result[4] and X-ray crystallographic results[12,13] reported by others, lead to a bioorganometallic reaction mechanism where Fe-C interactions play important roles, and no radical intermediates are involved.

3.3 Results and Discussion

3.3.1 Roles of amino acid residues in catalysis

I first investigated roles of several totally conserved protein residues in IspH catalysis. In previous work, Oldfield and co-workers noted that E126, His42 and His124 in *Aquifex aeolicus* IspH were all totally conserved residues, and are located in the active site region.[10] Therefore, these residues are likely essential for the catalysis. However, the exact roles of these residues were unclear. I thus determined the K_M and V_{max} values for three *Aquifex aeolicus* IspH mutants: H42A, H124A and E126A.

In the case of the E126A mutant, activity was so low ($V_{max} < 0.025$ μmol min^{-1} mg^{-1}) that K_M could not be measured. This low activity is consistent with the proposed role of E126 as a proton donor for removing the substrate 4-OH group, as suggested by a computational docking result,[10] and is later confirmed in an X-ray crystal structure of IspH:**1** complex, where the 4-OH group of **1** forms a hydrogen bond with the carboxyl group of the E126 residue.[13]

With the H124A mutant, I found that although V_{max} was low (0.05 μmol min^{-1} mg^{-1} versus 1.16 μmol min^{-1} mg^{-1} for the wild type enzyme), K_M was essentially unchanged (7 μM versus 5 μM, for the wild type enzyme). This indicates that H124 is not a major contributor to substrate binding, but is essential for catalysis, suggesting that H124 may be involved in delivering H$^+$ to E126 and the bound substrate HMBPP.

In the case of H42, however, I found an increase in K_M (from 7 to 74 μM), indicating a role in substrate binding, consistent with the crystallographic observation that H42 is hydrogen bonded to a bound diphosphate ligand.[6] There is, nevertheless, also a 5 fold decrease in V_{max}, due

perhaps to the possibility that several more distal residues could also be involved in proton transfer.

3.3.2 The reaction intermediate trapped with IspH E126A/E126Q mutants

As discussed above, E126 is a key catalytic residue. If E126 is inactivated by mutagenesis (to alanine or glutamine), this should block catalysis, and might enable observation of an early reaction intermediate. Indeed, a reaction intermediate was trapped with *A. aeolicus* IspH E126A mutant (Figure 3.2B), characterized by g = [2.124, 1.999, 1.958], very different to the result obtained with ligand-free wild type *A. aeolicus* IspH (Figure 3.2A). A similar intermediate was obtained with an *E. coli* IspH E126Q mutant, characterized by g = [2.132, 2.003, 1.972] (Figure 3.2C).

Could this intermediate be a carbon radical, as suggested in previous mechanistic proposals (Figure 3.1)? To test this possibility, I first prepared [57]Fe labeled *A. aeolicus* IspH. The spectrum is broadened with the [57]Fe-labeled sample (Figure 3.2D), indicating that most of the spin density is on the iron-sulfur cluster, therefore it is unlikely to be a carbon-based free radical. This result is consistent with ^{13}C electron nuclear double resonance (ENDOR) spectrum of IspH E126A + [U-[13]C$_5$]-**1**, which shows only small ^{13}C hyperfine couplings (Figure 3.2E).

To test if this reaction intermediate is an alkoxide complex containing a Fe-O bond, just as when **1** binds to the oxidized wild type IspH,[10,11] we prepared [4-[17]O]-labeled **1** (70% [17]O enrichment), and carried out an [17]O-hyperfine sublevel correlation (HYSCORE) investigation. HYSCORE spectra of the *E. coli* IspH E126Q mutant + [4-[17]O]-labeled **1** collected at three different τ-values show the presence of only a very weak [17]O hyperfine interaction (~1 MHz,

Figure 3.2F). In other iron-sulfur proteins (*e.g.* aconitase), Fe-O bonding usually results in ∼ 8-15

MHz ^{17}O hyperfine coupling.[14,15] So, the very small ^{17}O hyperfine coupling observed here

indicates lack of direct Fe-O bonding and, most likely, the 4-^{17}OH group of **1** is simply rotated

away from the unique 4th iron of the cluster on reduction to $[4Fe-4S]^+$. This is consistent with a

crystallographic result showing a critical rotation of the 4-OH group of **1** during catalysis.[13] A

very recent report on the stereochemical course of IspH catalysis using deuterated compounds

also support the rotation of the 4-OH group.[16]

Therefore, this reaction intermediate is not a free radical, and it is not an alkoxide complex.

Then, what is the possible structure of this intermediate? Interestingly, in a literature search I

fortuitously found that its **g** tensor is quite similar to those seen with ethylene and allyl alcohol

bound to the α-70^{Ala} mutant of a nitrogenase FeMo cofactor protein (ethylene: **g** = [2.123, 1.978,

1.949];[17] allyl alcohol: **g** = [2.123, 1.998, 1.986][18]) with, on average, only a |0.01| difference

between the IspH and nitrogenase **g**-values. In nitrogenase, ethylene and allyl alcohol have been

shown (via ENDOR and/or density functional theory calculations[17-19]) to bind as "metallacycles"

(Figure 3.2G). And since **1** is simply a substituted alkene, one possible explanation of the

E126A+**1** spectrum is that **1** binds to the reduced IspH in a similar manner, that is, as a

π-complex/metallacycle (Figure 3.2H).[20]

Do I have more evidence to support that there is indeed interactions between the π-system of

1 and the $[4Fe-4S]^+$ cluster of IspH? I next compared the **g** tensor of this intermediate with a

series of 80 other [4Fe-4S] cluster-containing proteins, Table 3.1. These included various

ferredoxins; [4Fe-4S] enzymes and synthetic models; typical HiPIPs; nitrogenase, benzoyl CoA

51

reductase, as well as IspG and IspH with alkene/alkyne ligands (previously unpublished spectra are shown in Figure 3.3). For ease of comparison, g_{iso} *versus* Δg ($\Delta g = g_{11}\text{-}g_{33}$) values are shown plotted in Figure 3.4. There appear to be three major clusters: (A) classic $[4Fe\text{-}4S]^+$ clusters[21] containing primarily σ-bonded ligands (black squares), such as ferredoxins, aconitase, and ligand-free IspH/IspG in which $g_{iso} < g_e$. (B) typical oxidized HiPiPs ($[4Fe\text{-}4S]^{3+}$, red circles), with $g_{iso} > g_e$. And (C), $[4Fe\text{-}4S]^+$ clusters with alkene or alkyne ligands (blue triangles) where $g_{iso} > g_e$ (but are generally smaller than those of typical HiPIPs). As can be seen in Figure 3.4, the reaction intermediates trapped with IspH E126A/E126Q mutants fall in class C, all of which have unsaturated ligands, such as nitrogenase liganded with alkenes. These unusual HiPIP-like g-values presumably reflect weak interactions between the metal cluster and the π-system of the ligand, where M → L back-bonding would make the iron-sulfur clusters electron-deficient, similar to the conventional oxidized HiPIP clusters. In this context, the olefinic π-system of substrate **1** (as well as the acetylene inhibitors) would be the key structural element involved in interacting with the iron-sulfur cluster, rather than the 4-OH group, which has rotated away from the cluster.

Taken together, this EPR-detected intermediate represents the 4-OH rotated π-complex/metallacycle (Figure 3.2H). Considering the longer Fe-C distances[13] observed in the crystal structure of a 4-OH rotated IspH:**1** complex than those observed in classical organometallic π-complexes/metallacycles, and the fact that the C2-C3 carbons and their attached atoms are essentially planar in above mentioned crystal structure, this intermediate is more appropriately described as a weak π or van der Waals complex.

### 3.3.3 The reaction intermediate trapped with wild type IspH

I next studied the reaction of wild type IspH with the natural substrate **1**. By freeze-quenching the reaction within 30 seconds in the presence of excess dithionite, a new paramagnetic reaction intermediate was trapped, characterized by g = [2.171, 2.010, 1.994] (Figure 3.5A) - a different g tensor to those seen observed with the IspH E126A/E126Q mutants. The 4-OH group is likely to be removed in this reaction intermediate, since the E126 residue is present. Therefore, this is possibly the next reaction intermediate in the reaction pathway. This is consistent with the result of [17]O-HYSCORE experiments on this intermediate, prepared by using [4-[17]O]-**1** (Figure 3.5D), which gave no evidence for [17]O hyperfine interactions. Notably, this reaction intermediate does not have a normal [4Fe-4S]$^+$ cluster, either. Its g_{iso} value is 2.06, greater than the free electron g-value (g_e = 2.0023) and is more akin to that seen in HiPIP proteins.[21] And unlike the intermediate trapped with IspH E126A/E126Q mutants, which I propose is a weak π-complex formed between the unreactive mutant and the alkene **1**, this intermediate was trapped under turnover conditions. How, then, might a [4Fe-4S]$^{3+}$-like cluster be generated during catalysis?

In fact, very similar results have been found with other [4Fe-4S] proteins catalyzing 2H$^+$/2e$^-$ reductions. For example, in both IspG [22,23] as well as ferredoxin:thioredoxin reductase (FTR)[24-26] EPR spectra of reaction intermediates are both characterized by g_{iso} > 2. In addition, the EPR signals both have unusual relaxation properties, being observable without broadening at 77 K or even higher temperature. The same result was also observed with this IspH intermediate (Figure 3.5B). FTR is a well-characterized system and it is thought that its [4Fe-4S]$^{2+}$ cluster undergoes a

one-electron reduction followed by a two-electron reaction of a disulfide bond, yielding a HiPIP-type $[4Fe-4S]^{3+}$ cluster, thus avoiding generation of a thiol free radical.[25,26] As shown in Scheme 3.2, IspG as well as IspH catalytic mechanisms can all be cast in essentially the same manner as proposed for FTR catalysis. In each case, following a one-electron reduction of the $[4Fe-4S]^{2+}$ cluster (intermediate I), the resulting $[4Fe-4S]^+$ (intermediate II) carries out a two-electron reduction of its substrate, generating an oxidized HiPIP-like cluster $[4Fe-4S]^{3+}$ (intermediate III). There are two paramagnetic intermediate in this reaction mechanism of IspH catalysis, intermediate II and III. In this context, the intermediate trapped with IspH E126A/E126Q mutants is intermediate II (the 4-OH group rotated π-complex), and the intermediate trapped with wild type IspH is intermediate III (the η^3-allyl complex). Interestingly, an η^3-allyl reaction intermediate was previously observed in the X-ray crystal structure of IspH:**1** complex after X-ray irradiation, which is possibly the intermediate III observed here by EPR spectroscopy. In the X-ray crystal structure of this η^3-allyl species, the Fe-C distance (2.6-2.7 Å) is shorter than the sum of van der Waals radii of iron and carbon (3.6 Å), indicating a direct Fe-C interaction. However, it is not possible to rule out the possibilities that this crystallographically observed species is a IspH:**3** complex, or a diamagnetic η^3-allyl intermediate formed by a one-electron reduction of the paramagnetic η^3-allyl complex.

But what about other possibilities for this intermediate trapped with wild type IspH - is it possible that it is an allyl radical? This seems unlikely, for the following three reasons. First, the ***g*** tensor is highly anisotropic, while typical organic radicals have isotropic ***g*** tensors. Second, the EPR linewidth is significantly broadened with ^{57}Fe-enriched IspH (Figure 3.5C) due to

unresolved large ^{57}Fe hyperfine coupling interactions, indicating that most of the spin density is on the [4Fe-4S] cluster. Third, the intermediates prepared from [2-^{2}H$_1$]-**1** or [4-^{2}H$_1$]-**1** have only small deuterium hyperfine coupling constants ($A_y \sim 0.5$ MHz and 0.9 MHz, respectively, Figures 3.5E and F), much smaller than those of allyl radicals.[27] Therefore, this intermediate is not a radical.
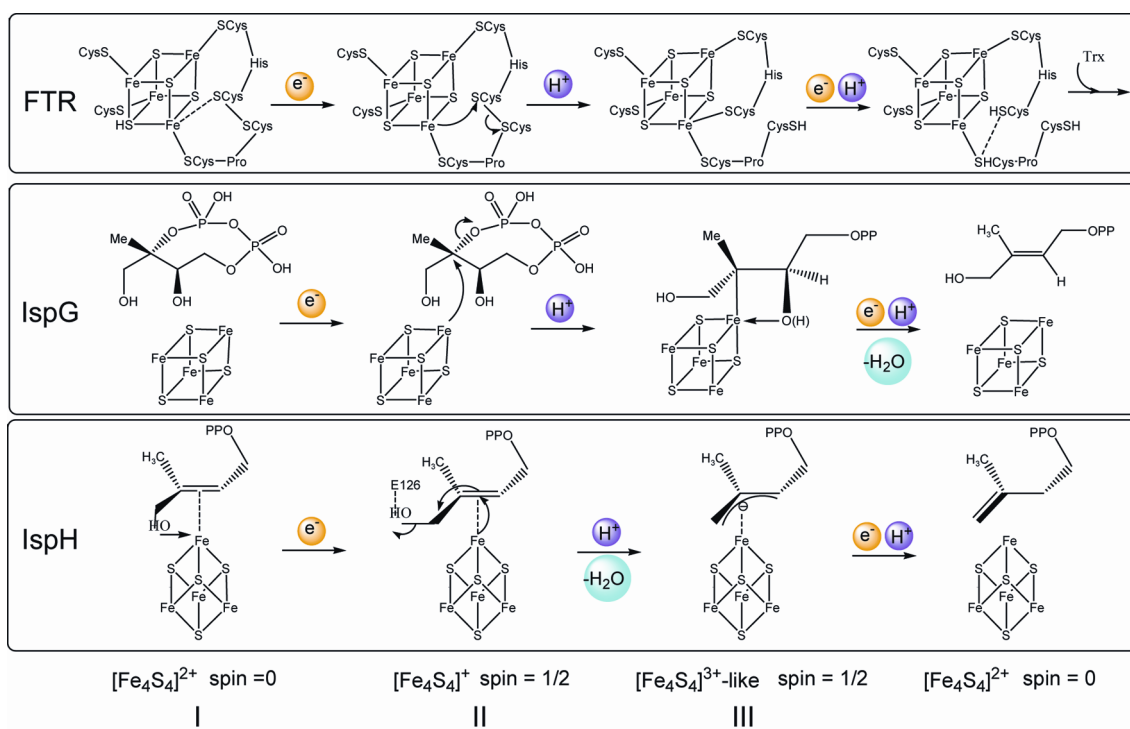
Scheme 3.2. Unified reaction mechanisms of action of FTR, IspG and IspH

### 3.3.4 Reaction with the fluoro substrate analog

With IspH E126Q mutant, **4** generates the same reaction intermediate as **1** does. The EPR spectrum of this intermediate (Figure 3.6A) is essentially identical to the spectrum obtained with **1** itself (Figure 3.2C). This suggests two possibilities: first, when bound to the reduced cluster,

the fluorine of **4** hydrolyzes to afford **1**; second, the fluorine group in **4** rotates away from the [4Fe-4S]$^+$ cluster, just as **1** does. Both possibilities are consistent with the ^{19}F-HYSCORE result of E126Q + **4** (Figure 3.6B) taken at three different τ-values, which shows no evidence of any ^{19}F hyperfine interaction - an observation that also rules out any significant Fe-F bonding proposed in some models.[28] This indicate as **1**, **4** forms a weak π-complex (intermediate II) with the [4Fe-4S]$^+$ cluster of IspH.

Also, with wild type IspH, **4** generates the same reaction intermediate as **1** does. The EPR spectrum of this intermediate (Figure 3.6C) is identical to that obtained with **1** and wild type IspH, indicating the formation of intermediate III. This is consistent with the HYSCORE result of this intermediate, which shows no ^{19}F singal (Figure 3.6D). Overall, these results indicate the non-natural substrate **4** follows the same reaction mechanism as the natural substrate **1**.

3.3.5 Reaction with substrate analog *iso*-HMBPP

Finally, we investigated the reaction of IspH with its substrate analog, *iso*-HMBPP (**5**). Liu and co-workers found that [5-^{13}C$_1$]-**5** only afforded one product, **6**; **7** was not detected (Scheme 3.3):[29]
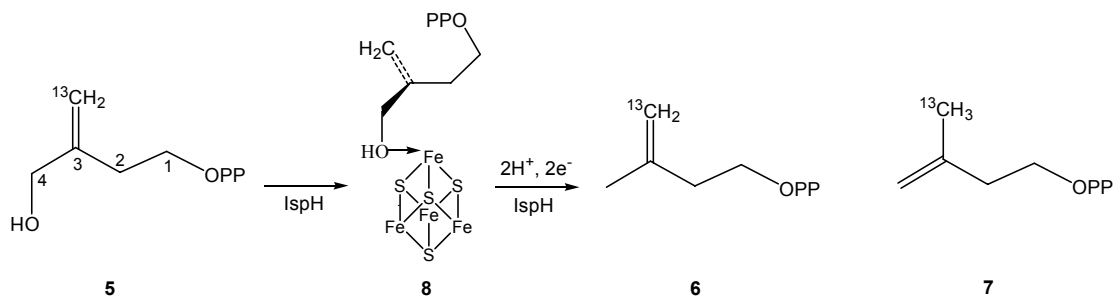
Scheme 3.3. The reaction of **5** with IspH.

Based on this result, it has been proposed that: (i) this was due to the formation of the alkoxide complex **8**, which positioned the C5 carbon away from the proton source, the diphosphate oxygen, so that C5 was not protonated in the reaction; (ii) the fact that **6** being the sole product indicated the interaction between the π-bond of **5** (or **1**) and the [4Fe-4S] cluster was not involved in catalysis, and (iii) the two electrons were delivered one after another, generating radical intermediates.[28,29] Thus, these workers favored a Birch reduction-like mechanism, shown in Scheme 3.4. To test these hypotheses, we obtained the x-ray crystal structure of IspH:**5** complex, and studied the reaction using EPR spectroscopy. The results do not support the latter two hypotheses.
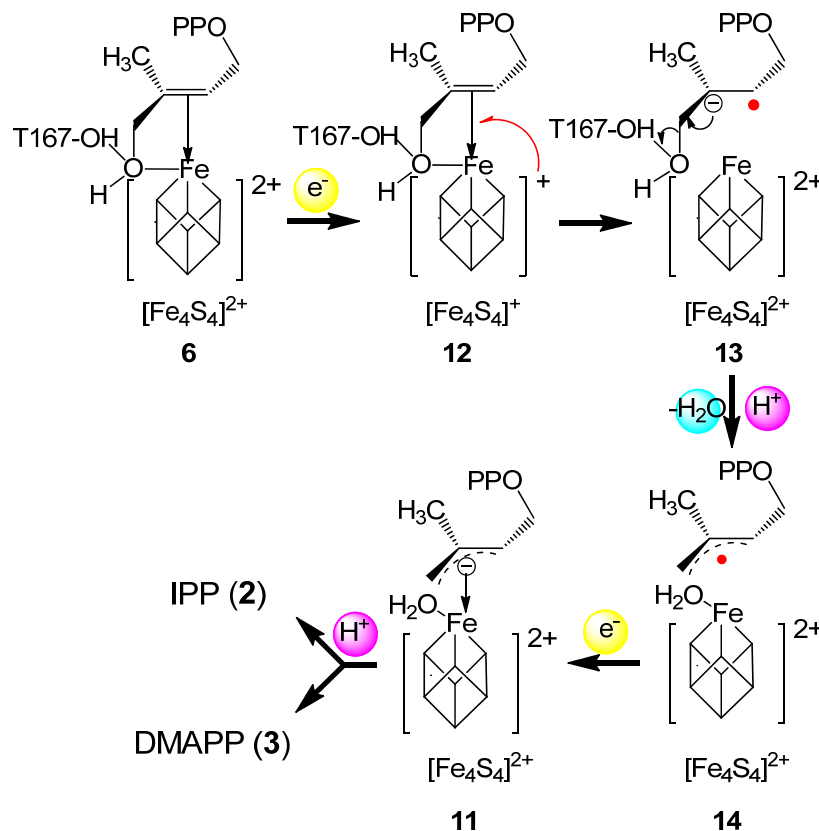

Scheme 3.4. The proposed Birch reduction-like mechanism of IspH catalysis.[28,29]

First, although the initial intermediate, the alkoxide complex **8** was indeed observed (Figures 3.7A, B), this is as expected and does not provide any information on π-interactions in subsequent reactions. As with the natural substrate **1**, on reduction of the [4Fe-4S] cluster, the presence of a π-interaction is supported by the EPR spectrum of IspH E126Q + **5** (Figure 3.7C) which shows two components, characterized by $\boldsymbol{g}_1$ = [2.091, 1.999, 1.999] with $g_{iso,1}$ = 2.030; and $\boldsymbol{g}_2$ = [2.091, 1.999, 1.982] with $g_{iso,2}$ = 2.024. The g_{iso}s of E126Q + **5** are greater than g_e, and fall in the type C region in Figure 3.4. This result suggests that on cluster reduction, the 4-OH group of **5** rotates away just as does **1**, so that the C=C can come closer to the [4Fe-4S]$^+$ cluster and interact with the unique 4th iron.

Second, the formation of the initial alkoxide complex **8** does not necessarily suggest a Birch reduction-like mechanism. As with **1**, we trapped a reaction intermediate within 30 seconds whose EPR spectrum was characterized by $\boldsymbol{g}$ = [2.171, 2.005, 2.005] (Figure 3.7D), essentially the same as the $\boldsymbol{g}$ tensor of the intermediate trapped with **1**, which we have assigned to the η^3-allyl complex having an oxidized HiPIP-like cluster (Intermediate III). This suggests that-as with **1**, the one-electron reduction of the IspH [4Fe-4S]$^{2+}$ cluster is followed by a two-electron reduction of **5**, yielding a HiPIP-type [4Fe-4S]$^{3+}$ cluster (in intermediate III), with no radicals observed. Taken together, our results clearly indicate **5** follows the same reaction mechanism as the natural substrate **1** (Scheme 3.5):
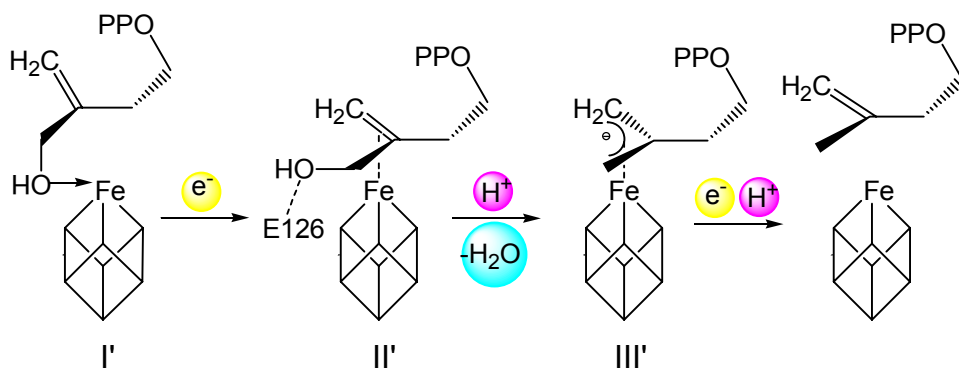
Scheme 3.5. Bioorganometallic reaction mechanism of IspH and *iso*-HMBPP **5**.

Why, then, is **6** the sole product of **5** reacting with IspH? Our results indicate that this is not due to the absence of a π-interaction, or to a radical reaction mechanism. It only indicates the proton source in the final protonation step, the diphosphate oxygen, is closer to C4 than C5, which is indeed suggested by the X-ray crystal structure of the IspH:**5** complex (Figure 3.7A). This crystal structure also provides a ready explanation as to why the K_m of **5** is 35 fold larger than that of **1**[29] – the average Fe-C3 and Fe-C5 distance in the alkoxide complex formed by **5** is 0.5 Å longer than that seen in the alkoxide complex formed by **1**.[11] Thus the π-interaction does not contribute much to the initial binding of **5**. However, as suggested by the EPR results (Figures 3.7C, D), C3 and C5 of **5** are likely to move closer to the iron-sulfur cluster on reduction, with the π-interaction playing a important role in the later catalytic steps, just as with **1**.

3.3.6 A Birch reduction-like mechanism does not fit experimental data

As discussed in section 3.3.5, the result of **5** reacting with IspH does not support a Birch reduction-like mechanism. Furthermore, the Birch reduction-like mechanism is unlikely for the

following four reasons. **(i)** In the Birch reduction mechanism, the 4-OH group binds to the reduced [4Fe-4S] cluster in **10** and is protonated by the T167 hydroxyl group in **11**. This contradicts the results of a computational docking study,[20] a crystal structure of an IspH:**1** complex,[13] the ^{17}O-HYSCORE data on intermediate II presented in section 3.3.2, as well as a recent report on the stereochemical course of IspH catalysis using deuterated compounds.[16] These results all indicate a rotation of the 4-OH group away from or off of the [4Fe-4S] cluster on reduction, after formation of the initial alkoxide complex **9** (intermediate I). This rotation enables the 4-OH group to be protonated and removed by the carboxyl group of E126, which is more acidic than the hydroxyl group of the T167. **(ii)** There are two radical species involved the Birch reduction-like mechanism. However, neither has been observed. The paramagnetic intermediate trapped with wild type IspH is likely to be an η^3-allyl complex; however, its **g** tensor, the deuterium hyperfine coupling constants, and the ^{57}Fe broadening effect all indicate this intermediate is not a radical. **(iii)** The Birch reduction-like mechanism cannot explain the identities of the paramagnetic intermediates trapped with either wild type IspH or the E126Q mutant. As discussed above, these intermediates are not a radicals, so cannot be **11** or **12**; they cannot be intermediate **10** either, because no sizeable ^{17}O hyperfine coupling signal was observed. Finally, these paramagnetic intermediates of course cannot be **9** or **13**, since they are diamagnetic. **(iv)** The cluster-bound water molecule in **12** and **13** is not observed in the crystal structure of the η^3-allyl complex.[11]

3.4 Conclusions

The results reported here strongly support the mechanism of IspH catalysis shown in Scheme 3.2. In this mechanism, no radical intermediate is involved; direct Fe-C interactions (e.g. in intermediate II and III) play important roles in catalysis. Therefore, we name this mechanism the bioorganometallic mechanism. Both paramagnetic reaction intermediates in this mechanism have been trapped and characterized in this study. The paramagnetic intermediate trapped with IspH E126A/E126Q mutants represents the terminal OH-rotated weak π-complex, intermediate II. Following a two-electron reduction and dehydration, intermediate II is convert into a HiPIP-like η^3-allyl complex, intermediate III, which is trapped with wild type IspH. Similar intermediates were obtained with substrate analogs **4** and **5,** indicating they follow the same bioorganometallic reaction mechanism. This reaction mechanism (as well as that of IspG) has very close similarities to that proposed for the ferredoxin-thioredoxin reductase reaction, in which HiPIP-like intermediates, but not free radicals, are involved. The two paramagnetic intermediates reported here do not fit the Birch reduction-like mechanism.

3.5 Materials and Methods

All chemicals were purchased from Sigma-Aldrich (St. Louis, MO) and were used as provided. ^{57}Fe metal was purchased from American Elements (Los Angeles, CA). The plasmid encoding wild type IspH from *Aquifex aeolicus* was the generous gift of Hassan Jomaa and Jochen Wiesner. The plasmid encoding the *E. coli* IspG was kindly provided by Pinghua Liu.

XL2-Blue ultracompetent cells and BL-21(DE3) competent cells were purchased from Stratagene (La Jolla, CA).

3.5.1 Site-directed mutagenesis

Primers were designed by using the on-line tool "QuickChange primer design" (https://www.genomics.agilent.com), and were synthesized by Integrated DNA Technologies (http://www.idtdna.com/Home/Home.aspx).   Point mutation was carried out using the Agilent QuickChange II Site-Directed Mutagenesis kit. In a typical PCR reaction, the following components were added into a PCR tube:

1 μL each primer (250 μg/mL);

5 μL 10X cloned Pfu DNA polymerase reaction buffer;

3 μL template plasmid from miniprep;

1 μL dNTP;

38 μL water;

1 μL Pfu turbo DNA polymerase.

Annealing temperature was set to 53 °C, and extension temperature to 68 °C. When the PCR reaction was done, 1μL DpnI enzyme was added to the reaction mixture and was incubated at 37 °C for ~ 2 hours, to digest the methylated template plasmids. Then, 10 μL of the resultant reaction mixture was subsequently transformed into XL1-Blue Ultracompetent cells (Stratagene) and spread onto LB plates with 100μg/mL ampicillin until colonies appeared. Individual colonies were grown in 5mL of LB medium with 100μg/mL ampicillin. The plasmids from an overnight culture were then extracted using the Qiagen (Valencia, CA) Miniprep. The plasmids were

sequenced at the core DNA sequencing facility at University of Illinois at Urbana-Champaign (http://www.biotech.uiuc.edu/centers/Keck/Core/), and the plasmid with the correct sequence chosen for expression and purification.

3.5.2 *E. coli* IspH protein expression and purification

BL-21(DE3) cells over-expressing *E. coli* IspH (encoded in plasmid pASK-IBA3$^+$) and *isc* proteins (encoded in plasmid pDB1282) were grown in LB media supplemented with 100 mg/l ampicillin and 50 mg/l kanamycin at 37 °C, until the OD_{600} reached 0.3. Cells were then induced with 0.5 g/l arabinose to initiate over-expression of the *isc* proteins. Cysteine (1 mM) and $FeCl_3$ (0.1 mM) were supplemented, and cells were grown until the OD_{600} reached 0.6. At this point, 400 µg/l anhydrotetracycline was added to induce over-expression of *E. coli* IspH. Cells were grown at 25 °C for 16 hours, harvested by centrifugation and kept at -80 °C until use.

All purification steps were carried out in a Coy Vinyl Anaerobic Chamber (Coy Laboratories, Grass Lake, MI) with an oxygen level < 2 ppm, and all buffers were degassed by using a Schlenk line. Cell pellets were re-suspended in 100 mM Tris-HCl, 150 mM NaCl buffer (pH 8.0). Lysozyme, Benzonase nuclease (EMD Chemicals, San Diego, CA) and phenylmethanesulfonyl fluoride were added, and stirred for one hour at 10 °C followed by sonication (Fisher Scientific Sonic Dismembrator, Model 500) with 4 pulses, each 7 s duration, at 35% power. The cell lysate was centrifuged at 11,000 rpm at 10 °C for 30 min. The supernatant was purified by using Strep-tactin chromatography. Fractions having a brown color were collected and desalted in pH 8.0 buffer containing 100 mM Tris-HCl and 150 mM NaCl.

3.5.3 Purification of *E. coli* IspH E126Q mutant

The purification of this mutant requires special attention, because if it was purified following the same procedure as that for the wild type mutant, a significant portion of the purified E126Q mutant has tightly bound substrate HMBPP, as indicated by the EPR spectrum. Passing through a desalting column or dialysis cannot remove these adventitiously bound HMBPP. I have therefore modified the purification protocol for this enzyme, adding an additional step after cell lysis to digest HMBPP in the cell lysate, by using wild type IspH enzyme. Specifically, wild type *A. aeolicus* IspH was added to the cell lysate, and sodium dithionite was added to 3 mM. The cell lysate was then incubated with stirring for another 2 hours, then the protein was purified using Strep-tag chromatography as described for the wild type enzyme. Because the added A. aeolicus IspH was His-tagged, it did not bind to the strep-tag column. E126Q mutant purified following this protocol was 80% - 90% ligand-free, as judged by EPR spectroscopy.

3.5.4 *A. aeolicus* IspH protein expression, purification and reconstitution

BL-21(DE3) cells producing either wild type IspH of IspH mutants from *A. aeolicus* were grown in LB media supplemented with 150 mg/L ampicillin at 37 °C until the OD_{600} reached 0.6. Cells were then induced with 200 μg / L anhydrotetracycline, and then grown at 20 °C for 15 hours. Cells were harvested by centrifugation (9000 rpm, 8 min, 4 °C) and were kept at -80 °C until use.

A. aeolicus IspH protein (either wild type or mutants) could be purified anaerobically following the same procedure as described above for *E. coli* IspH, however, the iron-sulfur

content in the as purified enzyme is low and still needs reconstitution. Therefore, *A. aeolicus* IspH protein used in this study was purified aerobically, followed by anaerobic reconstitution in a glove box with O_2 level lower than 2 ppm, as described below. Cell pellets were resuspended and lysed in B-PER (Thermo Scientific, Rockford, IL) protein extraction reagent for one hour at 4°C, then centrifuged at 200,000 rpm at 4 °C for 15 min. The supernatant was applied to a Ni-NTA column equilibrated with 5 mM imidazole in a pH 8.0 buffer containing 50 mM Tris·HCl and 150 mM NaCl. After washing with 20 mM imidazole, protein was eluted with 100 mM imidazole. Fractions were collected and dialyzed in pH 8.0 buffer containing 50 mM Tris·HCl, 150 mM NaCl, 5% glycerol, and 1mM DTT, 4 times. The purified protein was flash-frozen in liquid nitrogen and stored at -80 °C until use.

Before reconstitution, *A. aeolicus* IspH was transferred into a Coy Vinyl Anaerobic Chamber after being degassed on a Schlenk line. All the following steps were performed inside the anaerobic chamber with an oxygen level < 2 ppm. In a typical reconstitution experiment, 10 mM DTT and ~ 0.5 mg of elemental sulfur were added to 3 mL 0.6 mM protein solution in a pH 8.0 buffer containing 50 mM Tris·HCl, 150 mM NaCl and 5% glycerol. After stirring for 1.5 hours, $FeCl_3$ was then added slowly to 6 equivalents from a 30 mM stock solution. After 3 hours, an aliquot of the solution was centrifuged and a UV-VIS spectrum recorded. If the A_{410nm} / A_{280nm} ratio was ≥ 0.38, the protein was then desalted by passing through a PD10 column. If the ratio was < 0.38, more DTT, elemental sulfur and $FeCl_3$ were added and incubation (with stirring) continued for a longer time (typically ~ 2 hours) until the ratio was ~ 0.38. Alternatively, the protein can be reconstituted by adding 5 mM DTT, 8-10 equivalents of Na2S followed by slowly

adding 6~8 equivalents FeCl$_3$ with stirring. The reconstituted protein was then concentrated by ultrafiltration, and the protein concentration determined with a Bio-Rad (Hercules, CA) Protein Assay kit. For the [57]Fe enriched sample, [57]Fe metal was dissolved in HCl in air, then after pH adjustment, was purged with nitrogen gas and used for reconstitution as described above.

3.5.5 Enzyme inhibition assays

All assays were performed anaerobically at room temperature according to Altincicek et. al. [5], with minor modifications. To a pH 8.0 buffer solution containing 50 mM Tris−HCl, 150 mM NaCl, and 5% glycerol, sodium dithionite was added to 0.4 mM, methyl viologen was added to 2 mM, and IspH was added to 72 nM. For enzyme assays, various amounts HMBPP were added and the reactions were monitored at 732 nm. Initial velocities were fit by using the Michaelis-Menten equation with OriginPro 8 (OriginLab Corporation, Northampton, MA).

3.5.6 EPR and ENDOR spectroscopy

Samples for continuous-wave EPR spectroscopy were typically 0.1 - 0.3 mM in IspH enzyme, while samples for pulsed EPR spectroscopy were typically 1 - 2 mM. Ligands were added to 10 - 50 equivalents in the presence of 20 equivalents (for *A. aeolicus* IspH) or 50 equivalents (for *E. coli* IspH) of sodium dithionite. *A. aeolicus* IspH was also reduced photochemically in the presence of 300 μM 5-deazaflavin, 10 mM ammonium oxalate, and 5 mM DTT, using illumination from a 300 W LCD projector at ~1 cm for 2.5 hours. For *A. aeolicus* IspH samples, glycerol was added to 42.5 % (v/v) before frozen in liquid nitrogen. For *E. coli* IspH, glycerol was added to 15% - 20% before frozen in liquid nitrogen.

Continuous-wave EPR spectra were collected at X-band using a Varian E-122 spectrometer

together with an Air Product (Allentown, PA) helium cryostat. Data acquisition parameters were typically: field center = 3250 or 2500 G; field sweep = 800 or 4000 G; modulation = 100 kHz; modulation amplitude = 5 G; time constant = 32 ms; 60 sec per scan; 8 sec between each scan; and temperature = 15K. EPR spectra were simulated by using the "EasySpin" program [30].

Pulsed EPR (including electron-nuclear double resonance, or ENDOR, and hyperfine sublevel correlation, or HYSCORE) spectra were obtained on a Bruker ElexSys E-580-10 FT-EPR X-band EPR spectrometer using an ENI A 300RF or Bruker amplifier, and an Oxford Instruments CF935 cryostat. Davies pulsed ENDOR experiments were carried out using a three pulse scheme (π_{mw} −T− $\pi/2_{mw}$ − τ − π_{mw} − τ − echo, π_{rf} was applied during T),[31] while Mims pulsed ENDOR was employed using a three pulse scheme ($\pi/2_{mw}$ − τ − $\pi/2_{mw}$ − T − $\pi/2_{mw}$ − τ − echo, $\pi/2_{mw}$ = 16 ns and π_{rf} was applied during T). τ-averaging was used to reduce the blind spots that arise from the τ-dependent oscillations in Mims ENDOR experiments. HYSCORE used a four-pulse sequence ($\pi/2_{mw}$ − τ - $\pi/2_{mw}$ − t_1 − π_{mw} − t_2 − $\pi/2_{mw}$ − echo; $\pi/2_{mw}$ = 16 ns), 256 points for both t_1 and t_2, each at 20 ns steps. Time-domain data were baseline corrected using a 3rd order polynomial, then Hamming windowed, followed by zero-filling and 2D-Fourier transformation. The HYSCORE spectrum was simulated using EasySpin program package [30].

3.6 Figures and Table
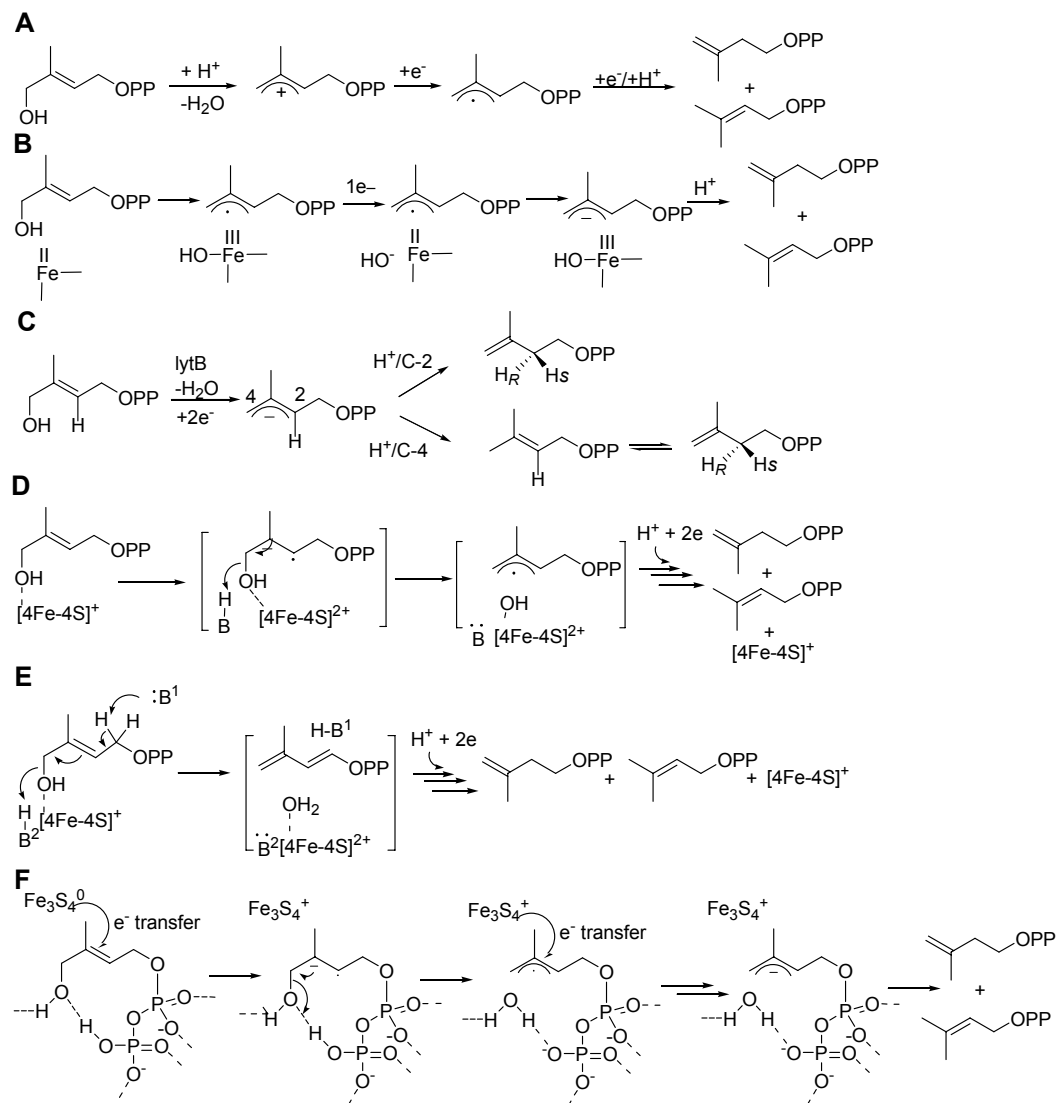
**Figure 3.1.** Previously proposed mechanisms of IspH catalysis.
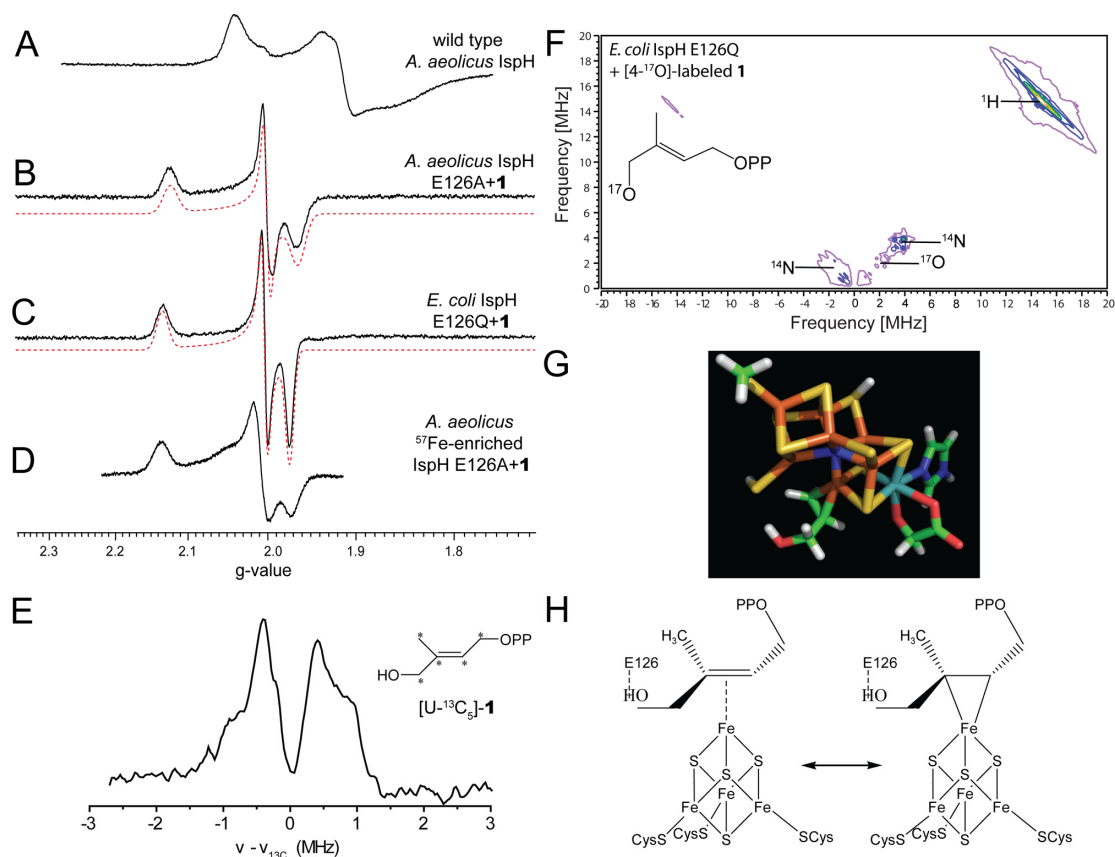
Figure 3.2. The reaction intermediate trapped with IspH E126A/E126Q mutant. (A), X-band EPR spectrum of wild type ligand-free *A. aeolicus* IspH. (B), X-band EPR spectrum of *A. aeolicus* IspH E126A mutant with **1**. (C), X-band EPR spectrum of *E. coli* IspH E126Q mutant with **1**. Red dotted lines are spectral simulations. (D), X-band EPR spectrum of [57]Fe-enriched *A. aeolicus* IspH E126A mutant with **1**. (E), X-band ^{13}C-Mims ENDOR spectrum of E126A+ [4-[17]O]-**1** at g_2. τ-averaging (32 spectra at 8 ns step, starting from 200 ns) was used. (F), X-band HYSCORE spectrum of *E. coli* IspH E126Q mutant with [4-[17]O]-**1** at g_2. (G), allyl alcohol binding to nitrogenase FeMo cofactor, forming a π-complex. (H), the formation of a π-complex between **1** and the [4Fe-4S][+] cluster of IspH. (A) - (F) were taken at $T = 15$ K.
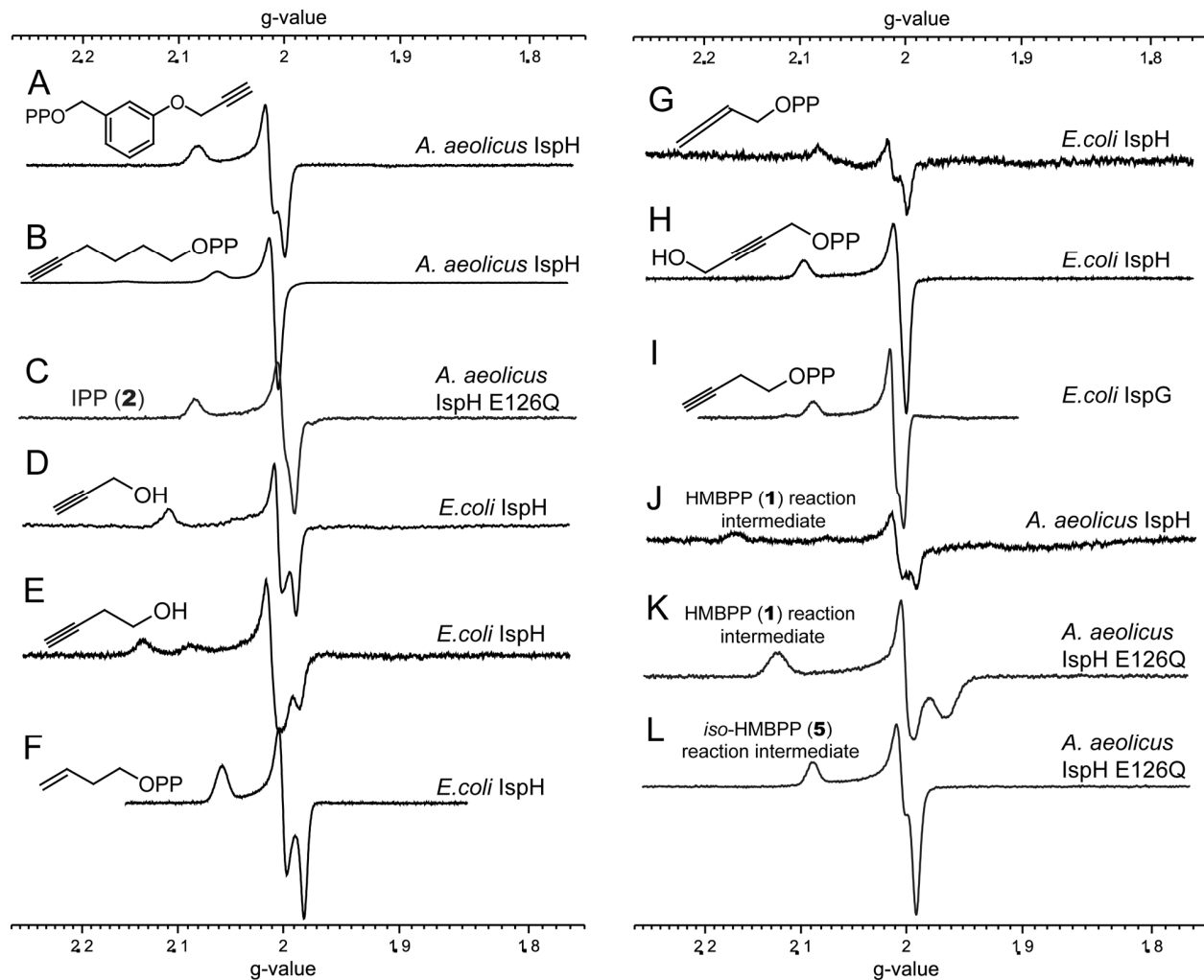
**Figure 3.3.** Previously unpublished X-band EPR spectra of IspH/IspG with alkene/alkyne ligands, and *A. aeolicus* IspH reaction intermediates.

70
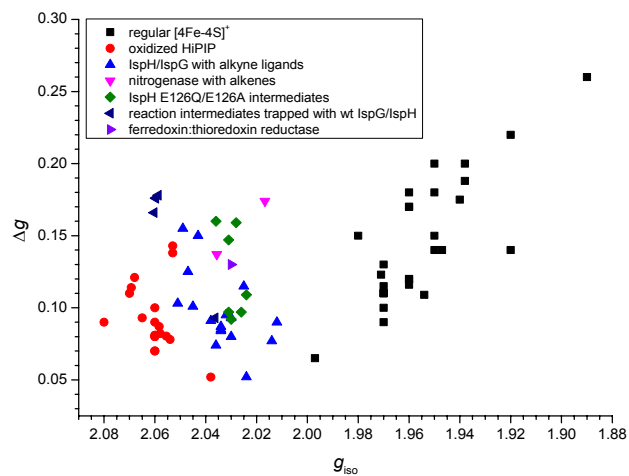
Figure 3.4. Plot of g_{iso} vs. Δg for 80 iron-sulfur containing systems.
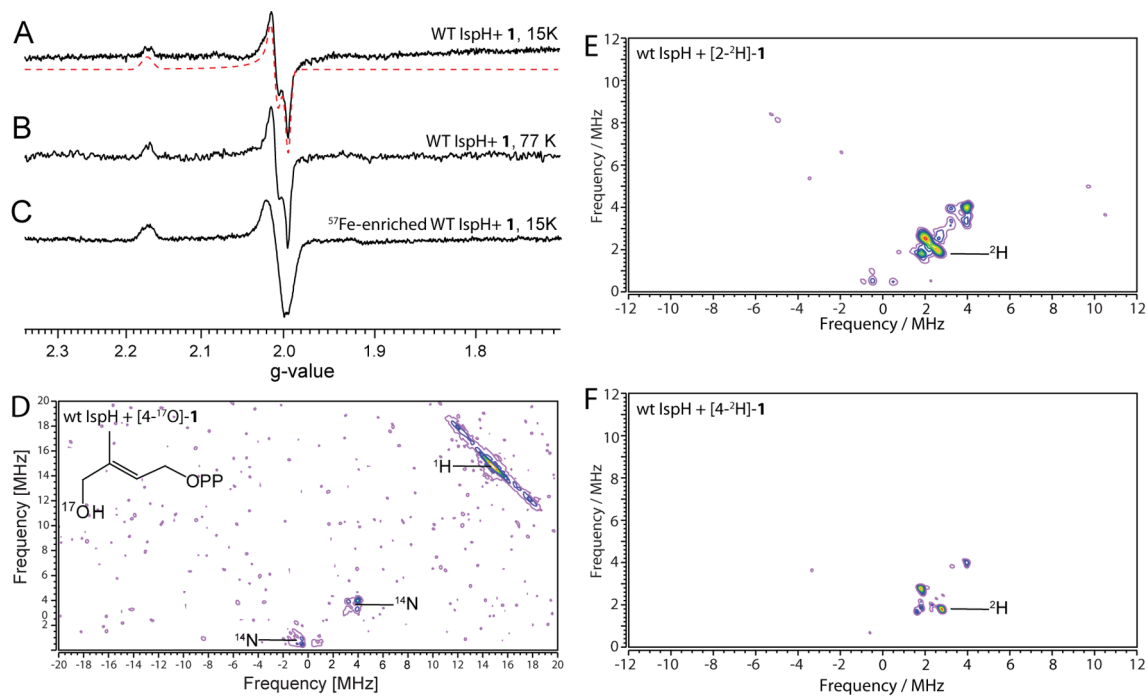
Figure 3.5. The reaction intermediate of **1** trapped with wild type IspH. (A), X-band EPR of IspH + **1** at 15 K. Spectral simulations are shown as red dotted lines. (B), X-band EPR of IspH + **1** at 77 K. (C), X-band EPR of [57]Fe-enriched IspH + **1** at 15 K. (D), X-band HSYCORE spectrum of IspH+[4-[17]O]-**1**. (D) is the sum of spectra taken at τ = 108 ns, 136 ns, and 208 ns. (E), IspH + [2-[2]H$_1$]-**1**. (F), IspH + [4-[2]H$_1$]-**1**. τ = 136 ns for (E) and (F).
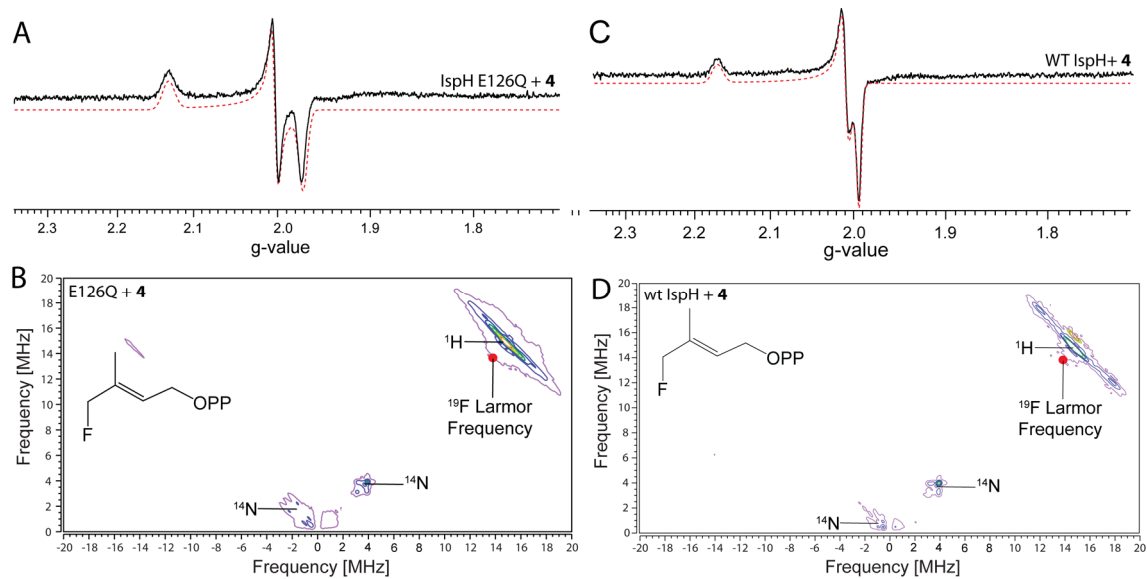
Figure 3.6. Non-natural substrate **4** binding to and reacting with *E. coli* IspH. (A), X-band EPR spectrum of *E. coli* IspH E126Q mutant + **4**. (B), X-band HYSCORE spectrum of *E. coli* IspH E126Q mutant + **4**. (C), X-band EPR spectrum of the reaction intermediate trapped with wild type *E. coli* IspH + **4**. (D), X-band HYSCORE spectrum of the reaction intermediate trapped with wild type *E. coli* IspH + **4**. (B) and (D) are sums of spectra taken at τ = 108 ns, 136 ns, and 208 ns. T = 15 K.
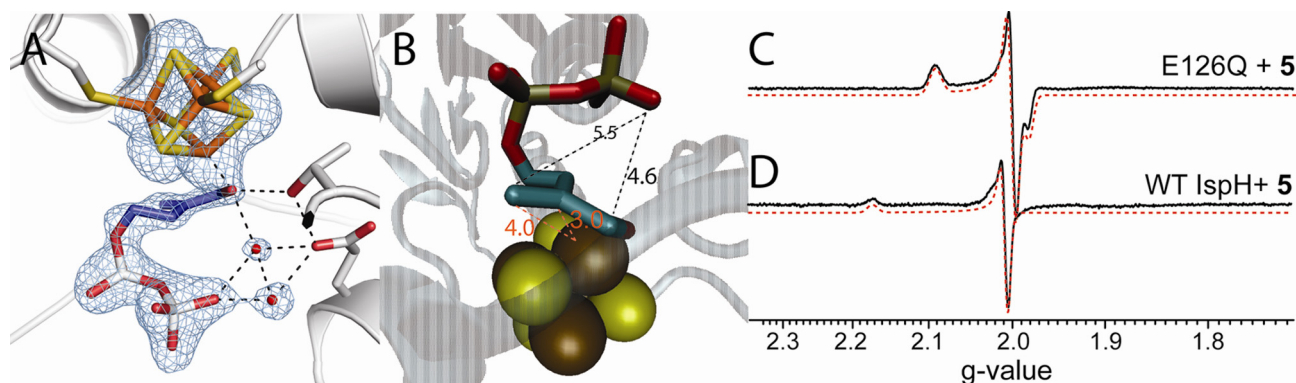
Figure 3.7. *Iso*-HMBPP (**5**) binding to and reacting with *E. coli* IspH. (A) and (B), X-ray structure of the

alkoxide complex formed by IspH + **5**. Electron densities in (A) represented in blue are contoured at 1.0σ with

$2F_0\text{-}F_c$ coefficients. C4-O, C5-O, Fe-C3 and Fe-C5 distances are labeled in Å in (B). (C) X-band EPR of IspH

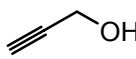E126Q mutant + **5**. (D) X-band EPR of wild type IspH + **5**. Spectral simulations are shown as red dotted lines
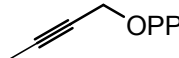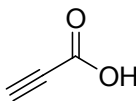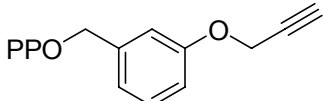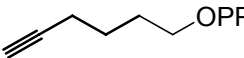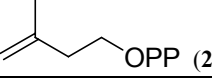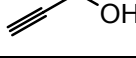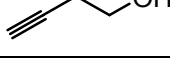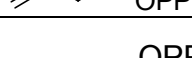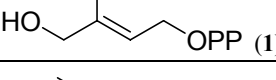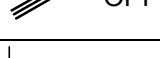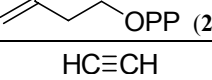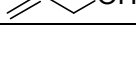
Table 3.1. *g*-values of various iron-sulfur clusters.

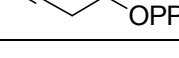|	Enzymes	comments	g_1	g_2	g_3	g_{iso}	Δg	references
$[Fe_4S_4]^+$ enzymes	*Aquifex aeolicus* IspH	ligand-free (major component)	2.040	1.916	1.865	1.940	0.175	20
		ligand-free (minor component)	2.040	1.935	1.840	1.938	0.200	
		with pyridine diphosphate inhibitor	2.041	1.921	1.853	1.938	0.188	32
	E. coli IspH	ligand-free (reconstituted)	2.037	1.921	1.921	1.960	0.116	2
	E. coli IspG	ligand-free	2.04	1.90	1.90	1.95	0.140	33
	E.coli fumarase	ligand-free, S=1/2 component	2.03	1.94	1.88	1.95	0.15	34
		with sodium fumarate	2.035	1.92	1.815	1.92	0.22	
	aconitase (from bovine heart)	ligand-free	2.06	1.93	1.86	1.95	0.2	35
		citrate bound	2.04	1.85	1.78	1.89	0.26	
	endonuclease III Fe-S center		2.04	1.94	1.94	1.97	0.1	36
	Pyruvate formate-lyase activating enzyme	ligand-free	2.02	1.94	1.88	1.947	0.14	37,38
		SAM bound	2.01	1.88	1.87	1.92	0.14	
	Benzoyl CoA reductase	cluster I	2.017	1.938	1.908	1.954	0.109	39
		cluster II	2.05	1.93	1.93	1.971	0.123	
		cluster III	2.03	1.995	1.965	1.997	0.065	
	DNA polymerase CysB motif		2.04	1.93	1.93	1.97	0.11	40
ferredoxins	*Bacillus polymyxa* ferredoxin		2.06	1.93	1.88	1.96	0.180	41
	Bacillus stearothermophilus ferredoxin		2.06	1.93	1.89	1.96	0.170	42
	Chromatium ferredoxin		2.04	1.93	1.93	1.97	0.110	43 44
	Clostridium pasterianum ferredoxin		2.06	1.92	1.88	1.95	0.180	45
	Desulfovibrio gigas ferredoxin		2.07	1.94	1.92	1.98	0.150	
	Rhodospirillum rubrum ferredoxin		2.03	1.94	1.94	1.97	0.090	46
	R. gelatinosa high potential iron-sulfur protein	super-reduced, $[4Fe-4S]^+$	2.04	1.92	1.92	1.96	0.120	47

Table 3.1. Continued.

	Enzymes	comments	g1	g2	g3	giso	Δg	references
synthetic [Fe$_4$S$_4$]$^+$	[Fe$_4$S$_4$(SCH$_2$Ph)$_4$]$^{3-}$		2.04	1.93	1.93	1.97	0.110	48
	[Fe$_4$S$_4$(SPh)$_4$]$^{3-}$ in solution		2.06	1.93	1.93	1.97	0.130	49
	[Fe$_4$S$_4$(SCH$_2$CH$_2$OH)$_4$]$^{3-}$		2.05	1.93	1.93	1.97	0.115	50
	[Fe$_4$S$_4$(S-p-C$_6$H$_4$Br)$_4$]$^{3-}$ polycrystalline		2.06	1.93	1.89	1.96	0.170	51,52
	[Fe$_4$S$_4$(S-p-C$_6$H$_4$Br)$_4$]$^{5-}$ in solution		2.04	1.92	1.92	1.96	0.120	52
oxidized high potential iron-sulfur proteins (HiPIP)	*R. gelatinosa* HiPIP		2.11	2.03	2.03	2.06	0.080	53
	Chromatium vinosum HiPIP	the major component	2.12	2.04	2.02	2.06	0.100	54
	Chromatium vinosum HiPIP	the minor component	2.13	2.07	2.04	2.08	0.090	
	Ectothiorhodospira halophila iso-II HiPIP	single component	2.145	2.034	2.024	2.068	0.121	55
	Rhodoferax fermentans HiPIP		2.114	2.033	2.033	2.060	0.081	56
	E. halophila HiPIP I	the major isomer	2.14	2.03	2.03	2.07	0.110	57
	E. halophila HiPIP I	the minor isomer	2.10	2.06	2.03	2.06	0.070	
	Rhodocyclus tenuis HiPIP		2.11	2.03	2.03	2.06	0.080	58
	Rhodophila globiformis HiPIP		2.12	2.03	2.03	2.06	0.090	47
	Thiobacillus ferrooxidans		2.127	2.034	2.034	2.065	0.093	59
	Halorhodospira halophila isoprotein I	major component (91%)	2.1435	2.0350	2.0295	2.0693	0.1140	60
	Ectothiorhodospira vacuolata isoprotein I	major component (70%)	2.1090	2.0287	2.0287	2.0555	0.0803	
	Ectothiorhodospira vacuolata isoprotein II	major component (70%)	2.112	2.038	2.025	2.0583	0.0870	
	Rubrivivax gelatinosus	major component (64%)	2.1127	2.0305	2.0305	2.0579	0.0822	
synthetic HiPIP models	(NBu$_4$)[Fe$_4$S$_4$(SR)$_4$]	in toluene	2.10	2.05	2.03	2.06	0.070	61
	[(C$_2$H$_5$)$_4$N]$_2$ [Fe$_4$S$_4$(SCH$_2$Ph)$_4$]	γ-irradiated single crystal	2.142	2.013	2.004	2.053	0.138	62
			2.146	2.009	2.003	2.053	0.143	
			2.101	2.039	2.023	2.054	0.078	
			2.070	2.026	2.018	2.038	0.052	

Table 3.1. Continued.

	Enzymes	comments	g1	g2	g3	giso	Δg	references
[4Fe-4S] enzymes With unsaturated ligands	*Aquifex aeolicus* IspH		2.125	2.015	2.000	2.047	0.125	20
			2.080	2.010	2.000	2.030	0.080	20
			2.112	2.011	2.011	2.045	0.101	63
			2.085	2.011	2.011	2.036	0.074	
			2.087	2.015	2.000	2.034	0.087	Fig. 3.3A
			2.059	2.007	2.007	2.024	0.052	Fig. 3.3B
	Aquifex aeolicus IspH E126Q mutant	(**2**)	2.088	2.006	1.995	2.030	0.093	Fig. 3.3C
	E. coli IspH		2.145	2.011	1.990	2.049	0.155	Fig. 3.3D
			2.135	2.008	1.985	2.043	0.150	Fig. 3.3E
			2.059	2.002	1.982	2.014	0.077	Fig. 3.3F
			2.085	2.015	2.001	2.034	0.084	Fig. 3.3G
			2.099	2.008	2.008	2.038	0.091	Fig. 3.3H
	E. coli IspG	(**1**)	2.090	2.010	1.975	2.025	0.115	64
			2.088	2.012	2.003	2.034	0.085	Fig. 3.3I
			2.090	2.012	1.995	2.032	0.095	64
	T. thermophilus IspH	(**2**)	2.065	1.995	1.975	2.012	0.090	64
	Benzoyl-CoA reductase	HC≡CH	2.120	2.017	2.017	2.051	0.103	39
	nitrogenase	$H_2C{=}CH_2$	2.123	1.978	1.949	2.017	0.174	65
			2.123	1.998	1.986	2.036	0.137	

Table 3.1. Continued.

	Enzymes	comments	g1	g2	g3	giso	Δg	references
IspH reaction intermediates trapped with the wild type enzyme	*Aquifex aeolicus* IspH	HMBPP (**1**), 30 sec intermediate	2.172	2.010	1.994	2.059	0.178	Fig. 3.3J
	E. coli IspH	HMBPP (**1**), 30 sec intermediate	2.172	2.011	1.996	2.060	0.176	Fig. 3.5A
		iso-HMBPP (**5**), 30 sec intermediate	2.171	2.005	2.005	2.060	0.166	Fig. 3.7D
		FMBPP (**4**), 30 sec intermediate	2.172	2.011	1.996	2.060	0.176	Fig. 3.6C
IspH reaction intermediates trapped with E126A/E126Q mutants	*Aquifex aeolicus* IspH E126A mutant	HMBPP (**1**, unreactive)	2.122	1.997	1.975	2.031	0.147	20
	Aquifex aeolicus IspH E126Q mutant	HMBPP (**1**, unreactive)	2.122	1.999	1.963	2.028	0.159	Fig. 3.3K
		iso-HMBPP (**5**, unreactive), comp. I	2.091	2.007	1.994	2.031	0.097	Fig. 3.3L
		iso-HMBPP (**5**, unreactive), comp. II	2.091	1.994	1.994	2.026	0.097	
	E. coli IspH E126Q mutant	HMBPP (**1**, unreactive)	2.132	2.003	1.972	2.036	0.160	Fig. 3.2C
		FMBPP (**4**, unreactive)	2.132	2.003	1.972	2.036	0.160	Fig. 3.6A
		iso-HMBPP (**5**, unreactive), comp. I	2.091	1.999	1.999	2.030	0.092	Fig. 3.7C
		iso-HMBPP (**5**, unreactive), comp. II	2.091	1.999	1.982	2.024	0.109	
IspG reaction intermediate	*E. coli* IspG	reaction intermediate "X"	2.092	2.018	1.999	2.036	0.093	64
	T. thermophilus IspG	reaction intermediate "X"	2.087	2.019	2.000	2.035	0.087	22
Ferredoxin: Thioredoxin Reductase	FTR from spinach	reaction intermediate	2.11	2.00	1.98	2.03	0.13	25
		NEM-modified	2.11	2.00	1.98	2.03	0.13	24
		super oxidized	2.090	2.040	2.020	2.05	0.07	

3.7 References

(1) Rohmer, M. *Lipids* **2008**, *43*, 1095.

(2) Wolff, M.; Seemann, M.; Tse Sum Bui, B.; Frapart, Y.; Tritsch, D.; Garcia Estrabot, A.; Rodriguez-Concepcion, M.; Boronat, A.; Marquet, A.; Rohmer, M. *FEBS Lett* **2003**, *541*, 115.

(3) Xiao, Y.; Chu, L.; Sanakis, Y.; Liu, P. *J Am Chem Soc* **2009**, *131*, 9931.

(4) Seemann, M.; Janthawornpong, K.; Schweizer, J.; Bottger, L. H.; Janoschka, A.; Ahrens-Botzong, A.; Tambou, E. N.; Rotthaus, O.; Trautwein, A. X.; Rohmer, M.; Schunemann, V. *J Am Chem Soc* **2009**, *131*, 13184.

(5) Altincicek, B.; Duin, E. C.; Reichenberg, A.; Hedderich, R.; Kollas, A. K.; Hintz, M.; Wagner, S.; Wiesner, J.; Beck, E.; Jomaa, H. *FEBS Lett* **2002**, *532*, 437.

(6) Grawert, T.; Rohdich, F.; Span, I.; Bacher, A.; Eisenreich, W.; Eppinger, J.; Groll, M. *Angew Chem Int ed* **2009**, *48*, 5756.

(7) Rohdich, F.; Zepeck, F.; Adam, P.; Hecht, S.; Kaiser, J.; Laupitz, R.; Grawert, T.; Amslinger, S.; Eisenreich, W.; Bacher, A.; Arigoni, D. *Proc Natl Acad Sci U S A* **2003**, *100*, 1586.

(8) Xiao, Y.; Zhao, Z. K.; Liu, P. *J Am Chem Soc* **2008**, *130*, 2164.

(9) Xiao, Y.; Liu, P. *Angew Chem Int ed* **2008**, *47*, 9722.

(10) Rekittke, I.; Wiesner, J.; Rohrich, R.; Demmer, U.; Warkentin, E.; Xu, W.; Troschke, K.; Hintz, M.; No, J. H.; Duin, E. C.; Oldfield, E.; Jomaa, H.; Ermler, U. *J Am Chem Soc* **2008**, *130*, 17206.

(11) Grawert, T.; Span, I.; Eisenreich, W.; Rohdich, F.; Eppinger, J.; Bacher, A.; Groll, M. *Proc Natl Acad Sci USA* **2010**, *107*, 1077.

(12) Grawert, T.; Span, I.; Bacher, A.; Groll, M. *Angew Chem Int ed* **2010**, *49*, 8802.

(13) Span, I.; Grawert, T.; Bacher, A.; Eisenreich, W.; Groll, M. *J Mol Biol* **2011**, *416*, 1.

(14) Werst, M. M.; Kennedy, M. C.; Beinert, H.; Hoffman, B. M. *Biochemistry* **1990**, *29*, 10526.

(15) Kennedy, M. C.; Werst, M.; Telser, J.; Emptage, M. H.; Beinert, H.; Hoffman, B. M. *Proc Natl Acad Sci USA* **1987**, *84*, 8854.

(16) Citron, C. A.; Brock, N. L.; Rabe, P.; Dickschat, J. S. *Angew Chem Int ed* **2012**, DOI: 10.1002/anie.201201110.

(17) Lee, H. I.; Sorlie, M.; Christiansen, J.; Yang, T. C.; Shao, J.; Dean, D. R.; Hales, B. J.; Hoffman, B. M. *J Am Chem Soc* **2005**, *127*, 15880.

(18) Lee, H. I.; Igarashi, R. Y.; Laryukhin, M.; Doan, P. E.; Dos Santos, P. C.; Dean, D. R.; Seefeldt, L. C.; Hoffman, B. M. *Journal of the American Chemical Society* **2004**, *126*, 9563.

(19) Pelmenschikov, V.; Case, D. A.; Noodleman, L. *Inorganic chemistry* **2008**, *47*, 6162.

(20) Wang, W.; Wang, K.; Liu, Y.-L.; No, J. H.; Nilges, M. J.; Oldfield, E. *Proc Natl Acad Sci USA* **2010**, *107*, 4522.

(21) Belinskii, M. *Chemical Physics* **1993**, *172*, 189.

(22) Adedeji, D.; Hernandez, H.; Wiesner, J.; Kohler, U.; Jomaa, H.; Duin, E. C. *FEBS Lett* **2007**, *581*, 279.

(23) Xu, W.; Lees, N. S.; Adedeji, D.; Wiesner, J.; Jomaa, H.; Hoffman, B. M.; Duin, E. C. *J Am Chem Soc* **2010**, *132*, 14509.

(24) Staples, C. R.; Ameyibor, E.; Fu, W.; Gardet-Salvi, L.; Stritt-Etter, A. L.; Schurmann, P.; Knaff, D. B.; Johnson, M. K. *Biochemistry* **1996**, *35*, 11425.

(25) Staples, C. R.; Gaymard, E.; Stritt-Etter, A. L.; Telser, J.; Hoffman, B. M.; Schurmann, P.; Knaff, D. B.; Johnson, M. K. *Biochemistry* **1998**, *37*, 4612.

(26) Walters, E. M.; Garcia-Serres, R.; Jameson, G. N.; Glauser, D. A.; Bourquin, F.; Manieri, W.; Schurmann, P.; Johnson, M. K.; Huynh, B. H. *J Am Chem Soc* **2005**, *127*, 9612.

(27) Mcmanus, H. J.; Fessenden, R. W.; Chipman, D. M. *J Phys Chem* **1988**, *92*, 3778.

(28) Xiao, Y.; Chang, W. C.; Liu, H. W.; Liu, P. *Org Lett* **2011**, *13*, 5912.

(29) Chang, W. C.; Xiao, Y.; Liu, H. W.; Liu, P. *Angew Chem Int ed* **2011**, *50*, 12304.

(30) Stoll, S.; Schweiger, A. *J Magn Reson* **2006**, *178*, 42.

(31) Gemperle, C.; Schweiger, A. *Chem Rev* **1991**, *91*, 1481.

(32) Wang, W.; Li, J.; Wang, K.; Smirnova, T. I.; Oldfield, E. *J Am Chem Soc* **2011**, *133*, 6525.

(33) Xiao, Y.; Zahariou, G.; Sanakis, Y.; Liu, P. *Biochemistry* **2009**, *48*, 10483.

(34) Flint, D. H.; Emptage, M. H.; Guest, J. R. *Biochemistry* **1992**, *31*, 10331.

(35) Beinert, H.; Kennedy, M. C.; Stout, C. D. *Chem Rev* **1996**, *96*, 2335.

(36) Cunningham, R. P.; Asahara, H.; Bank, J. F.; Scholes, C. P.; Salerno, J. C.; Surerus, K.; Munck, E.; McCracken, J.; Peisach, J.; Emptage, M. H. *Biochemistry* **1989**, *28*, 4450.

(37) Walsby, C. J.; Hong, W.; Broderick, W. E.; Cheek, J.; Ortillo, D.; Broderick, J. B.; Hoffman, B. M. *J Am Chem Soc* **2002**, *124*, 3143.

(38) Walsby, C. J.; Ortillo, D.; Yang, J.; Nnyepi, M. R.; Broderick, W. E.; Hoffman, B. M.; Broderick, J. B. *Inorg Chem* **2005**, *44*, 727.

(39) Boll, M.; Fuchs, G.; Meier, C.; Trautwein, A.; Lowe, D. J. *J Biol Chem* **2000**, *275*, 31857.

(40) Netz, D. J.; Stith, C. M.; Stumpfig, M.; Kopf, G.; Vogel, D.; Genau, H. M.; Stodola, J. L.; Lill, R.; Burgers, P. M.; Pierik, A. J. *Nat Chem Biol*, *8*, 125.

(41) Stombaugh, N.; Burris, R.; Ormejohn, W. *J Biol Chem* **1973**, *248*, 7951.

(42) Middleton, P.; Dickson, D. P.; Johnson, C. E.; Rush, J. D. *European journal of biochemistry / FEBS* **1978**, *88*, 135.

(43) Cammack, R. *Biochemical and biophysical research communications* **1973**, *54*, 548.

(44) Cammack, R. *Biochem Soc Trans* **1975**, *3*, 482.

(45) Cammack, R.; Rao, K. K.; Hall, D. O.; Moura, J. J.; Xavier, A. V.; Bruschi, M.; Le Gall, J.; Deville, A.; Gayda, J. P. *Biochim Biophys Acta* **1977**, *490*, 311.

(46) Yoch, D. C.; Carithers, R. P.; Arnon, D. I. *J Biol Chem* **1977**, *252*, 7453.

(47) Heering, H. A.; Bulsink, Y. B.; Hagen, W. R.; Meyer, T. E. *Eur J Biochem* **1995**, *232*, 811.

(48) Laskowski, E. J.; Frankel, R. B.; Gillum, W. O.; Papaefthymiou, G. C.; Renaud, J.; Ibers, J. A.; Holm, R. H. *J Am Chem Soc* **1978**, *100*, 5322.

(49) Laskowski, E. J.; Reynolds, J. G.; Frankel, R. B.; Foner, S.; Papaefthymiou, G. C.; Holm, R. H. *J Am Chem Soc* **1979**, *101*, 6562.

(50) Christou, G.; Garner, C. D.; Drew, M. G. B.; Cammack, R. *J Chem Soc Dalton Trans* **1981**, 1550.

(51) Papaefthymiou, G. C.; Laskowski, E. J.; Frotapessoa, S.; Frankel, R. B.; Holm, R. H. *Inorg Chem* **1982**, *21*, 1723.

(52) Carney, M. J.; Holm, R. H.; Papaefthymiou, G. C.; Frankel, R. B. *J Am Chem Soc* **1986**, *108*,

3519.

(53) Beinert, H.; Thomson, A. J. *Arch Biochem Biophys* **1983**, *222*, 333.

(54) Dunham, W. R.; Hagen, W. R.; Fee, J. A.; Sands, R. H.; Dunbar, J. B.; Humblet, C. *Biochim Biophys Acta* **1991**, *1079*, 253.

(55) Kappl, R.; Ciurli, S.; Luchinat, C.; Huttermann, J. *J Am Chem Soc* **1999**, *121*, 1925.

(56) Hochkoeppler, A.; Kofod, P.; Ferro, G.; Ciurli, S. *Arch Biochem Biophys* **1995**, *322*, 313.

(57) Dilg, A. W. E.; Mincione, G.; Achterhold, K.; Iakovleva, O.; Mentler, M.; Luchinat, C.; Bertini, I.; Parak, F. G. *J Biol Inorg Chem* **1999**, *4*, 727.

(58) Caspersen, M. B.; Bennett, K.; Christensen, H. E. M. *Protein Express Purif* **2000**, *19*, 259.

(59) Cavazza, C.; Guigliarelli, B.; Bertrand, P.; Bruschi, M. *Fems Microbiology Letters* **1995**, *130*, 193.

(60) Priem, A. H.; Klaassen, A. A.; Reijerse, E. J.; Meyer, T. E.; Luchinat, C.; Capozzi, F.; Dunham, W. R.; Hagen, W. R. *J Biol Inorg Chem* **2005**, *10*, 417.

(61) Papaefthymiou, V.; Millar, M. M.; Munck, E. *Inorg Chem* **1986**, *25*, 3010.

(62) Gloux, J.; Gloux, P.; Lamotte, B.; Mouesca, J. M.; Rius, G. *J Am Chem Soc* **1994**, *116*, 1953.

(63) Wang, K.; Wang, W.; No, J. H.; Zhang, Y.; Zhang, Y.; Oldfield, E. *J Am Chem Soc* **2010**, *132*, 6719.

(64) Wang, W.; Li, J.; Wang, K.; Huang, C.; Zhang, Y.; Oldfield, E. *Proc Natl Acad Sci USA* **2010**, *107*, 11189.

(65) Lee, H. I.; Igarashi, R. Y.; Laryukhin, M.; Doan, P. E.; Dos Santos, P. C.; Dean, D. R.; Seefeldt, L. C.; Hoffman, B. M. *J. Amer. Chem. Soc.* **2004**, *126*, 9563.

Chapter 4

IspH and IspG Inhibitor Discovery by Rationale Design:
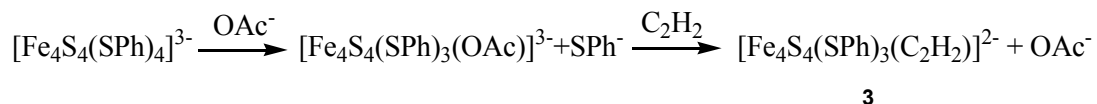
Alkyne Diphosphates

4.1 Notes and Acknowledgement

4.2 Introduction

The ultimate goal of this research is to design and discover inhibitors/drug leads targeting IspG and IspH. To get better ideas regarding inhibitor design, I first studied the catalytic mechanisms of IspG and IspH, described In Chapter 2 and Chapter 3. Key reaction intermediates in IspG and IspH catalyses have been characterized, and structures of these intermediates have been proposed. In IspG catalysis, a ferraoxetane intermediate is formed during the reaction, while in IspH catalysis, weak π-interaction between the alkene substrate HMBPP (**1**) and the unique 4th iron of the [4Fe-4S] cluster is critical (Scheme 4.1). Can we design any IspG/IspH inhibitors based on knowledge on catalytic mechanisms?

The inspiration came from the IspH catalytic mechanism. Since the [4Fe-4S] cluster of IspH can form weak π-complex (**2**) with its alkene substrate (**1**), what about alkynes? There are in fact precedents for the formation of organometallic species (i.e. containing Fe-C bonds) between [4Fe-4S] clusters and alkynes, which would be expected to act as IspH/IspG inhibitors. For example, in an early literature, McMillan *et al.* investigated the reduction of acetylene (C_2H_2) to ethylene (C_2H_4) by reduced synthetic [4Fe-4S] clusters, in particular $[Fe_4S_4(SPh)_4]^{3-}$.[1] These workers proposed that an acetato complex reacted initially with C_2H_2 to form an organometallic species, **3**:

$$[Fe_4S_4(SPh)_4]^{3-} \xrightarrow{OAc^-} [Fe_4S_4(SPh)_3(OAc)]^{3-} + SPh^- \xrightarrow{C_2H_2} [Fe_4S_4(SPh)_3(C_2H_2)]^{2-} + OAc^-$$

3

most likely containing a side-on (π/σ) acetylene unit, which was then *cis*-reduced to ethylene. Basically the same reduction, of diphenylacetylene (**4**) to *cis*-stilbene (**5**), was reported by Itoh.[2]

In these systems, alkyne complexes were not observed directly, but under controlled potential (electrochemical reduction) conditions, Tanaka *et al.* found evidence for a π complex of acetylene bound to $[Fe_4S_4(SPh)_4]^{3-}$ and $[Mo_2Fe_6S_8(SPh)_9]^{3-}$ clusters, as evidenced by significant shifts in the C≡C vibrational Raman spectra.[3] These workers also demonstrated that acetylene bound most strongly to reduced $([4Fe-4S]^+)$ clusters, and resulted in release of one SPh⁻.
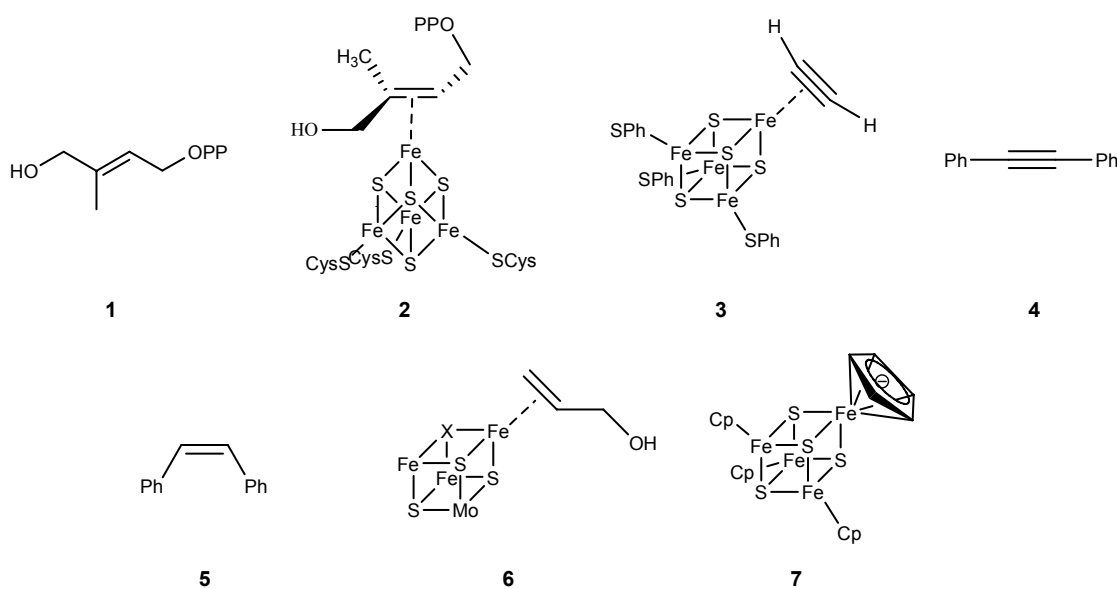

Scheme 4.1. Some of the stuctures discussed in this chapter.

This formation of a π complex would be very similar to that deduced for the binding of the HMBPP parent molecule, allyl alcohol (which lacks the Me and CH₂OPP substituents) to the FeMo cofactor in nitrogenase,[4] illustrated in Scheme 4.1 as the Fe₃MoS₃X cubane-like fragment (**6**). It also seemed possible that aromatic residues might interact with the [4Fe-4S] cluster, just as the cyclopentadienide ion did in model Fe₄S₄ clusters,[5] such as **7**. Although the structures of complexes such as **3** have not been confirmed crystallographically, the structure proposed by

McMillan et al.[1] is likely to involve the same type of bonding as found in many other organometallic complexes,[6] being described as a resonance hybrid of a pure π complex and a σ complex,[4] the latter corresponding to a metallacycle.

These results suggested to us that acetylenes might likewise bind to reduced IspH, forming π-complexes. Interestingly, with low valent (Fe^I) complexes, alkynes have also been found to bind far more strongly than do alkenes,[7] leading again to the possibility that alkynes could bind to iron and be good IspH/IspG inhibitors, displacing the olefinic substrate HMBPP. We thus investigated the binding and inhibition of IspH and IspG by propargyl alcohol (**8**) and a series of alkyne diphosphate compounds and (**9 - 13**) as well as their isoelectronic analogs (**14** and **15**), shown in Scheme 4.2.
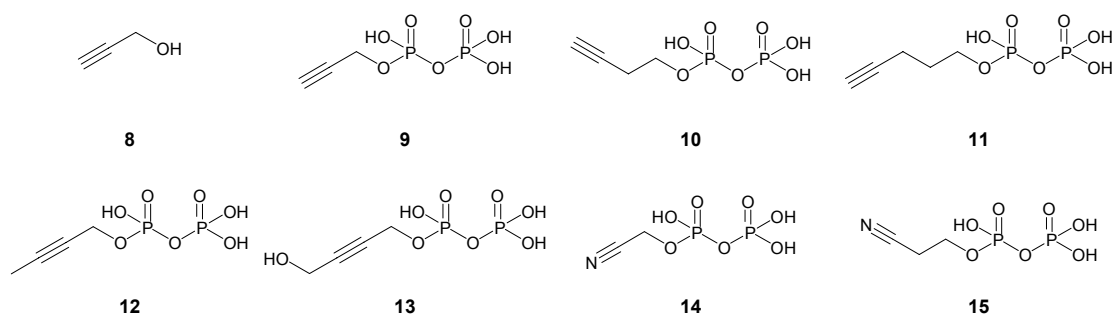
Scheme 4.2. Inhibitors studied in this chapter.

4.3 Results and Discussion

4.3.1 Propargyl alcohol binds to reduced IspH

As expected, propargyl alcohol (**8**) does bind to reduced IspH, as evidenced by EPR spectroscopic data. The EPR spectra of ligand-free IspH and IspH with **8** are shown in Figure

4.1A and B, which indicate large g-value changes upon adding **8**, suggesting a direct interaction with the [4Fe-4S]$^+$ cluster. Additional evidence for direct binding of **8** to the [4Fe-4S]$^+$ cluster of IspH comes from ^{1}H/^{2}H and ^{13}C ENDOR data. The Davies ENDOR spectrum (Figure 4.1C) of IspH with **8** shows an A (^{1}H) ~ 10 MHz hyperfine coupling feature, while in the Davies ENDOR spectrum of IspH with [3-^{2}H$_1$]-**8**, the ~10 MHz proton feature is greatly attenuated (Figure 4.1C, inset) and is replaced at low frequency by a ~1.5 MHz hyperfine coupling feature in the ^{2}H Mims ENDOR spectrum (Figure 4.1D), attributable to the 3-^{2}H. Orientation-selective ^{13}C Davies ENDOR experiment with selective inversion pulse (π_{mw} = 296 ns) using [U-^{13}C$_3$]-**8** revealed two ^{13}C peaks with fairly large hyperfine coupling constants (Figure 4.1E), one could be simulated with A (^{13}C) = [6.1 5.7 5.0] MHz, a_{iso} (^{13}C) = 5.6 MHz, and the other A (^{13}C) = [3.3 2.8 4.3] MHz, a_{iso} (^{13}C) = 3.5 MHz. Notably, the ^{13}C hyperfine couplings in the alkyne **8** are much larger than those found in the alkene complexes (~1–3.7 MHz),[8,9] suggesting stronger interactions between the metal clusters and the alkyne. This could be due to the fact that alkynes are better donors/acceptors than are alkenes. Overall, the ^{1}H and ^{2}H hyperfine couplings are similar to those seen in the nitrogenase + allyl alcohol system,[10] and the ^{13}C hyperfine coupling are even stronger, indicating formation of a π-complex.

4.3.2 Alkyne diphosphates are potent IspH/IspG inhibitors

Although propargyl alcohol (**8**) binds directly to [4Fe-4S]$^+$, it has very poor inhibitory activity against IspH (IC$_{50}$ > 10 mM). We reasoned that acetylenic diphosphates might interact more strongly with IspH, since there would be an increase in binding affinity due to their diphosphate moieties docking into the diphosphate binding site of IspH seen

crystallographically.[11] We thus synthesized propargyl diphosphate (**9**), and found it is a very potent IspH inhibitor with an IC_{50} of 6.7 μM. The binding mode of the alkyne moiety of **9** to IspH should be very similar to that of propargyl alcohol **8**. Like **8**, **9** changes the EPR spectrum of IspH (Figure 4.2A), and $A \sim 6$ MHz ^{13}C signal was observed when [U-$^{13}C_3$]-**9** was used (Figure 4.2D). Only very small ^{31}P hyperfine coupling constant was observed (~ 0.3 MHz, Figure 4.2E), indicating the diphosphate group does not bind directly to the [4Fe-4S]$^+$ cluster.

We then prepared several analogues of **9**. We first sought to improve activity by varying the length of the CH_2 spacer between the alkyne moiety and the diphosphate moiety. With the addition of 1 CH_2 group, **10** shows similar EPR spectrum (Figure 4.2B) as **9** when binding to IspH, and had the best inhibition activity ($IC_{50} = 0.45$ μM; $K_i \sim 60$ nM). With the addition of two CH_2 groups, **11** had about the same inhibition activity as **9**, with an $IC_{50} = 6.5$ μM. We then substituted the alkyne terminal hydrogen by a hydroxylmethyl group (**13**), the inhibition activity drops ($IC_{50} = 26$ μM). We also tested the effects of the isoelectronic analogs (**14**, **15**) of the acetylenes (-C≡C-H → -C≡N), cyanides, on IspH inhibition, but both compounds were far less active than their acetylenic counterparts ($IC_{50} = 254$ μM for **14** and 53 μM for **15**).

4.3.3 The binding mode is side-on

How do alkynes bind to the [4Fe-4S] cluster? Do they bind side-on as expected? I favor a side-on π-complex binding mode since: i) diphenylacetylene (**4**), which lacks a terminal H, binds to [4Fe-4S]$^+$ clusters[12] but as with acetylene,[1] is still *cis*-reduced (by ^{2}H);[12] ii) the shift in the C≡C vibrational Raman spectrum[3] of C_2H_2 on binding to [4Fe-4S]$^+$ clusters is relatively small (~ 60 cm^{-1}), while shifts seen on acetylide formation (or in mononuclear complexes) are typically

2-3 times larger;[13] iii), compound **12,** which cannot bind end-on to IspH, still exhibits (Figure 4.2C) a rhombic EPR spectrum similar to that seen with the terminal alkynes (Figures 4.2A, B); and iv), the observation of the ^{1}H/^{2}H ENDOR signal from the terminal ^{1}H/^{2}H in **8** or [3-^{2}H$_1$]-**8** (Figures 4.1C, D) indicate this terminal ^{1}H/^{2}H is still present when **8** binds to [4Fe-4S]$^+$, consistent with the side-on binding mode.

4.3.4 Alkyne diphosphates are also potent IspG inhibitors

Similar to IspH, IspG has a [4Fe-4S] cluster with a unique 4th iron not bonded to cysteine residue. In addition, the substrate of IspG contains a diphosphate group (Chapter 2), therefore, like IspH, it has a diphosphate group binding site, which is located on its TIM barrel domain[14,15] Based on these similarities with IspH, we reason that the alkyne group should also be able to bind at the unique 4th iron of IspG, and alkyne diphosphates should be potent IspG inhibitors. This is indeed the case. The EPR spectrum of propargyl diphosphate **9** bound to *E. coli* GcpE exhibited a spectrum (Figure 4.3A) similar to that observed with *A. aeolicus* IspH. A similar result was obtained with *T. thermophilus* IspG (Figure 4.3B). The results of an ENDOR experiment using [U-^{13}C$_3$]-**9** (Figure 4.3C) indicates a large ($A \sim$ 7 MHz) ^{13}C hyperfine interaction, together with a small ($A \sim$ 0.8 MHz) ^{31}P ENDOR signal. These results are very similar as those obtained with IspH + **9**, indicating formation of π-complex between the alkyne moiety of **9** and the unique 4th iron of IspG (Figure 4.3D), while the diphosphate group being away from the [4Fe-4S]$^+$ cluster. Finally, I find that **9** is a competitive IspG inhibitor with an IC$_{50}$ $\sim$ 750 nM ($K_i \sim$ 330 nM, Figure 4.3D), and is $\sim$1000 times more potent than previously reported IspG inhibitors.[16]

4.4 Conclusions

The formation of a π-complex in IspH catalysis has led to the discovery of alkyne diphosphates as the first μM inhibitors against IspH as well as IspG. Based on EPR and ENDOR studies, I propose that these types of inhibitors bind into the IspH active site with their diphosphates occupying the "PPi" site, while their alkyne groups form weak π-complexes with the unique 4th iron. In fact, there is good literature precedent for alkynes binding to model $[4Fe-4S]^+$ clusters, including Raman and catalytic activity results with model systems. These results have been interpreted as indicating π/σ "metallacycle" formation between $[4Fe-4S]^+$ clusters and alkynes. The observation that the IC_{50} for the most potent IspH alkyne inhibitor (IC_{50} = 0.45 μM; K_i ~ 60 nM) is much smaller than the K_M for HMBPP binding (K_M = 5 μM) is also expected based on organometallic precedent, in which alkynes bind much more strongly to low valent iron complexes than do alkenes.[7]

4.5 Materials and Methods

4.5.1 General aspects

E. coli and *A. aeolicus* IspH protein production and EPR spectroscopy were described in Chapter 3. The syntheses of alkyne/cyanide diphosphates **9-16** were performed by Ke Wang and were reported elsewhere.[17]

4.5.2 Enzyme inhibition assays

All assays were performed anaerobically at room temperature according to Altincicek et.

al.[18] with minor modification. To a pH 8.0 buffer solution containing 50 mM Tris·HCl, 150 mM

NaCl, and 5% glycerol, sodium dithionite was added to 0.4 mM, methyl viologen was added to 2

mM, and IspH was added to 72 nM. For enzyme assays, various amounts HMBPP were added

and the reactions were monitored at 732 nm. The initial velocities were fitted by using the

Michaelis-Menten equation with OriginPro 8 (OriginLab Corporation, Northampton, MA)

software. The activity of reconstituted *A. aeolicus* IspH tested under the conditions described

above was 1.2 μmol min^{-1} mg–1 with a K_M=7 μM. For inhibition assays, various concentrations

of inhibitor were added and incubated for 10 min, prior to addition of 34 μM HMBPP. Initial

velocities at different inhibitor concentrations were then plotted as dose-response curves, and

were fitted to the following equation, from which IC_{50} values were determined:
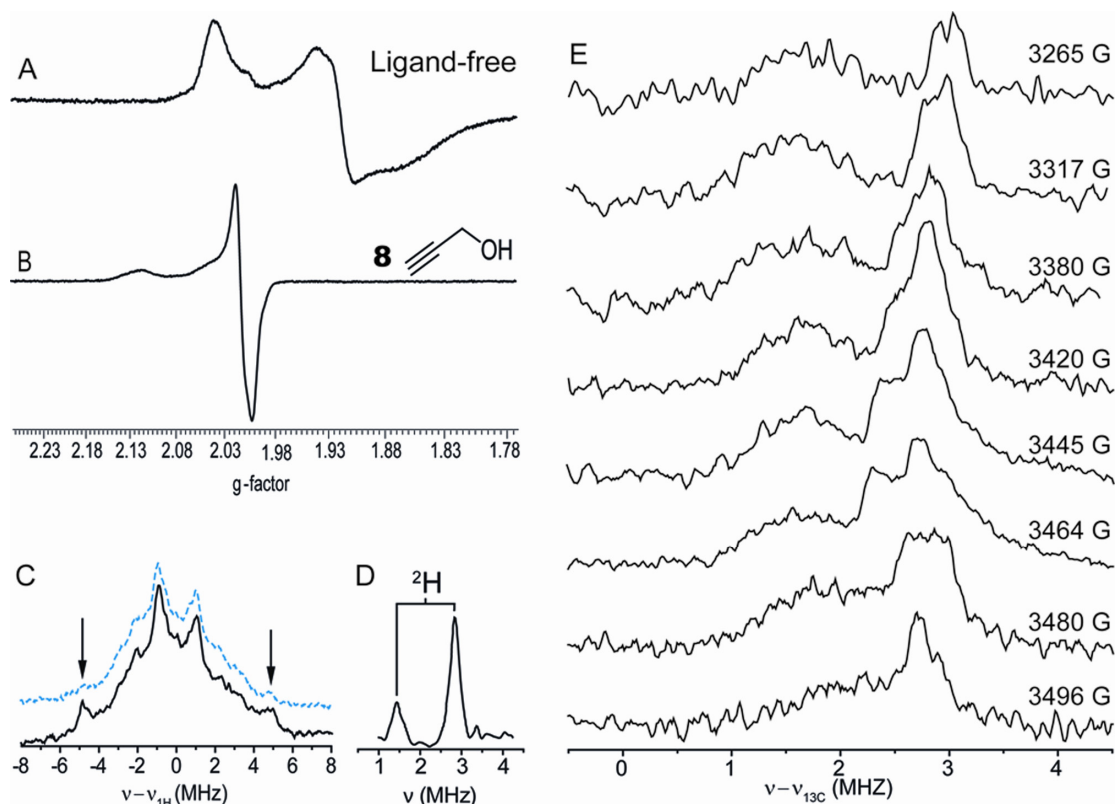
$$y = \frac{1}{1+\left(\dfrac{x}{IC_{50}}\right)^{slope}}$$

where x is the inhibitor concentration and y is the fraction inhibition. K_i values were then

deduced from the IC_{50} value by using the Cheng-Prusoff equation:[19]

$$K_i = \frac{IC_{50}}{1+\dfrac{[S]}{K_M}}$$

where [S] is the HMBPP concentration, and K_M is the Michaelis constant.

4.6 Figures

Figure 4.1. X-band EPR/ENDOR spectra of propargyl alcohol (**8**) binding to IspH. (A), EPR spectrum of ligand-free *A. aeolicus* IspH. (B), EPR spectrum of *A. aeolicus* IspH with **8**. (C), Davies ENDOR spectrum of *A. aeolicus* IspH with **8** at maximum EPR intensity, showing a large ^{1}H hyperfine coupling that is attenuated (inset, blue) in an 80% [3-^{2}H$_1$]-**8** labeled sample. (D), Mims ENDOR spectrum of *A. aeolicus* IspH with [3-^{2}H$_1$]-**8** at the magnetic field where maximum EPR intensity was obtained, showing a ^{2}H ENDOR signal with ~ 1.5 MHz coupling. τ-averaging (200 - 448 ns at 8 ns step) was used to reduce the blind spots that arise from the τ-dependent oscillations. (E), Orientation-selective Davies ENDOR spectra of *E. coli* IspH with [U-^{13}C$_3$]-**8** across the EPR signal envelope, showing two ^{13}C signals with 3.5 MHz and 5.6 MHz hyperfine couplings, respectively. $\pi/2_{mw}$ = 48 ns for (C), 16 ns for (D), and 148 ns for (E). T = 15 K.
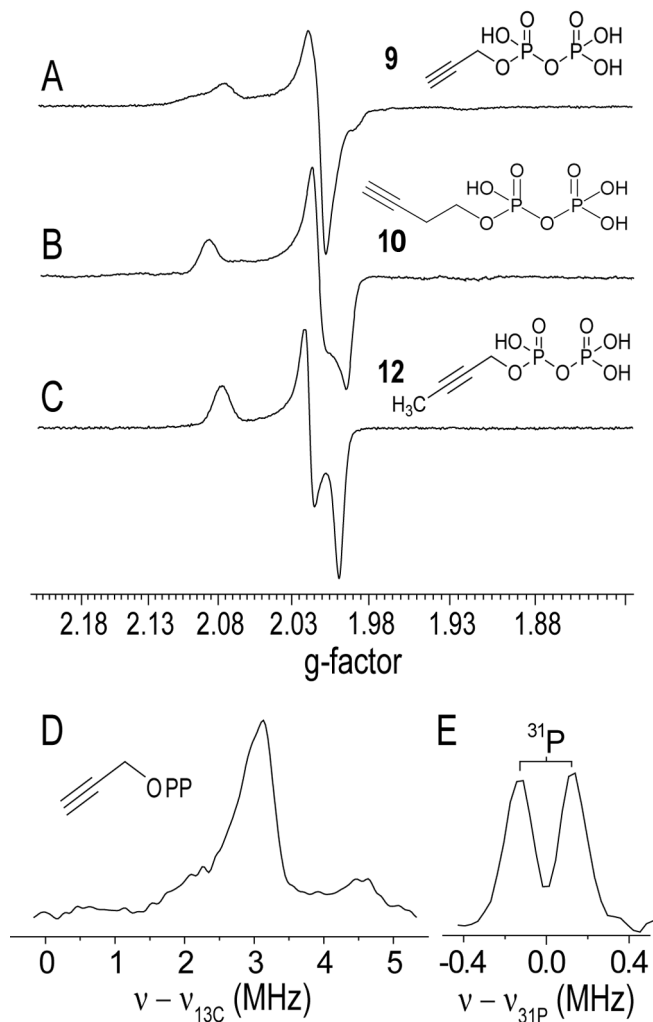
Figure 4.2. X-band EPR/ENDOR spectra of *A. aeolicus* IspH with alkyne diphosphates. (A), EPR spectrum of IspH with **9**. (B), EPR spectrum of IspH with **10**. (C), EPR spectrum of IspH with **12**. (D), ^{13}C Mims ENDOR spectrum of IspH with [U-^{13}C$_3$]-**9**. Spectrum of unlabeled **9** with IspH was subtracted. (E), ^{31}P Mims ENDOR spectrum of IspH with **9**. ENDOR spectra were collected at the magnetic field where maximum EPR intensity was obtained. $\pi/2_{mw}$ = 16 ns, T = 15 K. τ-averaging (32 spectra at 8 ns step, starting from 200 ns) was used for (D) and (E).
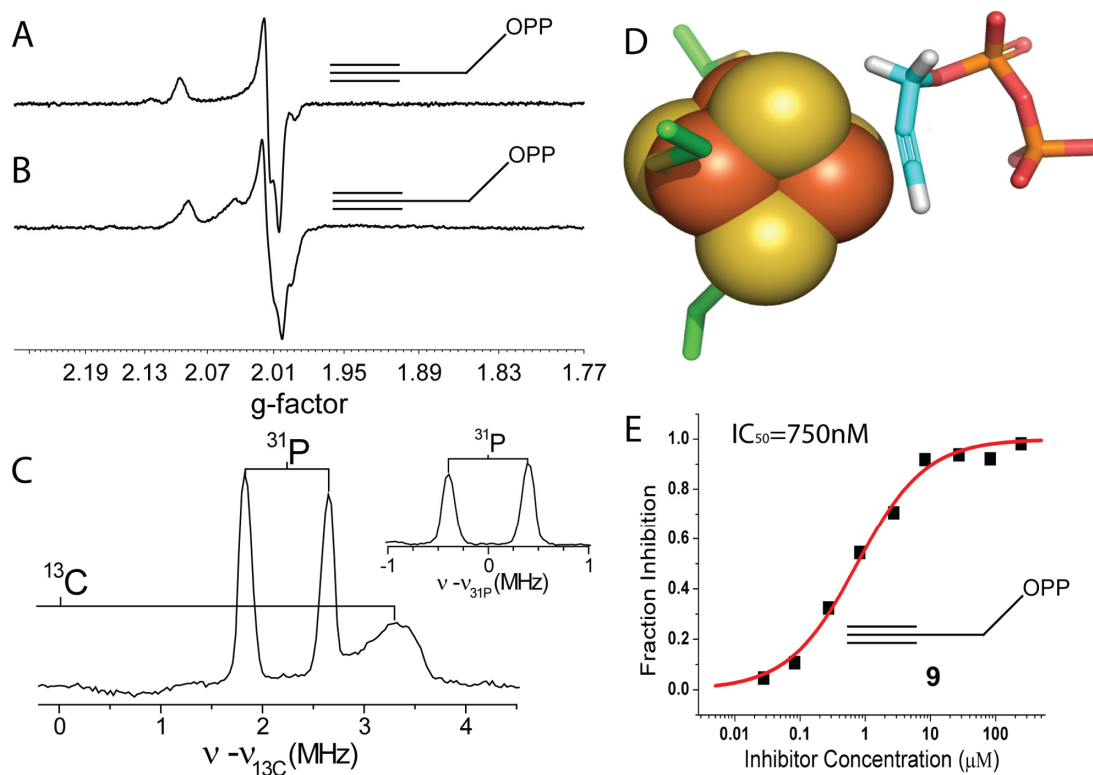
Figure 4.3. Inhibition of IspG by propargyl diphosphate **9**. (A), X-band EPR spectrum of *E. coli* IspG with **9**.

(B), X-band EPR of *T. thermophilus* IspG with **9**. (C), Mims ENDOR spectrum of *T. thermophilus* IspG with

[U-^{13}C$_3$]-**9** at the magnetic field where the maximum EPR signal intensity was obtained. The inset is the

ENDOR spectrum of IspG with unlabeled **9** showing only the ^{31}P signals. $T = 15$ K; τ-averaging (64 spectra at

8 ns steps with initial $\tau = 200$ ns) was used. (D), Schematic illustration (based on IspH + **9** docking

calculation)[9] of how **9** might bind to IspG. (E), *E. coli* IspG inhibition by **9**, with an IC$_{50}$ = 750 nM ($K_i \sim 330$

nM).

4.7 References

(1) McMillan, R. S.; Renaud, J.; Reynolds, J. G.; Holm, R. H. *J Inorg Biochem* **1979**, *11*, 213.

(2) Itoh, T.; Nagano, T.; Hirobe, M. *Tetrahedron Letters* **1980**, *21*, 1343.

(3) Tanaka, K.; Nakamoto, M.; Tsunomori, M.; Tanaka, T. *Chem Lett* **1987**, 613.

(4) Pelmenschikov, V.; Case, D. A.; Noodleman, L. *Inorg. Chem.* **2008**, *47*, 6162.

(5) Schunn, R. A.; Fritchie, C. J., Jr.; Prewitt, C. T. *Inorg Chem* **1966**, *5*, 892

(6) Crabtree, R. H. *Chapter 3 and Chapter 5, The Organometallic Chemistry of the Transition Metals (Fourth Edition)*; John Wiley & Sons, Inc.: Hoboken, New Jersey, 2005.

(7) Yu, Y.; Smith, J. M.; Flaschenriem, C. J.; Holland, P. L. *Inorg Chem* **2006**, *45*, 5742.

(8) Lee, H. I.; Igarashi, R. Y.; Laryukhin, M.; Doan, P. E.; Dos Santos, P. C.; Dean, D. R.; Seefeldt, L. C.; Hoffman, B. M. *J. Amer. Chem. Soc.* **2004**, *126*, 9563.

(9) Wang, W.; Wang, K.; Liu, Y.-L.; No, J. H.; Nilges, M. J.; Oldfield, E. *Proc Natl Acad Sci USA* **2010**, *107*, 4522.

(10) Lee, H. I.; Igarashi, R. Y.; Laryukhin, M.; Doan, P. E.; Dos Santos, P. C.; Dean, D. R.; Seefeldt, L. C.; Hoffman, B. M. *J Am Chem Soc* **2004**, *126*, 9563.

(11) Grawert, T.; Rohdich, F.; Span, I.; Bacher, A.; Eisenreich, W.; Eppinger, J.; Groll, M. *Angew Chem Int ed* **2009**, *48*, 5756.

(12) Itoh, T.; Nagano, T.; Hirobe, M. *Tetrahedron Lett* **1980**, *21*, 1343.

(13) Millen, R. P.; de Faria, D. L. A.; Temperini, M. L. A. *Vib Spectrosc* **2001**, *27*, 89.

(14) Lee, M.; Grawert, T.; Quitterer, F.; Rohdich, F.; Eppinger, J.; Eisenreich, W.; Bacher, A.;

Groll, M. *J Mol Biol* **2010**, *404*, 600.

(15) Rekittke, I.; Nonaka, T.; Wiesner, J.; Demmer, U.; Warkentin, E.; Jomaa, H.; Ermler, U. *FEBS Lett* **2010**, *585*, 447.

(16) Van Hoof, S.; Lacey, C. J.; Rohrich, R. C.; Wiesner, J.; Jomaa, H.; Van Calenbergh, S. *J Org Chem* **2008**, *73*, 1365.

(17) Wang, K.; Wang, W.; No, J. H.; Zhang, Y.; Zhang, Y.; Oldfield, E. *J Am Chem Soc* **2010**, *132*, 6719.

(18) Altincicek, B.; Duin, E. C.; Reichenberg, A.; Hedderich, R.; Kollas, A. K.; Hintz, M.; Wagner, S.; Wiesner, J.; Beck, E.; Jomaa, H. *FEBS Lett* **2002**, *532*, 437.

(19) Cheng, Y.; Prusoff, W. H. *Biochem Pharmacol* **1973**, *22*, 3099.

Chapter 5

IspH Inhibitor Discovery by Compound Library Screening:
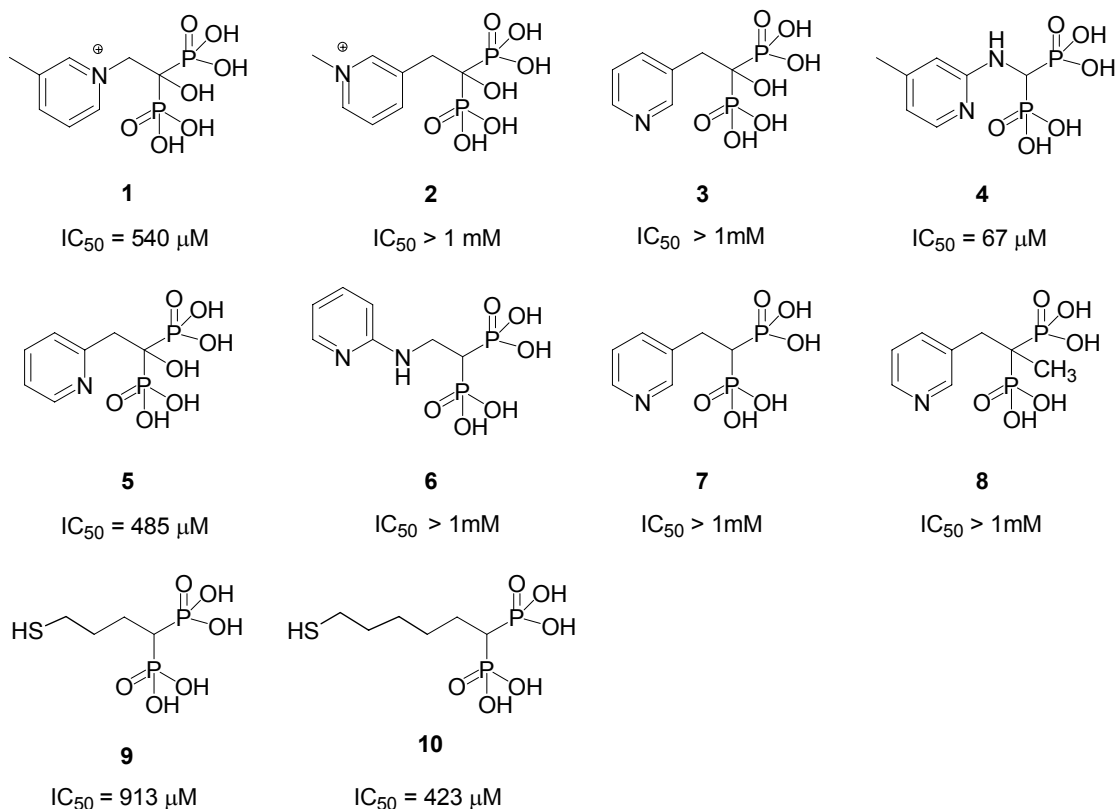
Pyridine Diphosphates

5.1 Notes and Acknowledgement

5.2 Introduction

In Chapter 3 I proposed that in IspH catalysis, the alkene substrate forms a weak π-complex with the [4Fe-4S] clusters. Inspired by this catalytic mechanism, we found that alkynes are potent inhibitors against both IspG and IspH, described in Chapter 4. Electron paramagnetic resonance (EPR) and electron-nuclear double resonance (ENDOR) study indicated that these alkynes bound at or very close to the unique 4th Fe in the reduced 4Fe-4S cluster, forming weak π-complex with the [4Fe-4S]$^{+}$ clusters. This rational-design approach was quite successful, but can I discover other types of inhibitors using an alternative strategy, through compound library screening? Our laboratory has a collection of over one thousand compounds, mostly bisphosphonates and diphosphates. Can I find any IspH/IspG inhibitors in this compound library?

5.3 Results and Discussion

5.3.1 Bisphosphonates are poor IspH inhibitors

I first investigated a series of cationic (or basic) bisphosphonates with 1-H, 1-Me or 1-OH backbone groups and pyridine, pyridinium, amino-pyridine, or thiol side-chains (Scheme 5.1). Overall, the activity of these bisphosphonates was only modest. The most active compound was **4** (IC$_{50}$ = 67 μM), an amino-pyridine, expected to contain an amidinium-like (protonated) side-chain. Based on Glide[1] docking results using the "closed" IspH structure (PDB code 3F7T) it appeared that this might be due to the "branched" nature of the bisphosphonate backbones.
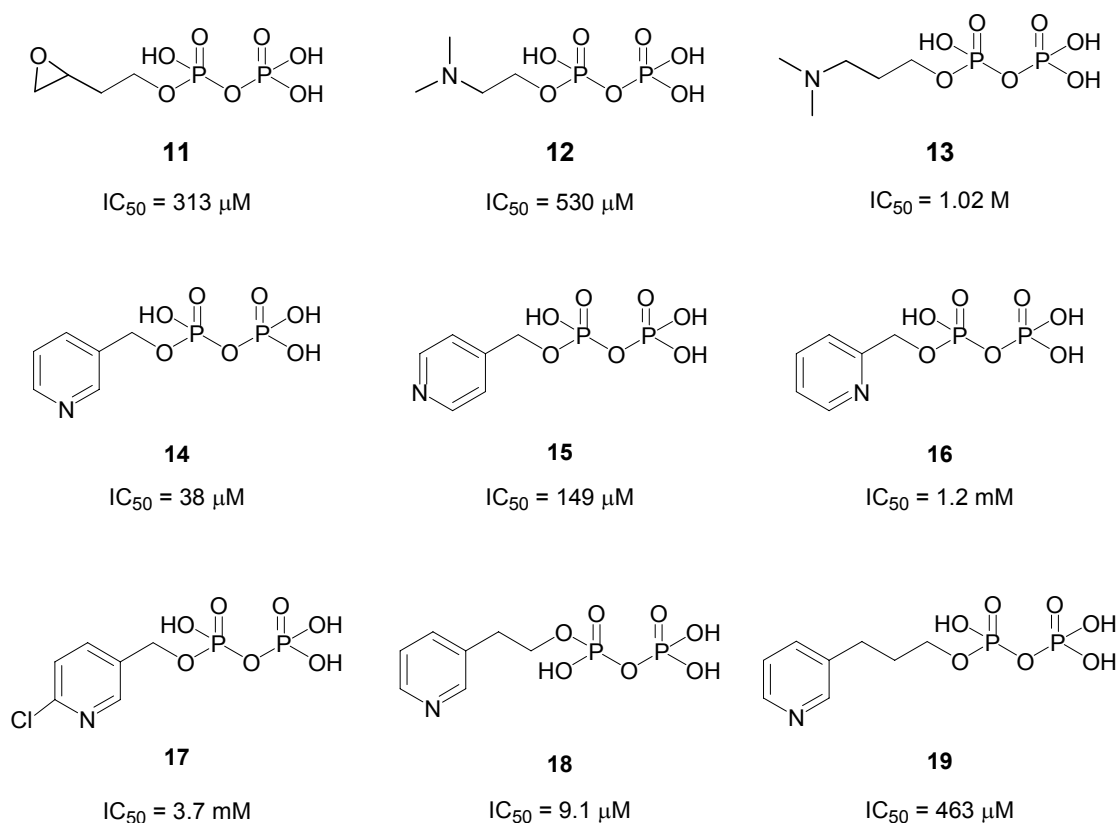
Scheme 5.1. Bisphosphonates tested against *A. aeolicus* IspH

5.3.2 Pyridine diphosphates are good *A. aeolicus* IspH inhibitors

Considering the "branched" nature of the bisphosphonate backbones which may hinder inhibitor binding, I thus next tested a series diphosphate compounds (**11-14**, Scheme 5.2). The most active compound in the series was **14**, a *meta* pyridinium diphosphate having an $IC_{50} = 38$ μM, slightly more potent than the best bisphosphonate, **4**.

We next prepared a series of analogs of **14**, and tested their inhibition effect against *A. aeolicus* IspH. The *para*-pyridinium analog (**15**) was less active ($IC_{50} = 149$ μM), and the *ortho*-pyridinium analog (**16**) was far less active ($IC_{50} = 1.2$ mM). The chloropyridine analog **17** has even weaker activity ($IC_{50} = 1.2$ mM), possibly due to the electron-withdrawing effect of the

chlorine, which results in a far less basic pyridine nitrogen than that of **14** (the computed pK_a

values of the pyridine fragments in **14** and **17** are 4.7 and 0.7, respectively). We then sought to

improve activity by varying the length of the CH_2 spacer in the side-chain: addition of 1 CH_2

group (**18**) resulted in increased inhibition activity (IC_{50} = 9.1 μM; $K_i \sim$ 1.2 μM), but addition of

2 CH_2 groups (**19**) reduced activity (IC_{50} = 463 μM).

11

IC_{50} = 313 μM

12

IC_{50} = 530 μM

13

IC_{50} = 1.02 M

14

IC_{50} = 38 μM

15

IC_{50} = 149 μM

16

IC_{50} = 1.2 mM

17

IC_{50} = 3.7 mM

18

IC_{50} = 9.1 μM

19

IC_{50} = 463 μM

Scheme 5.2. Diphosphate inhibitors tested against *A. aeolicus* IspH.

5.3.3 The binding mode of pyridine diphosphates to *A. aeolicus* IspH

How these pyridine diphosphates bind to *A. aeolicus* IspH was not clear. Considering the

pyridine nitrogen is potentially a metal ion ligand, it is possible that the pyridine nitrogen directly

binds to the unique 4th iron of the [4Fe-4S] cluster (Figure 5.1A). An alternative possibility is that this basic pyridine nitrogen interacts with the carboxyl group of E126, which is totally conserved and is at the active site. In fact, the latter binding mode is supported by a computational docking study, where we found that the diphosphate backbone binds to the diphosphate binding site of IspH seen crystallographically,[2] while the pyridinium H^N is only ~1.9 Å from the E126 O (modeled as CO_2^-), indicating the possibility of an H-bond or electrostatic interaction with this active site residue (Figures 5.1B). How do I determine which one is the real binding mode? I reasoned that these two binding mode would result in different ^{14}N hyperfine coupling constant and nuclear quadrupole coupling constant, therefore by measuring these coupling constants using pulsed EPR spectroscopy and then compare the results with well-characterized known systems, I should be able to tell what is the actual binding mode.

On addition of **14**, the EPR spectrum changed (Figure 5.2A) and new signals attributable to ^{14}N single and double quantum transitions appeared in the (+,-) quadrant of the HYSCORE spectrum (Figure 5.2B). The ^{14}N hyperfine interaction was quite large, with the hyperfine coupling constant being ~ 8 MHz. Reconstituted IspH (Figure 5.2B) and anaerobically purified IspH (Figure 5.2C) gave the same results. The *para* and *ortho*-pyridyl analogs of **14** (compounds **15** and **16**) showed no evidence of any sizeable pyridine-^{14}N hyperfine interaction in their HYSCORE spectra (Figures 5.1D, E), due presumably to their inability to bind to the 4th Fe, for "steric" reasons. Moreover, no pyridine-^{14}N HYSCORE signal was observed with the chlorine substitution of **14** (compound **17**, Figure 5.2F), consistent with it loss of inhibitory activity, due presumably to loss in donor-ability of the pyridine nitrogen. Addition of one CH_2 group to the

side-chain of **14** resulted in a better inhibitor (**18**), although there was no significant difference between the HYSCORE spectra of 14 (Figure 5.2B) and **18** (Figure 5.2G), indicating that differences in enzyme inhibition are due to differences in the alkyl diphosphate fragment binding in the active site, rather than differences in iron-pyridine interactions.

These results do not, however, prove that the ^{14}N HYSCORE signals in the (+,-) quadrant arose directly from the inhibitors **14** and **18** since, in principle, inhibitor binding might result in a protein conformational change and binding of a protein ligand to iron, e.g. the nearby histidine 42 or 124, which form part of the active site.[2] To investigate this possibility, we prepared a sample using uniformly ^{15}N-labeled IspH and inhibitor **14**. As can be seen in Figure 5.2H, the ^{14}N signals centered at ~3.6 MHz seen in Figure 5.2B were no longer present, and were replaced by a signal centered at 1.5 MHz, the ^{15}N Larmor frequency. Moreover, the ^{14}N signals in the (+,-) quadrant were essentially identical to those seen in samples prepared using unlabeled IspH (Figure 5.2B). This strongly suggests that the signals centered at ~3.6 MHz arose from protein nitrogens near the 4Fe-4S cluster, while the ^{14}N signals in the (+,-) quadrant arose from the bound inhibitor **14**, rather than from any protein residues.

To begin to better understand the interaction between the pyridine inhibitor **14** and IspH, I next simulated the HYSCORE spectra of IspH + **14** taken at three different magnetic field strengths (Figures 5.3A-C) using EasySpin[3] (Figures 5.3D-E), finding a_{iso} (^{14}N) = 7.4 MHz, *A* (^{14}N) = [6.2, 7.6, 8.4] MHz for the hyperfine interaction, and e^2qQ/h = 3.0 MHz for the nuclear quadrupole coupling constant.

This large a_{iso} (^{14}N) is similar to, or even larger than, that of a number of systems in which

nitrogens directly bind to iron centers. For example, in met-myoglobin the porphyrin nitrogens have a_{iso} = 8.11 MHz and 7.8 MHz, and the histidine N_ε has a_{iso} = 9.28 MHz.[4] In a model heme complex, FeTPP(4-MeIm)$_2$ (TPP, tetraphenylporphyrin; 4-MeIm, 4-methyl imidazole), the a_{iso} of the porphyrin nitrogens is 5.1 MHz, while that of the coordinated 4-MeIm is 5.7 MHz.[5] In Rieske-type 2Fe-2S proteins, a_{iso}(^{14}N) of the coordinated histidine nitrogens are approximately 5 MHz,[6] and in the case of the [4Fe-4S] enzyme MoaA (which also has an unique 4th iron), N1 of the substrate guanosine 5'-triphosphate binds to the 4th iron and has a_{iso} = 3.6 MHz.[7] On average, these results give an a_{iso}(^{14}N) ~ 6 MHz for systems containing Fe-N bonds, suggesting that the IspH + **14** complex also contains an Fe-N bond.
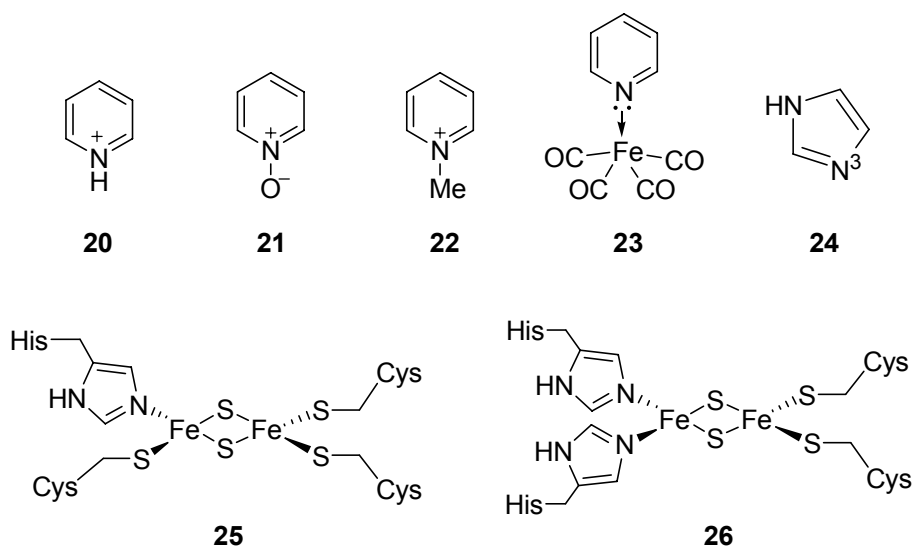
Scheme 5.3. Nitrogen-containing systems discussed in the text

The large ^{14}N hyperfine interaction seen in the IspH + **14** complex might also, at least in principle, indicate that the pyridine fragment is just close-by to the [4Fe-4S]$^+$ cluster, without

directly bonding to the 4th iron. For example, the pyridine group might be protonated and interact with e.g. the carboxyl group of glutamate 126 that is close to the cluster as suggested by computational docking; or it could be close-by, but protonated. Fortunately, determination of the ^{14}N nuclear quadrupole coupling constant (e^2qQ/h) enables an answer to this question, since protonated, neutral and metal-coordinated pyridine ligands have very different e^2qQ/h values.[8]

For pyridine itself, the e^2qQ/h is 4.6 MHz, but in species in which there is a formal +1 charge on N, such as the pyridinium ion (**20**), pyridine-N-oxide (**21**) and N-methyl pyridinium (**22**), e^2qQ/h values of approximately 1 MHz are observed experimentally.[8] In the case of pyridine bonded to Fe in Fe(CO)$_4$(pyridine), **23**, e^2qQ/h is in between these extreme values ($e^2qQ/h \sim$ 2.4 MHz), and for Mo(pyr)$_2$(CO)$_4$ as well as Cr(CO)$_4$(2,2'-bipyridyl), e^2qQ/h ~3.1 MHz. So, when pyridine nitrogen is bonded to Cr, Mo or Fe, the e^2qQ/h decreases from the 4.6 MHz seen in free pyridine to ~ 2.4 – 3.1 MHz, due to metal-ligand bonding, close to the 3.0 MHz value we find from the ^{14}N HYSCORE results.

This large decrease in e^2qQ/h, from the 4.6 MHz value found for free pyridine to the 2.4 – 3.1 MHz values observed in model systems and the IspH + **14** complex, is also seen in proteins in which imidazole (histidine) ligands bind to iron. For example, for imidazole (**24**) the N3 (deprotonated) e^2qQ/h is 4.032 MHz.[9] The e^2qQ/h values for solid imidazole and solid histidine are both smaller and essentially identical (3.27 MHz, Im; 3.36 MHz, His)[10] – due presumably to very strong hydrogen bonding in the solid state. But when bound to irons in metalloproteins, e^2qQ/h decreases considerably from the 4 MHz gas phase value (for imidazole). For example, in myoglobins, e^2qQ/h ranges from 2.2 – 2.5 MHz for the directly bonded imidazole nitrogens;[11-13]

in the $(Cys)_3$ $(His)_1$ – coordinated [2Fe-2S] cluster in the human mito-NEET protein (**25**), e^2qQ/h = (-) 2.47 MHz;[14] and in several $(Cys)_2(His)_2$-coordinated [2Fe-2S] Rieske-type protein (**26**), e^2qQ/h values have been reported to be in the range ~ 2.2-2.9 MHz.[15-17] Clearly then, the ^{14}N nuclear quadrupole coupling constant decreases from ~ 4 MHz for the free (gas phase) imidazole to ~ 2.5 MHz when bound to iron, similar to the decrease in e^2qQ/h we find with pyridine bound to iron in the 4Fe-4S cluster of IspH.

These results all support the idea that the IspH pyridine inhibitors **14** and **18** bind to IspH via a Lewis acid/base ([4Fe-4S] cluster/ligand) mechanism with direct Fe-N bonding (Figure 5.1A), rather than being due to a neutral pyridine, or protonated pyridine ligand just being close to the [4Fe-4S] cluster suggested by the computational docking result.

5.3.4 Pyridine diphosphates are weak *E. coli* IspH inhibitors

Different to results obtained with *A. aeolicus* IspH, pyridine diphosphate **14** has a much weaker inhibitory activity against *E. coli* IspH (IC_{50} = 500 μM, Scheme 5.4). In addition, on adding **14** to *E. coli* IspH in the presence of 50 equivalent sodium dithionite, *E. coli* IspH is hardly reduced based on the result of continuous-wave EPR spectroscopy; therefore HYSCORE investigation is not possible. It is possible that **14** binds to *E. coli* IspH in a different way compared with its binding mode to *A. aeolicus* IspH. We have also tested several other nitrogen-containing aromatic diphosphates (Scheme 5.4), including imidazole diphosphates (**27** and **28**) and a triazole diphosphate (**29**); however, none of them are good inhibitors.

14	**27**	**28**	**29**
$IC_{50} = 500\ \mu M$	$IC_{50} = 1.6\ mM$	$IC_{50} = 406\ \mu M$	$IC_{50} > 6\ mM$
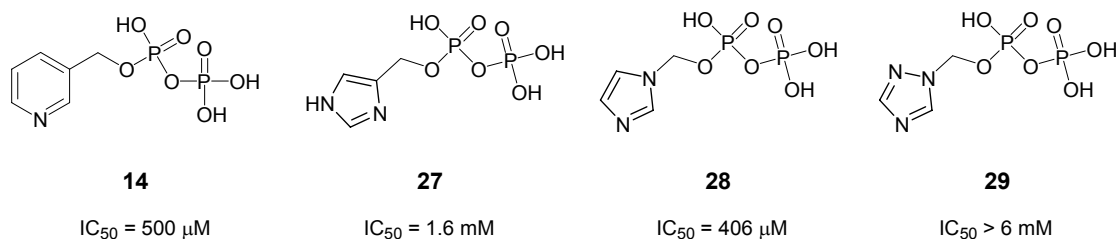
Scheme 5.4. Aromatic nitrogen-containing diphosphates tested against E. coli IspH

5.4 Conclusions

By testing a series of bisphosphonate/diphosphate compounds, I have discovered a second class of *A. aeolicus* IspH inhibitors, pyridine diphosphates. The best pyridine diphosphate, **18**, has an $IC_{50} = 9.1\ \mu M$. The binding mode of two pyridine diphosphates **14** and **18** were determined by measuring the pyridine ^{14}N hyperfine coupling constant and nuclear quadrupole coupling constant, using HSYCORE spectroscopy. By comparing these coupling constants with a series of well characterized aromatic nitrogen-containing systems, the results indicate formation of an η^1-complex between IspH and **14**, where direct Fe-N bonding is involved. *E. coli* IspH has a different inhibition profile compared with *A. aeolicus* IspH, as pyridine diphosphate **14** is a weak inhibitor against *E. coli* IspH.

5.5 Materials and Methods

A. aeolicus IspH and *E. coli* IspH production was described in Chapter 3. To prepare [u-^{15}N]-labeled *A. aeolicus* IspH, *E. coli* BL-21 (DE3) cells harboring an *A. aeolicus* IspH

plasmid were grown in M9 minimal media (12.8 g Na_2HPO_4-$7H_2O$, 3 g KH_2PO_4, and 0.5 g NaCl in 1 L distilled H_2O, supplemented with 2 mL 1M $MgSO_4$, 100 L 1M $CaCl_2$, 4 g glucose, 1 g $^{15}NH_4Cl$ and 5 mL 100X MEM vitamin solution (Sigma, St Louis, MO)). When the OD_{600} reached 0.6, 400 g/L anhydrotetracycline was added to induce the over-expression of *A. aeolicus* IspH. Cells were then allowed to grow at 28 °C for 20 hours, then harvested by centrifugation and stored in -80 °C until purification. [u-^{15}N]-labeled *A. aeolicus* IspH was then purified and reconstituted following the same procedure as unlabeled *A. aeolicus* IspH (Chapter 3). Inhibition assay was as described in Chapter 4. Electron paramagnetic resonance (EPR) and hyperfine sublevel correlation (HYSCORE) spectroscopy were as described in Chapter 2.

5.6 Figures
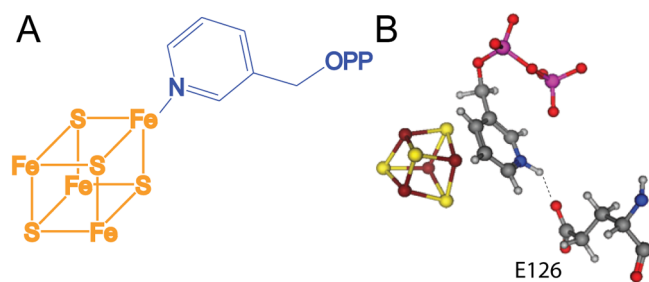
Figure 5.1. Two possible binding modes of **14** binding to *A. aeolicus* IspH. (A), η^1-complex containing a Fe-N bond. (B), pyridine nitrogen interacts with the carboxyl group of E126 residue.
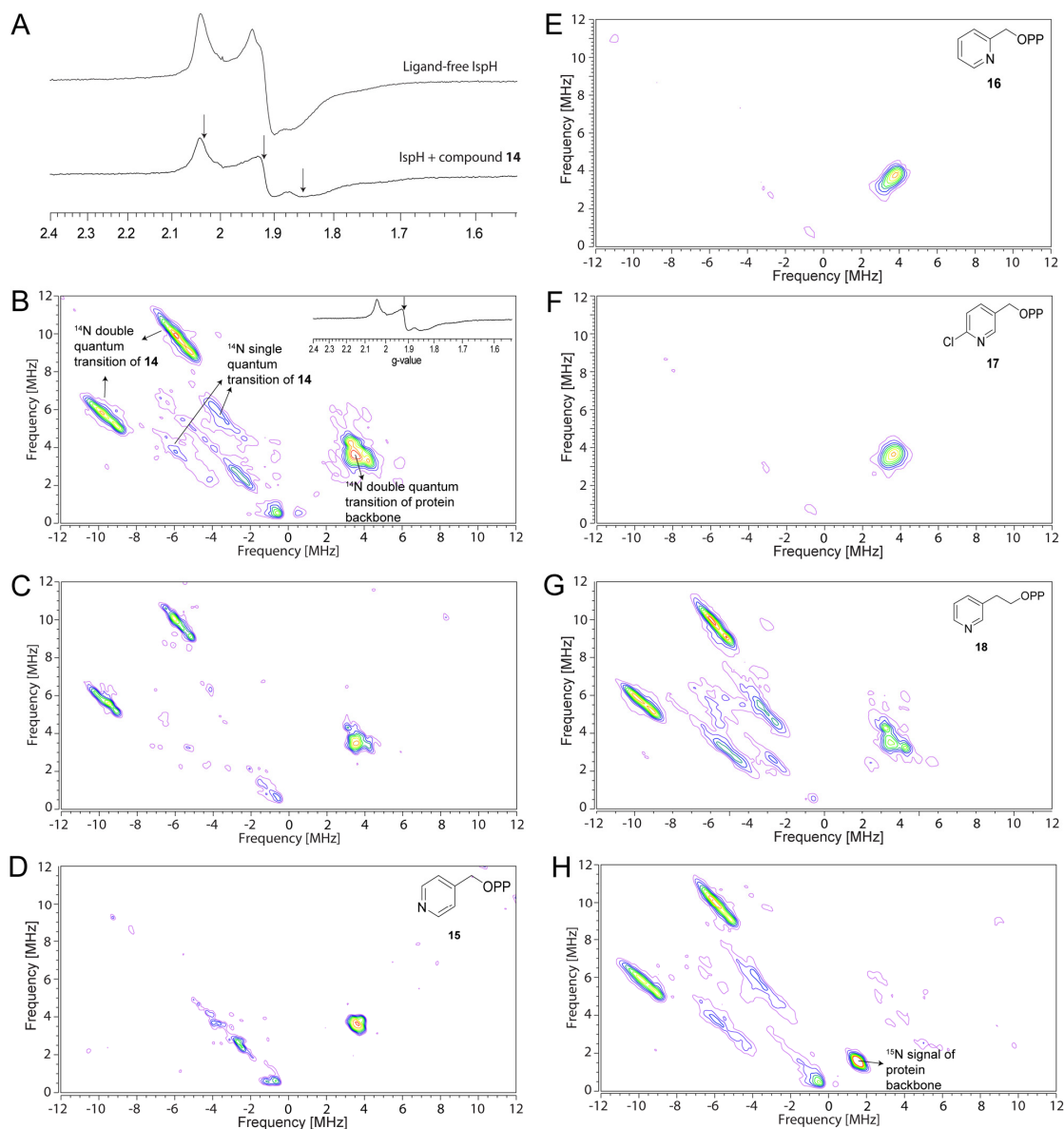
Figure 5.2. X-band EPR and HYSCORE spectra of IspH with pyridine diphosphates at g_2. (A), EPR spectra of ligand-free *A. aeolicus* IspH (top) and *A. aeolicus* IspH + **14** (bottom). (B), HYSCORE spectrum of reconstituted *A. aeolicus* IspH + **14**. The inset shows the EPR spectrum, and the arrow indicates the magnetic field position for collecting the HYSCORE data. (C), HYSCORE spectrum of anaerobically purified *A. aeolicus* IspH + **14**. (D) - (G), *A. aeolicus* IspH + **15-18**. (H), HYSCORE spectrum of ^{15}N-labeled *A. aeolicus* IspH + **14**. T = 15 K and microwave power = 1 mW for (A); T = 8 K and τ = 136 ns for (B) - (H).
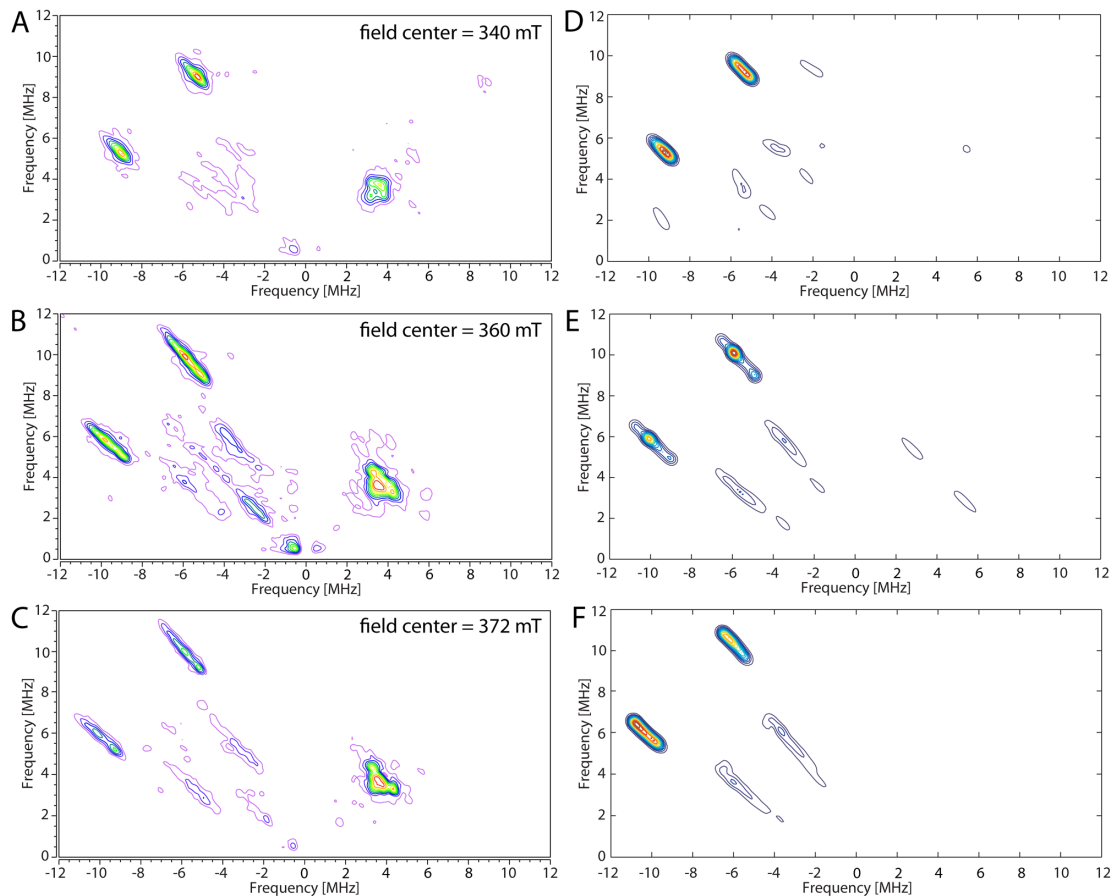
Figure 5.3. X-band HYSCORE spectra of *A. aeolicus* IspH + **14** at three different magnetic field strengths and their computer simulations. (A), 340 mT; (B), 360 mT; (C), 372 mT. (D), simulation of (A); (E), simulation of (B); (F), simulation of (C). Microwave frequency = 9.66 GHz; τ = 136ns. Simulation parameters are: *A* (^{14}N) = [6.2 7.6 8.4] MHz, α = 10˚, β = 30˚, γ = 10˚ for the hyperfine interaction and e^2qQ/h = 3.0 MHz, *η* = 0.2, α = 45˚, β = 60˚, γ = 35˚ for the quadrupole coupling interaction.

5.7 References

(1) Friesner, R. A.; Murphy, R. B.; Repasky, M. P.; Frye, L. L.; Greenwood, J. R.; Halgren, T. A.; Sanschagrin, P. C.; Mainz, D. T. *J Med Chem* **2006**, *49*, 6177.

(2) Rekittke, I.; Wiesner, J.; Rohrich, R.; Demmer, U.; Warkentin, E.; Xu, W.; Troschke, K.; Hintz, M.; No, J. H.; Duin, E. C.; Oldfield, E.; Jomaa, H.; Ermler, U. *J Am Chem Soc* **2008**, *130*, 17206.

(3) Stoll, S.; Schweiger, A. *J Magn Reson* **2006**, *178*, 42.

(4) Fittipaldi, M.; Garcia-Rubio, I.; Trandafir, F.; Gromov, I.; Schweiger, A.; Bouwen, A.; Van Doorslaer, S. *J Phys Chem B* **2008**, *112*, 3859.

(5) Vinck, E.; Van Doorslaer, S. *Phys Chem Chem Phys* **2004**, *6*, 5324.

(6) Dikanov, S. A.; Shubin, A. A.; Kounosu, A.; Iwasaki, T.; Samoilova, R. I. *J Biol Inorg Chem* **2004**, *9*, 753.

(7) Lees, N. S.; Hanzelmann, P.; Hernandez, H. L.; Subramanian, S.; Schindelin, H.; Johnson, M. K.; Hoffman, B. M. *J Am Chem Soc* **2009**, *131*, 9184.

(8) Brown, T. L. *Inorg Chem* **1980**, *19*, 392.

(9) Palmer, M. H.; Stephenson, D.; Smith, J. A. S. *Chem. Phys.* **1985**, *97*, 103.

(10) Ashby, C. I. H.; Cheng, C. P.; Brown, T. L. *J Am Chem Soc* **1978**, *100*, 6057.

(11) Scholes, C. P.; Lapidot, A.; Mascarenhas, R.; Inubushi, T.; Isaacson, R. A.; Feher, G. *J Am Chem Soc* **1982**, *104*, 2724.

(12) Magliozzo, R. S.; Peisach, J. *Biochemistry* **1992**, *31*, 189.

(13) Magliozzo, R. S.; Peisach, J. *Biochemistry* **1993**, *32*, 8446.

(14) Dicus, M. M.; Conlan, A.; Nechushtai, R.; Jennings, P. A.; Paddock, M. L.; Britt, R. D.; Stoll, S. *J Am Chem Soc* **2010**, *132*, 2037.

(15) Britt, R. D.; Sauer, K.; Klein, M. P.; Knaff, D. B.; Kriauciunas, A.; Yu, C. A.; Yu, L.; Malkin, R. *Biochemistry* **1991**, *30*, 1892.

(16) Shergill, J. K.; Joannou, C. L.; Mason, J. R.; Cammack, R. *Biochemistry* **1995**, *34*, 16533.

(17) Gurbiel, R. J.; Batie, C. J.; Sivaraja, M.; True, A. E.; Fee, J. A.; Hoffman, B. M.; Ballou, D. P. *Biochemistry* **1989**, *28*, 4861.

Chapter 6

Unexpected Hydratase Activity of the Reductase IspH

6.1 Notes and Acknowledgement

6.2 Introduction

The [4Fe-4S] enzyme IspH carries out a $2H^+/2e^-$ reduction and deoxygenation of HMBPP (**1**), to form isopentenyl diphosphate (**2**) and dimethylallyl diphosphate (**3**), shown in Scheme 6.1A.[1-3] This reaction is of interest in the context of drug discovery, since IspH is essential for cell growth in many pathogenic bacteria, as well as in malaria parasites.[4,5] In Chapter 4, I

reported the inhibition of IspH by alkyne inhibitors (**4-6**), by forming a π-complexes with the reduced iron-sulfur cluster $[4Fe-4S]^{+}$.[6] Very surprisingly, we found that some of these compounds (**5** and **6**) can react with oxidized IspH, forming the aldehyde **7** and the ketone **8**. In addition, an η^1-O-enolate reaction intermediate **9** was trapped in a crystal of oxidized IspH:**5** complex. This acetylene hydratase reaction is equivalent to that carried out by the W(IV)-containing protein acetylene hydratase,[7] where enolate formation has recently been proposed on theoretical grounds to be part of the catalytic mechanism.[8]
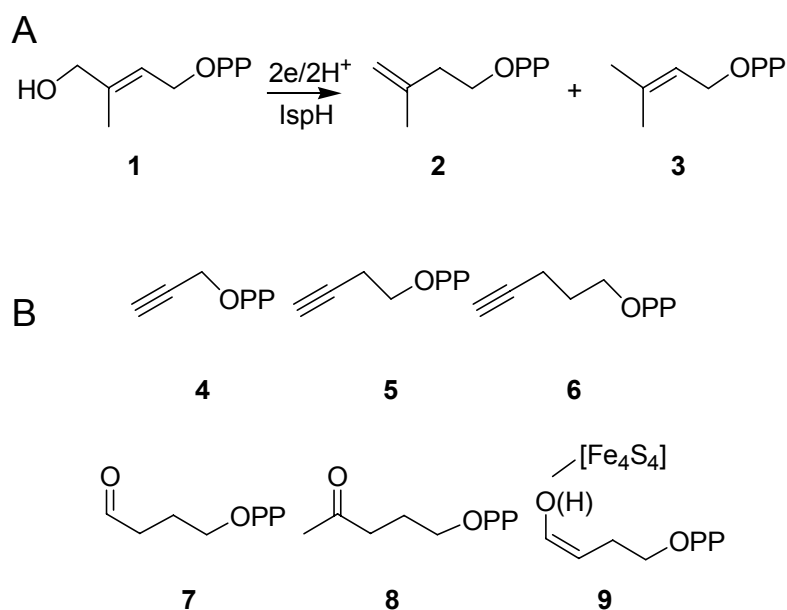
Scheme 6.1. (A), the reaction catalyzed by IspH. (B), alkyne inhibitors and the products/intermediate of their reactions with oxidized IspH

6.3 Results and Discussion

6.3.1 Mössbauer spectroscopic investigation

The oxidized IspH with an $[4Fe-4S]^{2+}$ cluster is diamagnetic, therefore it is not possible to use EPR to study inhibitors binding. I thus carried out a Mössbauer spectroscopic investigation of three IspH inhibitors[9] (**4-6**, Scheme 6.1B) bound to oxidized *E. coli* IspH. All gave similar Mössbauer spectra (Figure 6.1A-C) with quadrupole splittings (ΔE_Q) and isomer shifts (δ_{Fe}) of ~1.1 mm sec^{-1} (ΔE_Q) and ~0.45 mm sec^{-1} (δ_{Fe}). These results are different to those seen in ligand-free IspH (Figure 6.1D),[10] but are similar to those observed on addition of the HMBPP substrate (**1**) to IspH, where the quadrupole splitting of the unique 4th iron changes from 1.91 mm sec^{-1} to 1.00 mm sec^{-1}, and the isomer shift from 0.89 mm sec^{-1} to 0.53 mm sec^{-1}.[10,11] As noted by Seemann *et al.*[10] based on previous work with aconitase and model systems,[12] this indicates conversion from a 3S,3N/O (octahedral) coordination to 3S,1O (tetrahedral) coordination. The Mössbauer results of IspH with **4-6** might also suggest a 3S,1O coordination on inhibitors binding, as reported for **1**. To better understand how do these inhibitors bind to oxidized IspH enzyme, our collaborators in Michael Groll's laboratory performed co-crystallization of compounds **4-6** bound to oxidized IspH and analyzed the obtained X-ray crystal structures.

6.3.2 Propargyl diphosphate binding to the oxidized IspH

The crystal structure of propargyl diphosphate (**4**) binding to oxidized IspH revealed a different binding mode compared with that when IspH is in its reduced state. As can be seen in Figure 6.2A, the acetylene group of **4** is not bonded to the unique 4th iron (Fe-C distances of

3.4-3.5Å). Rather, there is a water molecule (or, in principle, a hydroxide ion) bound to the [Fe$_4$S$_4$] cluster with a Fe-O bond length of 2.1 Å, essentially the same as is found when **1** is bound to oxidized IspH.[13,14] The crystal structure of IspH in complex with **4** then gives a ready explanation of the ^{57}Fe Mössbauer results: the $_{Fe}$ and ΔE_Q values for **1** as well as **4** bound to IspH are essentially the same because both species contain a [4Fe-4S] cluster with 3S,1O coordination to the apical iron.

6.3.3 But-3-ynyl diphosphate is converted to an aldehyde by the oxidized IspH

The X-ray structure of IspH in complex with but-3-ynyl diphosphate (**5**) is, however, totally different (Figure 6.2B), even though the Mössbauer spectroscopic results (Figures. 6.1A, B) are similar. Whereas the diphosphate backbone of this longer-chain species binds to the same Ser-X-Asn motif as found with **1** and **4**, the ligand has undergone a chemical reaction, hydration. The crystal structure clearly indicates formation of an η^1-enolate (**9**) complex, having an Fe-O bond length of 2.0 Å. As with the substrate **1**,[14] binding of ligand **5** protects the [4Fe-4S] cluster from O$_2$, with the bound enolate **9** being remarkably stable in air.

Also of interest is the observation that this complex actually turns over, forming the aldehyde **7**, as evidenced by the appearance of a ^{1}H NMR peak at 9.72 ppm (Figure 6.3A). In aqueous solution, such aldehydes exist in part as hydrates (*gem*-diols), and the J-couplings seen in Figure 6.3A are consistent with the presence of both the free aldehyde as well as the 4,4-diol - just as reported previously with 3-formyl-1-butyl diphosphate.[15] When **5** is added to IspH in D$_2$O, the ^{1}H NMR resonances from C3 at 2.63 ppm (the aldehyde, **7**) and 1.65 ppm (the hydrate) are missing (Figure 6.3B), because the proton that attaches to C3 in initial enolate formation is now

117

actually a deuterium, plus, the enolate H is replaced by a deuterium as well. These observations are confirmed by electrospray ionization mass spectroscopy (ESI-MS, Figure 6.3C), indicating formation of an m/e=246.9 amu parent ion, due to water addition to **5**. These X-ray crystal structures give a good explanation of the Mössbauer observation, that the isomer shift and quadrupole splitting of the fourth iron both decrease on ligand binding and are comparable to the IspH:**4** and IspH:**5** complexes, since the enolate provides a 3S,1O coordination sphere.

6.3.4 Pent-4-ynyl diphosphate is converted to a ketone by the oxidized IspH

In the case of the pent-4-ynyl diphosphate **6**, the Mössbauer results (Figure 6.1C) are consistent with 3S,1O coordination but, once again, the data reveal that a chemical reaction of the acetylene group has occurred. However, rather than forming an aldehyde (via anti-Markovnikov addition), the ^{1}H-NMR results (Figures 6.3D) indicate primarily Markovnikov addition and formation of the ketone, **8**, confirming the results of mass spectrometry (Figure 6.3E). The Mössbauer spectra suggest initial enolate formation as observed with **5**, but the X-ray complex structure (Figure 6.2C) reveals a [Fe$_3$S$_4$] cluster, so evidently the fourth iron is lost during crystallization.

6.4 Conclusions

The results presented above all indicate that the 2H$^+$/2e$^-$ reductase IspH, which normally catalyzes the reductive dehydroxylation of HMBPP to form dimethylallyl diphosphate and isopentenyl diphosphate, is promiscuous. The root cause of this promiscuity involves the

addition or removal of OH groups at C4 in bound ligands (Scheme 6.2), with or without cluster

reduction. The substrate HMBPP (**1**) binds to the fourth Fe via O4 and reductive dehydroxylation

ensues (Scheme 6.2B). With **4**, the C_3 side-chain is too short to interact directly with the oxidized

cluster (Scheme 6.2A), but with the C_4 species **5**, OH (presumably from a cluster-bound water)

adds to C4 via anti-Markovnikov addition to form the η^1-enolate **9,** which is then released as the

aldehyde **7** (Scheme 6.2C). With a C_5 side chain, OH once again adds at C4, but now,

protonation must be at C5 - Markovnikov addition - resulting in ketone **8** formation (Scheme

6.2D). Neither reaction is catalyzed with reduced IspH. These results all reveal a wholly

unexpected side to IspH reactivity of importance in inhibitor design, and support the idea that

metal enolates may be involved in acetylene hydratase activity in other systems, as proposed on

theoretical grounds.[8]
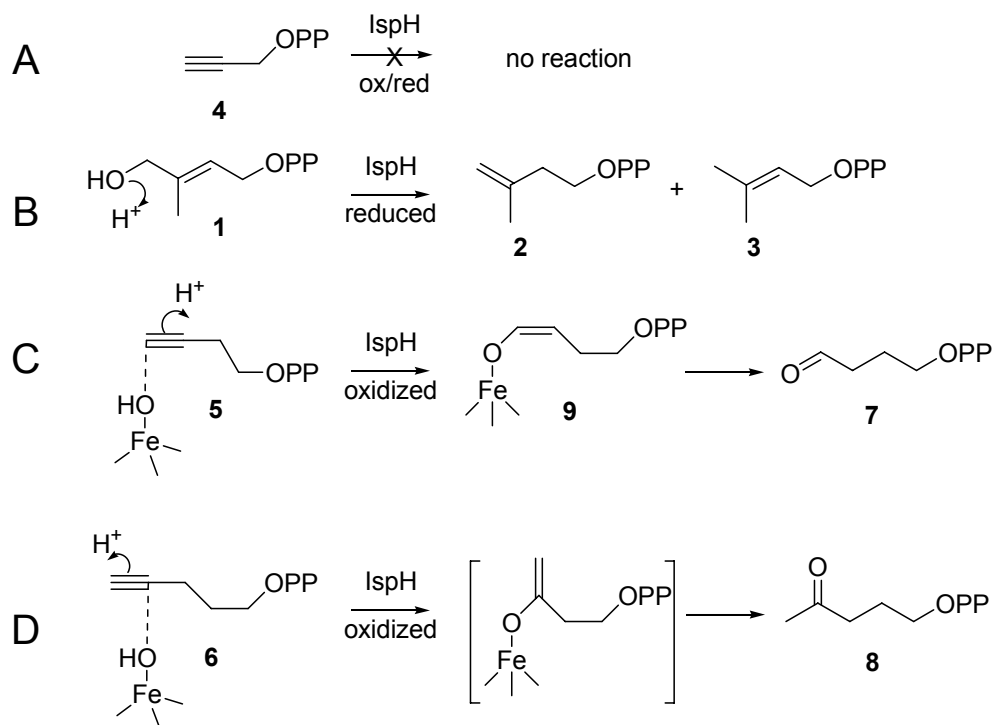
**Scheme 6.2.** Summary of IspH reactions

119

6.5 Materials and Methods

6.5.1 General aspects

Syntheses of **4-6** have been reported previously.[6,9] *E. coli* IspH protein production and purification was described in Chapter 3. For ^{57}Fe labeled *E. coli* IspH, ^{57}Fe metal was dissolved by HCl and H_2O_2, and was added to the growth media to 80 μM/L when arabinose was added to induce the expression of *isc* proteins.
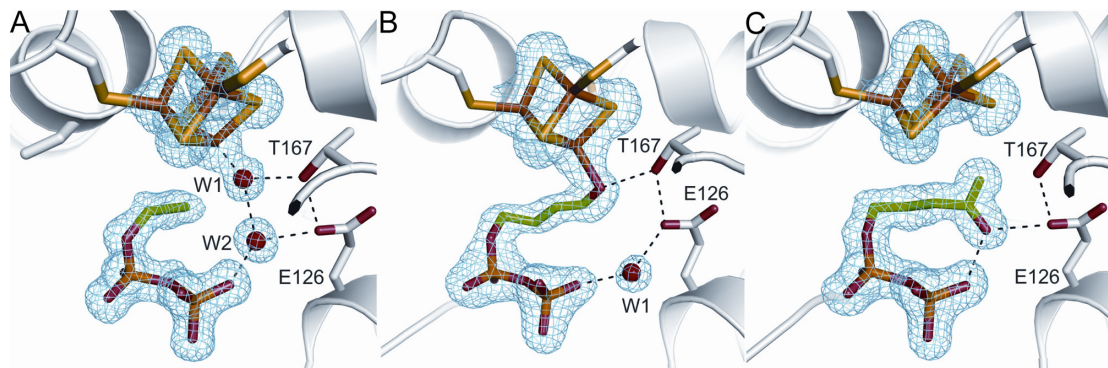
6.5.2 Spectroscopy

Mössbauer spectra were collected on a constant acceleration spectrometer (Knox College) at 77 K with a 500 G magnetic field perpendicular to the γ-ray. ^{1}H-NMR spectra were collected on a 500 MHz Varian Unity spectrometer. ESI-MS spectra were collected on a Waters Quattro II mass spectrometer in negative mode.

6.6 Figures
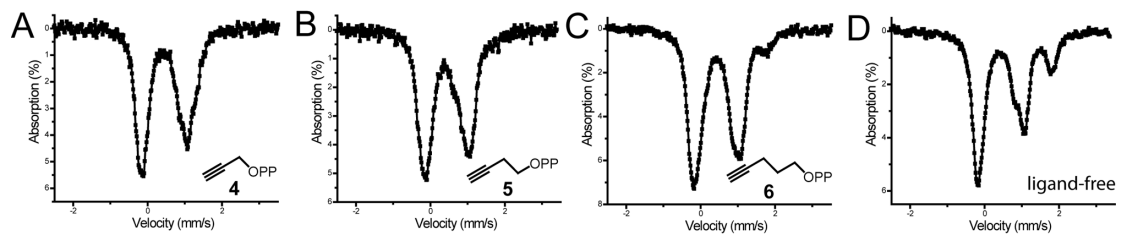
Figure 6.1. Mössbauer spectra of *E. coli* IspH with alkyne diphosphates or ligand-free. (A), propargyl

diphosphate, **4**. (B), but-3-ynyl diphosphate, **5**. (C), pent-4-ynyl diphosphate, **6**. (D), ligand-free IspH.

Figure 6.2. X-ray crystal structures of diphosphate ligands bind to *E. coli* IspH. (A), **4** binds to *E. coli* IspH.

(B), **5** is converted to the enolate **9** with *E. coli* IspH. (C), **6** is converted to the ketone **8** with *E. coli* IspH.
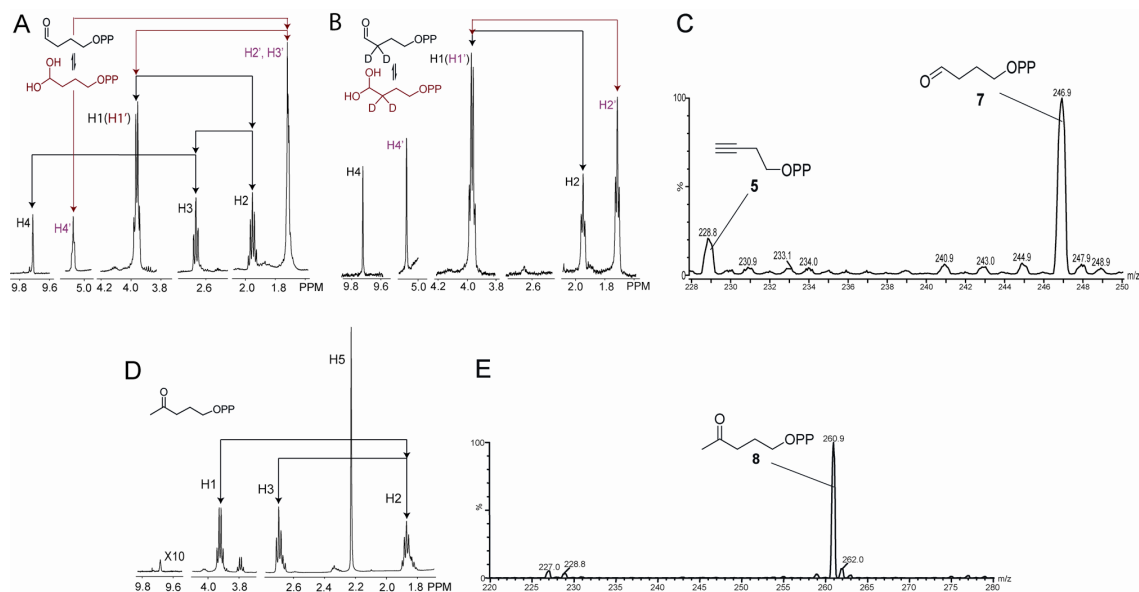
Figure 6.3. Spectroscopic evidence of hydration reactions of **5** and **6**. (A), ^{1}H NMR spectrum (500 MHz) of aldehyde **7** (black) and *gem*-diol (red) formed on hydration of **5** by IspH in natural abundance water. (B), ^{1}H NMR spectrum (500 MHz) of aldehyde **7** (black) and *gem*-diol (red) formed on hydration of **5** by IspH in D_2O. (C), ESI-MS spectrum of the aldehyde **7** due to hydration of **5** by oxidized IspH. (D), ^{1}H NMR spectrum (500 MHz) of the Markovnikov-product, **8**. (E), ESI-MS spectrum of IspH with inhibitor **6** also reveals a hydration of the ligand at its C4 position, forming the ketone **8**.

6.7 References

(1) Wolff, M.; Seemann, M.; Tse Sum Bui, B.; Frapart, Y.; Tritsch, D.; Garcia Estrabot, A.; Rodriguez-Concepcion, M.; Boronat, A.; Marquet, A.; Rohmer, M. *FEBS Lett* 2003, *541*, 115.

(2) Altincicek, B.; Duin, E. C.; Reichenberg, A.; Hedderich, R.; Kollas, A. K.; Hintz, M.; Wagner, S.; Wiesner, J.; Beck, E.; Jomaa, H. *FEBS Lett* 2002, *532*, 437.

(3) Rohdich, F.; Zepeck, F.; Adam, P.; Hecht, S.; Kaiser, J.; Laupitz, R.; Grawert, T.; Amslinger, S.; Eisenreich, W.; Bacher, A.; Arigoni, D. *Proc Natl Acad Sci U S A* 2003, *100*, 1586.

(4) Rohmer, M.; Grosdemange-Billiard, C.; Seemann, M.; Tritsch, D. *Curr Opin Investig Drugs* 2004, *5*, 154.

(5) Hunter, W. N. *Curr Top Med Chem* 2011, *11*, 2048.

(6) Wang, W.; Wang, K.; Liu, Y.-L.; No, J. H.; Nilges, M. J.; Oldfield, E. *Proc Natl Acad Sci USA* 2010, *107*, 4522.

(7) Seiffert, G. B.; Ullmann, G. M.; Messerschmidt, A.; Schink, B.; Kroneck, P. M.; Einsle, O. *Proc Natl Acad Sci USA* 2007, *104*, 3073.

(8) Liao, R. Z.; Yu, J. G.; Himo, F. *Proc Natl Acad Sci U S A* 2010, *107*, 22523.

(9) Wang, K.; Wang, W.; No, J. H.; Zhang, Y.; Zhang, Y.; Oldfield, E. *J Am Chem Soc* 2010, *132*, 6719.

(10) Seemann, M.; Janthawornpong, K.; Schweizer, J.; Bottger, L. H.; Janoschka, A.; Ahrens-Botzong, A.; Tambou, E. N.; Rotthaus, O.; Trautwein, A. X.; Rohmer, M.;

Schunemann, V. *J Am Chem Soc* 2009, *131*, 13184.

(11) Ahrens-Botzong, A.; Janthawornpong, K.; Wolny, J. A.; Tambou, E. N.; Rohmer, M.; Krasutsky, S.; Poulter, C. D.; Schunemann, V.; Seemann, M. *Angew Chem Int ed* 2011, *50*, 11976.

(12) Ciurli, S.; Carrie, M.; Weigel, J. A.; Carney, M. J.; Stack, T. D. P.; Papaefthymiou, G. C.; Holm, R. H. *J Am Chem Soc* 1990, *112*, 2654.

(13) Rekittke, I.; Wiesner, J.; Rohrich, R.; Demmer, U.; Warkentin, E.; Xu, W.; Troschke, K.; Hintz, M.; No, J. H.; Duin, E. C.; Oldfield, E.; Jomaa, H.; Ermler, U. *J Am Chem Soc* 2008, *130*, 17206.

(14) Grawert, T.; Span, I.; Eisenreich, W.; Rohdich, F.; Eppinger, J.; Bacher, A.; Groll, M. *Proc Natl Acad Sci USA* 2010, *107*, 1077.

(15) Zhang, Y.; Song, Y.; Yin, F.; Broderick, E.; Siegel, K.; Goddard, A.; Nieves, E.; Pasa-Tolic, L.; Tanaka, Y.; Wang, H.; Morita, C. T.; Oldfield, E. *Chem Biol* 2006, *13*, 985.